COMPUTATIONAL FLUID DYNAMIC MODELING OF CHEMICALLY REACTING GAS-PARTICLE FLOWS

by

Miguel Olivas-Martinez

A dissertation submitted to the faculty of
The University of Utah
in partial fulfillment of the requirements for the degree of

Doctor of Philosophy

Department of Metallurgical Engineering

The University of Utah

December 2013

The University of Utah Graduate School

STATEMENT OF DISSERTATION APPROVAL

The dissertation of **Miguel Olivas-Martinez**

has been approved by the following supervisory committee members:

Hong Yong Sohn	, Chair	**July 31 2013** Date Approved
Raj K. Rajamani	, Member	**July 31 2013** Date Approved
Michael S. Moats	, Member	**July 31 2013** Date Approved
Moo Eob Choi	, Member	**July 31 2013** Date Approved
Terry A. Ring	, Member	**July 31 2013** Date Approved

and by **Manoranjan Misra**, Chair of the Department of **Metallurgical Engineering**

and by David B. Kieda, Dean of The Graduate School.

ABSTRACT

Computational fluid dynamic modeling was performed to describe and analyze the various processes occurring in three chemically reacting gas-particle flows: chemical vapor synthesis of tungsten carbide and aluminum nanopowders, flame synthesis of silica nanopowder, and a novel flash ironmaking process based on the direct gaseous reduction of iron oxide concentrate particles.

The model solves the three-dimensional turbulent governing equations of overall continuity, momentum, energy, and species transport including gas-phase chemical kinetics. For modeling nanopowder synthesis, the particle size distribution is obtained by solving the population balance model. The particle nucleation rate is calculated based on chemical kinetics or homogeneous nucleation theory. The particle growth rate is calculated by vapor condensation, Brownian coagulation or a combination of both, depending on the type of material. The quadrature method of moments is used to numerically solve the population balance. For modeling the flash ironmaking reactor, a simplified chemical reaction mechanism for hydrogen-oxygen combustion is used to calculate realistic flame temperatures. The iron oxide concentrate particles are treated from a Lagrangian viewpoint.

First, the chemical vapor synthesis of tungsten carbide nanopowder was simulated. Using available experimental data, a parametric study was conducted to

determine the nucleation and growth rate constants. Second, the flame synthesis of silica nanopowder was simulated. A single value of the collision efficiency factor was sufficient to reproduce the magnitude as well as the variations of the average particle diameter with different experimental conditions. Third, the chemical vapor synthesis of aluminum nanopowder was simulated. Comparison of model predictions with the available experimental data showed good agreement under different operating conditions without the need of adjustable parameters.

For modeling the flash ironmaking reactor, experiments reported in the literature for a nonpremixed hydrogen jet flame were simulated for validation. Model predictions showed good agreement with gas temperature and species concentrations measurements. The model was used to design a nonpremixed hydrogen-oxygen burner. The distributions of velocity, temperature, and species concentrations, and the trajectories of iron oxide concentrate particles in a lab flash reactor were computed and analyzed.

To Silvia and Victoria

TABLE OF CONTENTS

LIST OF TABLES

LIST OF FIGURES

NOMENCLATURE

Symbol	Units	Definition
A_d	m^2	Spray droplet surface area
A_f	m^2	Furnace cross-sectional area
A_p	m^2	Particle surface area
B_{coag}	# m^{-3} m^{-1} s^{-1}	Birth rate term due to coagulation in population balance equation
$\bar{c}_i$	m s^{-1}	Mean molecular velocity of the *i*th species, defined by Equation (2-39)
$\bar{c}_j$	m s^{-1}	Mean thermal velocity of the *j*th particle, defined by Equation (2-45)
c_p	J kg^{-1} K^{-1}	Particle heat capacity at constant pressure in Equation (2-10)
$c_{p,g}$	J kg^{-1} K^{-1}	Gas heat capacity at constant pressure
C_c	1	Slip correction factor defined by Equation (2-44)
C_D	1	Drag coefficient
C_i	mol m^{-3}	Molar concentration of the *i*th species
C_μ	1	Turbulent parameter used in Equation (2-23)
d_j	m	Diameter of particles in the *j*th trajectory
d_p	m	Particle diameter
d_p^*	m	Critical particle diameter
d_{pg}	m	Geometric mean diameter

D_{coag}	# m^{-3} m^{-1} s^{-1}	Death rate term due to coagulation in population balance equation
D_{k-mix}	m^2 s^{-1}	Diffusion coefficient of the *k*th species in the vapor mixture
D_j	m^2 s^{-1}	Diffusion coefficient of the *j*th particle, defined by Equation (2-43)
e_g	W m^{-3} sr^{-1}	Volumetric emission term from gas phase
e_p	W m^{-3} sr^{-1}	Volumetric emission term from particle phase
E	1	Empirical constant used in Equation (2-24); $E = 9.793$
$E_{a,j}$	cal mol^{-1}	Activation energy of the *j*th reaction
$\vec{g}$	m^2 s^{-1}	Gravity vector
g_i	m^2 s^{-1}	*i*th component of the gravity vector
g_j	m	Transition parameter of the *j*th particle, defined by Equation (2-46)
G	W m^{-2}	Total incident flux or irradiance
G	m s^{-1}	Linear particle growth rate by vapor condensation (gas-to-particle conversion), defined by Equation (2-37)
G_m	m s^{-1}	Linear particle growth rate under the control of mass transfer
$G_{overall}$	m s^{-1}	Overall linear particle growth rate under the combined control of surface chemical reaction and mass transfer
G_{rxn}	m s^{-1}	Linear particle growth rate under the control of chemical reaction kinetics
h_g	J kg^{-1}	Gas specific enthalpy
h_{eff}	W m^{-2} K^{-1}	Effective heat convection coefficient at inner wall surface
h_f	W m^{-2} K^{-1}	Convective heat transfer coefficient at outer wall surface
h_p	J kg^{-1}	Particle specific enthalpy
h_s	W m^{-2} K^{-1}	Convective heat transfer coefficient of the particle
H_r	W	Net rate of heat production of the particle by chemical reaction
I	W m^{-2} sr^{-1}	Radiation intensity per steradian

$I_{\Omega,w}$	W m^{-2} sr^{-1}	Radiation intensity per steradian leaving the wall surface in the direction Ω
J	# m^{-3} s^{-1}	Particle nucleation rate
J	1	Number of particle trajectories
k	m^2 s^{-2}	Turbulent kinetic energy
k	W m^{-1} K^{-1}	Thermal conductivity
$k_{a,g}$	m^{-1}	Absorption coefficient of gas
$k_{a,p}$	m^{-1}	Absorption coefficient of particles
k_B	J K^{-1}	Boltzmann constant; $k_B = 1.38 \times 10^{23}$ J K^{-1}
$k_{c,i}$	m s^{-1}	Convective mass transfer coefficient of species *i*
k_d	s^{-1}	Decomposition rate constant
$k_{f,j}$	Various	Rate coefficient of the *j*th forward reaction
k_g	W m^{-1} K^{-1}	Gas thermal conductivity
k_g	m^7 kmol^{-2} s^{-1}	Growth rate constant; used in Equation (3-3)
k_m	m s^{-1}	Convective mass transfer coefficient; used in Equation (3-4)
k_n	# m^{-3} s^{-1}	Nucleation rate constant; used in Equation (3-2)
k_P	m^2 s^{-2}	Turbulent kinetic energy at point *P* adjacent to the wall, used in Equation (2-23)
$k_{r,j}$	Various	Rate coefficient of the *j*th backward reaction
k_s	s^{-1}	Scattering coefficient for radiation
$K_{c,J}$	Various	Concentration equilibrium constant
Kn	1	Knudsen number defined by Equation (2-38)
l_j	m	Mean free path of the *j*th particle, defined by Equation (2-47)
L_e	m	Mean beam length; $L_e = 3.6\frac{V_f}{A_f}$

m	kg	Mass
m_i	kg	Molecular mass of the *i*th species, used in Equation (2-39)
m_j	kg	Mass of the *j*th particle
m_k	$m^k\ m^{-3}$	*k*th moment of the particle size distribution
m_p	kg	Particle mass
M_i	$g\ mol^{-1}$	Molecular weight of the *i*th species
$\boldsymbol{n}$	1	Normal vector used in radiation computations; used in Equation (2-17)
n	$\#\ m^{-3}\ s^{-1}$	Particle number density function
n_j	$\#\ m^{-3}$	Number density of particles of the *j*th trajectory
n_p	$\#\ m^{-3}$	Particle number density
$\dot{n}_p$	$\#\ s^{-1}$	Particle number flow rate of the *j*th trajectory
n_w	m	Local coordinate normal to the wall; used in Equation (2-21) and (2-22)
N	mol^{-1}	Avogadro's number
N_i	$\#\ m^{-3}$	Number concentration of the *i*th species in the vapor phase
p	Pa	Pressure
p_i	Pa	Partial pressure of the *i*th species
p_i°	Pa	Vapor pressure of the *i*th species at the particle surface
P	1	Parameter used in Equation (2-24); defined by $P = 9.24\left[\left(\frac{\mathrm{Pr}}{\mathrm{Pr}_t}\right)^{3/4} - 1\right]\left[1 + 0.28e^{-0.007\mathrm{Pr}/\mathrm{Pr}_t}\right]$
Pr	1	Laminar Prandtl number
Pr_t	1	Turbulent Prandtl number; $\mathrm{Pr}_t = 0.85$ at the wall
q	$W\ m^{-2}$	Wall heat flux

q_w	W m^{-2}	Incident radiation heat flux at the wall surface
Q_{rg}^h	W m^{-3}	Net radiative heat-transfer rate to the gas phase
Q_{rp}	W	Net radiative heat-transfer rate to the particle
Q_{rp}^h	W m^{-3}	Net radiative heat-transfer rate to the particle phase
r	m	Radial coordinate direction
R	J mol^{-1} K^{-1}	Gas constant
R_j	mol m^{-3} s^{-1}	Net rate of the *j*th reaction
S	m	Radiation path length; used in Equation (2-15)
S	1	Supersaturation ratio; defined by Equation (2-35)
S_i	kg m^{-3} s^{-1}	Net mass generation of the *i*th species by gas-phase reactions
S_g^h	W m^{-3}	Source term due to gas-phase chemical reactions
S_p	kg m^{-3} s^{-1}	Mass generation or addition in the particulate phase from the interaction with the gas phase; used in Equation (2-51)
S_p^h	W m^{-3}	Source term due to the net heat transfer by convection from the particles to the gas phase
S_p^m	kg m^{-3} s^{-1}	Total mass source term in the gas-phase continuity equation [Equation (2-3)] due to the presence of particles
S^ϕ	Various	Net source term of dependent variable ϕ
t	s	Time
t_0	s	Long enough time to obtain a smooth-averaged value
T	K	Temperature
T_b	K	Bulk temperature
T_g	K	Gas temperature
T^*	1	Dimensionless temperature defined by Equation (2-24)
T_p	K	Particle temperature

T_P	K	Temperature at the cell P adjacent to the wall; used in Equation (2-24)
T_w	K	Wall temperature
T_∞	K	Surroundings temperature
$\vec{u}$	m s^{-1}	Gas velocity vector
u_i	m s^{-1}	Gas velocity component in the ith direction
u_i'	m s^{-1}	Instantaneous gas velocity component in the ith direction
$\vec{v}$	m s^{-1}	Particle velocity vector
v_i	m s^{-1}	Particle velocity component in the ith direction
v_i	m^3	Molecular volume of the ith species; used in Equation (2-36)
$\vec{v}_m$	m s^{-1}	Mixture velocity vector
v_{WC}	m^3 $kmol^{-1}$	WC molar volume; $v_{WC} = 0.0125$ m^3 $kmol^{-1}$
V_{cell}	m^3	Volume of a computational cell
V_f	m^3	Furnace volume
V_i	m^3 mol^{-1}	Molar volume of condensable the ith species
x	m	x-coordinate length
x_i	m	Coordinate length in the ith direction
y	m	y-coordinate length
Y_i	1	Favre-averaged mass fraction of the ith species
y_P	m	Distance from point P to the wall
y^*	m	Dimensionless distance from point P to the wall; $y^* = \frac{\rho_g C_\mu^{1/4} k_p^{1/2} y_P}{\mu}$
y_T^*	1	Thermal sublayer thickness calculated by the procedure described in conjunction with Equation (2-24)

z	m	z-coordinate length

Greek Symbols

α_k	1	Volume fraction of the kth phase
α_v	1	Vapor-phase collision efficiency factor
α_p	1	Particle collision efficiency factor
β	1	Collision frequency function defined by Equation (2-42)
Γ_ϕ	Various	Effective transport coefficient
δ_i	1	Unit vector in the ith direction
δ_{ij}	1	Kronecker delta function
ε	$m^2\ s^{-3}$	Turbulent dissipation rate
ε_g	1	Gas emissivity
ε_p	1	Particle emissivity
ε_w	1	Wall emissivity
κ	1	Von Kármán constant; $\kappa = 0.4187$
λ	m	Mean free path of vapor molecules
μ	Pa s	Viscosity
μ_g	Pa s	Gas viscosity
μ_t	Pa s	Turbulent viscosity
ρ	$kg\ m^{-3}$	Density
ρ_g	$kg\ m^{-3}$	Gas density
ρ_k	$kg\ m^{-3}$	Density of the kth phase

ρ_m	kg m^{-3}	Mixture density defined by Equation (2-49)
ρ_M	mol m^{-3}	Molar density; used in Equation (2-34)
ρ_p	kg m^{-3}	Particle density
σ	N m^{-1}	Surface tension
σ	W m^{-2} K^{-4}	Stefan-Boltzmann constant; $\sigma = 5.67\times10^{-8}$ Wm^{-2}K^{-4}
σ_{gs}	m	Geometric standard deviation
ϕ	1	Generic dependent variable
Φ	1	Phase function; used in Equation (2-15)
ω	sr	Solid angle
Ω, Ω''	1	Outward and inward direction vectors of radiation intensity

Subscripts

b	Bulk
d	Droplet
i	ith species, or inner wall surface, or ith coordinate direction
j	jth particle, or jth particle trajectory, or jth coordinate direction
g	Gas
k	kth phase, or kth moment, or kth species
m	Mixture
o	Outer wall surface
p	Particle
w	Wall

Operators

∇	m^{-1}	Nabla operator in Cartesian coordinates; $\nabla = \frac{\partial}{\partial x}\delta_x + \frac{\partial}{\partial y}\delta_y + \frac{\partial}{\partial z}\delta_z$
$\bar{\phi}$	Various	Favre-averaged generic dependent variable

ACKNOWLEDGMENTS

The author wishes to acknowledge Professor Hong Yong Sohn for his supervision, teaching and guidance through the course of this research work; and for the opportunities to collaborate in and learn from other research areas.

The author thanks the members of the supervisory committee: Dr. Terry A. Ring, Dr. Raj K. Rajamani, Dr. Michael S. Moats, and Dr. Moo Eob Choi, for examining this dissertation and providing thoughtful advice. The author is especially grateful to Dr. Terry A. Ring for many helpful technical discussions.

The author's appreciation is extended to his colleagues and friends: Taegong Ryu, Jin Won Choi, Silvia E. Perez-Fontes and Tyler Bronson, with whom the author enjoyed numerous technical discussions regarding computational fluid dynamics.

The author is particularly thankful to Dr. Manuel Pérez Tello for his unconditional friendship and for encouraging the author's desire to pursue doctoral studies abroad.

The author is grateful for the 2011 Graduate Research Fellowship granted to him by the University of Utah through The Graduate School. Acknowledgments are also due to the Computer Aided Design and Engineering (CADE) Laboratory of the University of Utah for its support with ANSYS FLUENT CFD code.

The author expresses his gratitude to CONACYT (Consejo Nacional de Ciencia y Tecnología / National Council of Science and Technology) of México for providing financial support, under scholarship No. 188864, for part of his doctoral program. Special thanks are due to Mr. Jose Luis García Ruíz for being the intermediary between the author and CONACYT during the application process.

Acknowledgments are due to the Korea Institute of Geoscience and Mineral Resources (KIGAM) and to the Resource Recycling R&D Center of Korea for providing the financial support for the modeling work presented in Section 4. Special thanks are due to Dr. Hee Dong Jang for providing experimental data and for helpful technical discussions.

Acknowledgments are also due to the American Iron and Steel Institute (AISI) for providing financial support, under the AISI CO_2 Breakthrough Program, for the work presented in Section 6.

The author also acknowledges ANSYS Inc. for providing the ANSYS FLUENT software used in this work.

Last but not least, the author expresses his profound gratitude to his wife and colleague, Silvia E. Perez-Fontes, and to his daughter, Victoria Olivas-Perez, for all their love and support. Special thanks are due to the author's families in México for their continuing and unselfish support during the past several years.

1. INTRODUCTION

Chemically reacting gas-particle flows refer to material production technologies in which solid particles are generated in a gas stream and/or gas-solid reactions take place. Examples of such processes include the chemical vapor synthesis (CVS) of inorganic nanopowders and the flash smelting and converting of copper sulfides. This work is related to three reacting gas-particle flows: chemical vapor synthesis (CVS) of tungsten carbide and aluminum nanopowders, flame synthesis of silica nanopowder, and a novel flash ironmaking process based on the direct gaseous reduction of iron oxide concentrate.

Nanopowders exhibit extreme physical and chemical properties due to their small sizes and large surface-to-volume ratios. High catalytic activities, special optical properties, electrical and magnetic characteristics, and other properties such as flowability, plasticity, and toughness make nanopowders suitable for a wide range of novel applications (Gleiter, 1989; Thölén, 1994). Specific applications require certain particle morphology, average particle size, and particle size distribution (PSD) (Jang, 2001). The control of these characteristics is one of the technical challenges in the design and operation of nanopowder production technologies.

A novel flash ironmaking process is under development at the University of Utah (Choi and Sohn, 2010). This technology aims at significantly increasing energy productivity (by reducing energy consumption) and reducing environmental emissions,

especially CO_2 emissions, versus the conventional blast furnace route. In flash ironmaking, iron oxide concentrate particles are injected directly into a refractory-lined reaction chamber, and they are reduced in flight by hot reducing gases produced by the partial combustion of natural gas, hydrogen or syngas.

1.1 Problem Statement

In chemically reacting gas-particle flows, the product characteristics, such as particle size in vapor-phase nanopowder synthesis and reduction degree in flash ironmaking, are determined by the reaction temperature, residence time of the particles in the reaction zone, gas composition, and aerodynamic condition inside the reactor. These operating conditions originate from complex interactions between various physical and chemical processes occurring inside the reactor; namely, fluid flow, heat and mass transfer, gas-phase reactions, and the reaction of solid particles with a hot gaseous stream. Therefore, the understanding of these rate processes plays a critical role in the development and operation of these processes.

The study of chemically reacting gas-particle flows solely by traditional experimental methods is difficult because these methods do not provide information on the local gradients of velocity, temperature, and species concentrations, which the reacting particles experience inside the reactor. Furthermore, the mechanisms of formation, growth, and transport of nanoparticles in high-temperature reactors with fast chemical reactions and complex fluid dynamics are still not well understood. Consequently, the experimental design and scale-up of these processes is a rather difficult

task. Mathematical models based on fundamental principles will thus provide a critical tool in the study and application of such processes.

Therefore, the present investigation was aimed at contributing to the understanding of chemically reacting gas-particle flows by computational fluid dynamic (CFD) modeling. The synthesis of tungsten carbide, aluminum, and silica nanopowders and a novel flash ironmaking process were studied and analyzed.

1.2 Research Objectives

The overall objective of this work was to develop a three-dimensional mathematical model based on computational fluid dynamics (CFD) capable of describing the various processes occurring in chemically reacting gas-particle flows. Upon completion, the model can be used as a design, scale-up and operational optimization tool for such processes.

To achieve the overall objective, the following specific objectives were established:

1. Develop a realistic modeling approach to represent the formation and growth of nanoparticles in the vapor phase;
2. Validate the computational model with the available experimental data;
3. Simulate and analyze the chemical vapor synthesis of tungsten carbide and aluminum nanopowders, and the flame synthesis of silica nanopowder;
4. Use the computational model to analyze the gas-phase distributions of velocity, temperature, and species concentrations; and the motion and temperature of iron oxide concentrate particles inside a lab flash reactor.

2. ELEMENTS OF COMPUTATIONAL FLUID DYNAMIC (CFD) MODELING*

The mathematical modeling of the various processes involved in chemically reacting gas-particle flows requires quantitative description of the coupled gas-phase transport and chemical reaction rate equations; that is, fluid flow, heat and mass transfer, and reaction kinetics. For modeling vapor-phase nanopowder synthesis, the particle size distribution (PSD) is computed by solving the population balance model (PBM) coupled with kinetic expressions for the rates of particle nucleation and growth. For modeling the flash ironmaking reactor, iron oxide concentrate particles are treated from a Lagrangian viewpoint. In this section, the elements of computational fluid dynamic (CFD) modeling relevant to chemically reacting gas-particle flows are presented.

2.1 Gas-Phase Equations

The generic transport equation, in steady state, can be written in the following form:

$$\nabla \cdot \rho_g \vec{u} \phi - \nabla \cdot \Gamma_\phi \nabla \phi = S^\phi \tag{2-1}$$

*This section contains a significant part from Sohn, H. Y.; Olivas-Martinez, M.; Perez-Fontes, S. E. Mathematical Modeling of Nanopowder Production by Vapor-Phase Processes. In *Mathematical Modeling;* Brennan, C. R., Ed.; Nova Science Publishers, Inc.: Hauppauge, NY, 2011; pp 179-208; for which permission to use has been obtained from Nova Science Publishers, Inc., copyright owner.

where ϕ represents the generic dependent variable, Γ_ϕ is the effective transport coefficient, and S^ϕ is the source term. Other symbols are defined in the Nomenclature.

Table 2.1 presents the governing equations (ANSYS, 2011; Bird et al., 2007) considered in this work. Favre averaging, a density-weighted average used for compressible flows, was used in the turbulence modeling and is represented by

$$\bar{\phi} = \frac{1}{\bar{\rho}} \int_t^{t+t_0} \rho(t)\phi(t)dt \tag{2-2}$$

where $\bar{\phi}$ is the Favre-averaged generic dependent variable, ρ and $\bar{\rho}$ are the density and its time-averaged value, respectively, and t_0 is a long enough time to obtain a smooth-averaged value.

The description of gas-phase processes comes from the conservation of overall mass [Equation (2-3)], momentum in the three Cartesian directions [Equation (2-4)], turbulent kinetic energy [Equation (2-5)], turbulent dissipation rate [Equation (2-6)], energy [Equation (2-7)], and species continuity [Equation (2-8)]. The standard k-ε turbulence model (Launder and Spalding, 1972) was used. Heat transfer by radiation was described using the discrete ordinate (DO) model (ANSYS, 2011).

2.2 Heat Transfer

Due to the importance of the transport of heat in chemically reacting gas-particle flows, this subsection provides a comprehensive description of the mathematical treatments for representing the phenomena of conduction, convection, and radiation within the gas phase and between the gas and particle phases. It also presents the various boundary conditions used in the solution of the resulting model equations.

Table 2.1: Gas-Phase Equations.

Overall continuity:	$\frac{\partial}{\partial x_i}\left(\overline{\rho}_g \overline{u}_i\right) = S_p^m$	(2-3)
Momentum:	$\frac{\partial}{\partial x_j}\left(\overline{\rho}_g \overline{u}_i \overline{u}_j\right) = -\frac{\partial \overline{p}}{\partial x_i} + \frac{\partial}{\partial x_j}\left[\mu_g\left(\frac{\partial \overline{u}_j}{\partial x_j} + \frac{\partial \overline{u}_j}{\partial x_i} - \frac{2}{3}\delta_{ij}\frac{\partial \hat{u}_i}{\partial x_i}\right)\right] + \frac{\partial}{\partial x_j}\left(-\overline{\rho}_g \overline{u_i' u_j'}\right) + \overline{\rho}_g \overline{g}_i$	(2-4)
Turbulent kinetic energy:	$\frac{\partial}{\partial x_j}\left(\overline{\rho}_g \overline{u}_j k\right) = \frac{\partial}{\partial x_j}\left[\left(\mu_g + \frac{\mu_t}{\sigma_k}\right)\frac{\partial k}{\partial x_j}\right] + G_k + \overline{\rho}_g \varepsilon - Y_M + S_k$	(2-5)
Turbulent dissipation rate:	$\frac{\partial}{\partial x_j}\left(\overline{\rho}_g \overline{u}_j \varepsilon\right) = \frac{\partial}{\partial x_j}\left[\left(\mu_g + \frac{\mu_t}{\sigma_\varepsilon}\right)\frac{\partial \varepsilon}{\partial x_j}\right] + C_{1\varepsilon}\frac{\varepsilon}{k}G_k - C_{2\varepsilon}\overline{\rho}_g \frac{\varepsilon^2}{k} + S_\varepsilon$	(2-6)
Energy:	$\frac{\partial}{\partial x_i}\left(\overline{\rho}_g \overline{u}_i h_g\right) = \frac{\partial}{\partial x_i}\left(k_g \frac{\partial T_g}{\partial x_i}\right) + Q_{rg}^h + S_p^h + S_g^h$	(2-7)
Species:	$\frac{\partial}{\partial x_i}\left(\overline{\rho}_g \overline{u}_i \overline{Y}_k\right) = \frac{\partial}{\partial x_i}\left[\left(\overline{\rho}_g D_{k-mix} + \frac{\mu_t}{Sc_t}\right)\frac{\partial \overline{Y}_k}{\partial x_j}\right] + S_k$	(2-8)
Reynolds stresses:	$-\overline{\rho}_g \overline{u_i' u_j'} = \mu_t\left(\frac{\partial \overline{u}_i}{\partial x_j} + \frac{\partial \overline{u}_j}{\partial x_i}\right) - \frac{2}{3}\left(\overline{\rho}_g k + \mu_t \frac{\partial \overline{u}_k}{\partial x_k}\right)\delta_{ij}$	(2-9)

2.2.1 Gas-Phase Energy Equation

Equation (2-7) is the governing equation for the transport of heat in the gas phase under steady state. The term on the left-hand side represents heat transfer by convection (bulk flow). The first term on the right-hand side (RHS) represents heat transfer by conduction. The second term on the RHS denotes the net radiative heat transfer to the gas phase. The third term on the RHS is a source term due to the net heat transfer by convection and chemical reaction from the particles to the gas phase. The last term on the RHS represents a source term due to gas-phase chemical reactions such as combustion. The solution of Equation (2-7) yields the temperature (T_g) distribution of the gas phase inside the reactor.

2.2.2 Particle-Phase Energy Equation

The temperature variation of the reacting particles is described from a Lagrangian viewpoint in which particle trajectories are tracked from their injection points. The equation of energy for a particle moving along its trajectory is

$$m_p c_p \frac{dT_p}{dt} = h_s A_p \left(T_g - T_p\right) + Q_{rp} + H_r \qquad (2\text{-}10)$$

where T_p is the particle temperature. Equation (2-10) states that the rate of change of the particle temperature is due to the heat transfer by convection (first term on the RHS), the net radiation received by the particles (second term on the RHS), and the net rate of heat production (third term on the RHS) by the reactions involving the particles. Equation (2-10) assumes that there is negligible internal resistance to heat transfer, which means that a particle is at uniform temperature throughout. In typical CFD applications, Equation (2-10) is part of a coupled set of ordinary differential equations (ODE's) for the velocity,

temperature and composition of the particle along its trajectory with its residence time as the independent variable. The heat transfer correlation needed to calculate the convective heat transfer coefficient (h_s) can be found in the literature (Szekely et al., 1976).

The exchange of energy between the reacting particle and the gas phase is computed as follows

$$(S_p^h)_{V_{\text{cell}}} = \frac{1}{V_{\text{cell}}} \sum_{j=1}^{J} [\dot{n}_p [(m_p h_p)^{in} - (m_p h_p)^{out}]]_j + Q_{rp}^h \qquad (2\text{-}11)$$

where J is the number of particle trajectories, V_{cell} is the volume of a computational cell, and $\dot{n}_p$ is the particle number flow rate of the jth trajectory, and Q_{rp}^h is the net radiative heat-transfer rate to the particle phase, per unit volume. The terms containing $(m_p h_p)^{in}$ and $(m_p h_p)^{out}$ correspond to the particle enthalpy entering and leaving the cell, respectively. The resulting source term S_p^h is then added to the gas-phase energy equation [Equation (2-7)].

2.2.3 Radiation Modeling

Thermal radiation plays a significant role as a heat transfer mechanism at the sufficiently high temperatures characteristic of most chemically reacting gas-particle flows. Furnace walls emit, absorb, and reflect radiation from or to particles, gas or other furnace walls, and may have a nonuniform temperature distribution.

The modeling of radiation considers the effects of gas, walls, and particles on the radiation field. The radiative transfer equation (RTE) is set up for an absorbing, emitting and scattering media, and is solved in a full three-dimensional framework. The nonuniform temperature distribution of the furnace walls can also be accounted for.

The objective of the radiation model is to compute the coupling terms Q_{rg}^{h} and Q_{rp}^{h} appearing in Equations (2-7) and (2-10), respectively. These terms are computed from the following expressions:

$$Q_{rg}^{h} = k_{a,g}G - 4\pi e_g \tag{2-12}$$

$$Q_{rp}^{h} = k_{a,p}G - 4\pi e_p \tag{2-13}$$

where G is the total incident flux or irradiance. Equations (2-12) and (2-13) represent the difference between absorption and emission rates from each phase per unit volume. The Lagrangian term Q_{rp} in Equation (2-10) is computed by

$$Q_{rp} = \frac{Q_{rp}^{h}}{n_p} \tag{2-14}$$

where n_p is the number density of the particle phase.

The modeling of radiation consists of tracking the path followed by a beam of radiation. If I is the incoming radiation of this beam, its rate of change along a path length of size dS is given by

$$\frac{dI}{dS} = -(k_{a,g} + k_{a,p} + k_s)I + e_g + e_p + \frac{k_s}{4\pi}\int_{\omega''=4\pi} I''\Phi(\Omega'',\Omega)d\omega'' \tag{2-15}$$

The first term on the RHS represents the loss of radiant energy due to absorption by gas, absorption by particles and out-scattering. The second and third terms are generation terms due to gas and particle emission, respectively. The fourth term accounts for incoming radiation in the direction Ω due to scattering from all directions Ω'' in the surroundings. The following assumptions were incorporated: (1) the medium is gray, (2) particle surface is diffuse, and (3) Kirchhoff's law is valid (i.e., the absorption and emission coefficients of the medium are equal). The walls of high-temperature furnaces

were assumed to be opaque, gray, and diffuse. Thus, only the surface emissivity values were needed to specify the radiative properties of the wall. Once these are specified, the intensity of radiation per steradian leaving the wall is obtained from the following relationship:

$$I_{\Omega,w} = \varepsilon_w \left(\frac{\sigma T_w^4}{\pi} \right) + \frac{(1-\varepsilon_w) q_w}{\pi} \tag{2-16}$$

which consists of emission from the surface and the intensity reflected by the surface. The incident heat flux at the wall surface is obtained by integrating the incoming radiation from all directions to the surface

$$q_w = \int_{\omega''=2\pi} (\mathrm{n} \cdot \Omega'') I'' d\omega'' \tag{2-17}$$

Upon solving Equation (2-15), the irradiation term G, which is required to compute the coupling terms Q_{rg}^h and Q_{rp}^h, is computed as follows

$$G = \int_{\omega''=4\pi} I'' d\omega'' \tag{2-18}$$

The solution of the radiative transfer equation [Equation (2-15)] requires the specification of the radiation properties of the medium (gas and particles) and participating surfaces. The absorption coefficient of the gas phase is computed from the Bouguer-Lambert law:

$$k_{a,g} = \frac{-1}{L_e} \ln(1-\varepsilon_g) \tag{2-19}$$

There are a number of sources for obtaining emissivity values of gases at different temperatures (Hottel et al., 2008). The ANSYS FLUENT software uses the weighted-

sum-of-gray-gases model (WSGGM) to compute the gas emissivity as a function of temperature and partial pressures (ANSYS, 2011).

The absorption coefficient of the particles is computed by assuming independent absorbing spheres. The total coefficient is expressed as the summation over the contributions from all particles in a computational cell:

$$k_{a,p} = \frac{\pi}{4} \sum_{j=1}^{J} \varepsilon_p n_j d_j^2 \tag{2-20}$$

2.2.4 Boundary Conditions for the Gas-Phase Energy Equation

High-temperature reactors commonly have composite walls consisting of layers of refractory, insulating, and metallic materials. If necessary, heat transfer by conduction through the composite wall can be computed. In such a case, boundary conditions are only needed at the external wall surface with matching conditions at the inner wall surface. The temperature in the wall layers is computed by solving heat conduction equations through them.

Thus, the matching condition at the inner surface and the boundary condition at the outer surface, respectively, are

$$h_{eff}(T_g - T_w)\Big|_i + \varepsilon_w (q_w - \sigma T_w^4)\Big|_i = -k_{refractory} \frac{\partial T}{\partial n_w}\Big|_i \tag{2-21}$$

and

$$h_f (T_w - T_b)\Big|_o + \varepsilon_{steel} \sigma (T_w^4 - T_\infty^4)\Big|_o = -k_{steel} \frac{\partial T}{\partial n_w}\Big|_o \tag{2-22}$$

The second term on the left-hand side of Equation (2-21) represents the net radiation heat transfer to the surface wall, that is, the emitted energy minus the absorbed

incident energy. To compute the convective coefficient (h_{eff}) at the inner surface [Equation (2-21)], the ANSYS FLUENT software uses the law-to-the-wall approach which has been extensively used for industrial turbulent flows (ANSYS, 2011). The law-of-the-wall approach consists of (a) a linear law for the thermal conduction sublayer where conduction is important, and (b) a logarithmic law for the turbulent region where effects of turbulence dominate conduction. The convective coefficient (h_{eff}) is then computed as follows

$$h_{eff} = \frac{\rho_g c_{p,g} C_\mu^{1/4} k_P^{1/2}}{T^*} \tag{2-23}$$

where T^* is a dimensionless temperature defined by

$$T^* \equiv \frac{(T_w - T_P)\rho_g c_{p,g} C_\mu^{1/4} k_P^{1/2}}{q} = \begin{cases} \Pr y^* & (y^* < y_T^*) \\ \Pr_t \left[\frac{1}{\kappa} \ln(Ey^*) + P \right] & (y^* > y_T^*) \end{cases} \tag{2-24}$$

For laminar flows, Equations (2-23) and (2-24) reduce to case of conduction in the fluid side. The procedure of applying the law-of-the-wall approach for computing the wall temperature is as follows. Once the physical properties of the fluid being modeled are specified, its molecular Prandtl number is computed. The thermal sublayer thickness y_T^* is then computed from the intersection of the linear and logarithmic profiles and stored. During an iteration, depending on the y^* value at the near-wall cell, either the linear or the logarithmic profile is applied to compute the wall temperature T_w.

In Equation (2-22), the convective coefficient (h_f) can be calculated using heat-transfer correlations such as those given in Geankoplis (1993). For example, the expression to compute h_f for a vertical cylinder when the product of the Grashof and

Prandtl numbers is larger than 10^9 is given by

$$h_f = 1.24\Delta T^{1/3} \tag{2-25}$$

where ΔT is the positive temperature difference between the outer wall and surrounding fluid. The second term on the left-hand side of Equation (2-22) corresponds to the net energy leaving the outer surface by radiation. In a typical CFD problem, the RTE is not solved in the fluid side adjacent to the outer wall. Instead, simplified expressions are used to calculate the net radiation term. In ANSYS FLUENT, this is computed using the net-radiation method (Siegel and Howell, 1992) which is a simple approach commonly used to solve radiation exchange problems between gray-diffuse surfaces inside enclosures.

The radiative transfer equation [Equation (2-15)] is solved using the discrete ordinate method (ANSYS, 2011) in which a hypothetical sphere constructed around a computational cell is discretized in a finite number of angular directions (solid angles). Each arbitrary direction is called a discrete ordinate. The radiation intensity within each solid angle is assumed to be uniform. The radiation intensity throughout the computational domain is obtained by writing Equation (2-15) for each discrete ordinate and solving the resulting integrodifferential equations using a finite volume method. The Lagrangian energy equation [Equation (2-10)] is an ordinary differential equation and is solved by standard numerical techniques, such as Runge-Kutta methods.

2.3 Gas-Phase Reaction Kinetics

Gas-phase reactions often take place in chemically reacting gas-particle flows and can be represented by the following general form:

$$a\mathrm{A(g)} + b\mathrm{B(g)} = c\mathrm{C(g)} + d\mathrm{D(g)} \tag{2-26}$$

When the gas-phase reactions occur at high temperatures and the mixing of the gaseous reactants takes place inside the reactor, it is customary to assume that the intrinsic gas-phase reaction rate is very fast and thus the reaction rate is controlled by the turbulent mixing. In this work, unless indicated differently, the rate of gas-phase reactions was calculated using the eddy-dissipation model (EDM) developed by Magnussen and Hjertager (1977).

In the EDM, the net production rate of the *i*th species due to reaction *r* ($R_{i,r}$) is determined by the lowest reaction rate of the following expressions (ANSYS, 2011):

$$R_{i,r} = \nu'_{i,r} M_{w,i} A \rho \frac{\varepsilon}{k} \min_R \left(\frac{Y_R}{\nu'_{R,r} M_{w,R}} \right) \tag{2-27}$$

$$R_{i,r} = \nu'_{i,r} M_{w,i} A B \rho \frac{\varepsilon}{k} \frac{\sum_P Y_P}{\sum_j^N \nu''_{j,r} M_{w,j}} \tag{2-28}$$

where $\nu'_{i,r}$ is the stoichiometric coefficient for the *i*th species in the *r*th reaction, $\nu''_{j,r}$ is the stoichiometric coefficient for the *j*th product species in the *r*th reaction, $M_{w,i}$ is the molecular weight of the *i*th species, ρ is the density of the gas mixture, Y_R is the mass fraction of any reactant species, Y_P is the mass fraction of any product species, A is an empirical constant equal to 4.0, and B is an empirical constant equal to 0.5.

2.4 Population Balance Model

The population balance model (PBM), which incorporates particle transport, nucleation, growth and coagulation, describes the change in particle size distribution function in terms of the particle size and the local spatial position (Friedlander, 2000). At steady state, the PBM is expressed by

$$\nabla \cdot n\vec{v}_m + \frac{\partial}{\partial d_p}(nG) = B_{coag} - D_{coag} \tag{2-29}$$

where n is the particle number density function, d_p is the particle size (diameter), and G is the particle size growth rate. The first term on the left-hand side of Equation (2-29) denotes the convection of particles due to the flow field. The second term represents the growth of particles by gas-to-particle conversion; that is, nucleation, vapor condensation, and surface reaction. The terms on the right-hand side describe particle coagulation and are given by

$$B_{coag} = \frac{1}{2}\int_o^{d_p} \beta(d_p', (d_p^3 - d_p'^3)^{1/3}) n(d_p') n((d_p^3 - d_p'^3)^{1/3}) dd_p' \tag{2-30}$$

and

$$D_{coag} = n(d_p)\int_o^{\infty} \beta(d_p', d_p) n(d_p') dd_p' \tag{2-31}$$

Equation (2-30) represents the rate of birth of particles of size d_p by collisions between particles of sizes $d_p - d_p'$ and d_p'. The term $1/2$ prevents counting the collisions twice, once each for the two colliding particles. Equation (2-31) describes the rate of death of particles of size d_p by collisions of particle of size d_p with particles of all sizes.

The boundary condition at $d_p = 0$ for the integration of the second term on the left-hand side of Equation (2-29) is given by

$$n\big|_{d_p=0} = \frac{J}{G} \tag{2-32}$$

where J represents the rate of nucleation of particles.

The particle size distribution function can be expressed in terms of the appropriate moments of the size distribution. The *k*th moment (m_k) is defined by (Friedlander, 2000)

$$m_k = \int_o^\infty d_p^k n(d_p) dd_p \tag{2-33}$$

The zeroth moment (m_0) is equal to the total number of particles per unit volume of the system. The first moment (m_1) gives the sum of the particle diameters per unit volume. The second moment (m_2) gives, when multiplied by π, the total surface area of particles per unit volume. The third moment (m_3) yields, when multiplied by $\pi/6$, the total volume of particles per unit volume.

2.5 Kinetics of Particle Nucleation and Growth

For systems in which particles are produced by gas-phase reactions, the processes of particle nucleation and growth need to be described by the population balance model given by Equation (2-29). In this subsection, these expressions will be introduced along with the underlying theories.

2.5.1 Particle Nucleation

Homogeneous nucleation is responsible for the formation of particles from the vapor phase. In this process, vapor atoms or molecules are transformed into solid particles in a supersaturated vapor without the presence of a foreign phase. In chemical vapor synthesis where vapor-phase reactions produce the condensable product, the homogeneous nucleation process can be controlled by the degree of supersaturation (Seinfeld and Pandis, 2006) or it can be reaction-limited (Bolsaitis et al., 1987; Kodas and Hampden-Smith, 1999) depending on the vapor pressure of the condensed phase.

The classical theory of homogeneous nucleation describes the formation of nuclei when the degree of supersaturation of the vapor phase is the driving force. In a supersaturated vapor, small clusters of the secondary phase containing a few molecules are produced. However, most of them are thermodynamically unstable and disappear in a short time. Only a small fraction of these clusters will grow to a size large enough to produce nuclei; that is, the clusters have reached their critical size. In a cluster of critical size, molecules condense and evaporate at the same rate. Hence, those clusters that have a size larger than the critical size will probably continue to grow and become particles. In contrast, clusters with a size smaller than the critical size will evaporate. The critical nucleus size is predicted by the Kelvin equation (Friedlander, 2000) given by

$$d_p^* = \frac{2\sigma}{\rho_M RT \ln S} \tag{2-34}$$

where the supersaturation ratio S is defined as follows:

$$S = \frac{p_i}{p_i^\circ} \tag{2-35}$$

The nucleation rate is therefore the net number of clusters formed per unit time that has a size larger than the critical size and can be computed by (Seinfeld and Pandis, 2006)

$$J = \left(\frac{2\sigma}{\pi m_i}\right)^{1/2} \left(\frac{v_i N_i^2}{S}\right) \exp\left(-\frac{16\pi}{3} \frac{v_i^2 \sigma^3}{(k_B T)^3 (\ln S)^2}\right) \tag{2-36}$$

Reaction-controlled nucleation occurs when the vapor pressure of the nucleating species is very low (Bolsaitis et al., 1987; Kodas and Hampden-Smith, 1999; Rao and McMurry, 1989). Under such conditions, the nucleation process is indistinguishable from the chemical reactions that produce the condensable products. In other words, every

monomer formed by chemical reaction in the vapor phase can be regarded as a thermodynamically stable particle. Thus, the nucleation rate can be represented by the rate of formation of the vapor product.

2.5.2 Particle Growth by Gas-to-Particle Conversion

In vapor-phase synthesis, the growth of particles by gas-to-particle conversion occurs as the result of vapor condensation and/or surface reactions. In vapor condensation, particles grow when vapor atoms or molecules condense on the particle surface. The rate of change of the particle diameter with time by condensation is computed by the Fuchs-Sutugin interpolation formula (Friedlander, 2000; Seinfeld and Pandis, 2006), given by

$$G = \frac{dd_p}{dt} = \frac{4V_i D_{i\text{-}mix}}{d_p RT}\left(p_{i,b} - p_i^{\circ}\right)\left\{\frac{0.75\alpha_v(1+\mathrm{Kn})}{\mathrm{Kn}^2 + \mathrm{Kn} + 0.283\mathrm{Kn}\alpha_v + 0.75\alpha_v}\right\} \qquad (2\text{-}37)$$

where α_v is the vapor collision efficiency factor, Kn is the Knudsen number defined as

$$\mathrm{Kn} = \frac{6D_{i\text{-}mix}}{\bar{c}_i d_p} \qquad (2\text{-}38)$$

and $\bar{c}_i$ is the mean molecular velocity of the *i*th species expressed as follows

$$\bar{c}_i = \left(\frac{8k_B T}{\pi m_i}\right)^{1/2} \qquad (2\text{-}39)$$

Equation (2-37) represents the growth rate in the entire range of Knudsen numbers. When $\mathrm{Kn} << 1$, Equation (2-37) becomes the diffusion equation for the continuum regime. When $\mathrm{Kn} >> 1$, Equation (2-37) becomes the growth equation in the free-molecule regime.

In certain systems, chemical reactions on the particle surface are the important mechanism for particle growth. The overall growth rate by this mechanism under the combined control of surface chemical reaction and mass transfer can be expressed by:

$$G_{overall} = \frac{G_{rxn} G_m}{G_{rxx} + G_m} \tag{2-40}$$

where G_{rxn} and G_m are, respectively, the growth rates under the control of chemical reaction kinetics and mass transfer.

In terms of the particle growth rate, the rate of increase of the solid mass per unit volume of the system in the overall mass balance is given by

$$Source = (\pi / 2) m_2 G_{overall} \rho_p \tag{2-41}$$

where m_2 is the second moment of the PSD, which represents the total surface area of particles per unit volume of the gaseous mixture.

2.5.3 Particle Coagulation

The coagulation of small particles takes place predominantly by Brownian motion. In this mechanism, two particles collide and stick together to form a new, larger particle. Coagulation increases the average particle size, decreases the total particle number density, and conserves the total particle mass concentration and volume (Friedlander, 2000). Particle coagulation is modeled by assuming that the rate of particle coalescence is infinitely fast, allowing the particle to always be spherical. The collision frequency function is computed using the Fuchs interpolation formula given by (Seinfeld and Pandis, 2006)

$$\beta(d_{p1},d_{p2})=\frac{2\pi(D_1+D_2)(d_{p1}+d_{p1})}{\dfrac{d_{p1}+d_{p2}}{d_{p1}+d_{p2}+2(g_1^2+g_2^2)^{1/2}}+\dfrac{8(D_1+D_2)}{\alpha_p(\bar{c}_1^2+\bar{c}_2^2)^{1/2}(d_{p1}+d_{p2})}} \tag{2-42}$$

where D_j is the diffusion coefficient of the *j*th particle given by

$$D_j=\frac{k_B T C_c}{3\pi\mu d_{p,j}}; \tag{2-43}$$

C_c is the slip correction factor defined by

$$C_c=1+\frac{2\lambda}{d_{p,j}}\left(1.257+0.4\exp\left(-\frac{1.1d_{p,j}}{2\lambda}\right)\right); \tag{2-44}$$

$\bar{c}_j$ is the mean thermal velocity of the *j*th particle expressed by the following equation:

$$\bar{c}_j=\left(\frac{8k_B T}{\pi m_j}\right)^{1/2}; \tag{2-45}$$

g_j is the transition parameter given by

$$g_j=\frac{1}{3d_{p,j}l_j}\left[\left(d_{p,j}+l_j\right)^3-\left(d_{p,j}^2+l_j^2\right)^{3/2}\right]-d_{p,j}; \tag{2-46}$$

l_j denotes the mean free path of the *j*th particle as follows

$$l_j=\frac{8D_j}{\pi\bar{c}_j}; \tag{2-47}$$

and α_p is the particle collision efficiency factor. Equation (2-42) allows the calculation of the collision frequency function from the free-molecule regime ($\mathrm{Kn}>>1$) to the continuum regime ($\mathrm{Kn}<<1$), including the transition ($\mathrm{Kn}\approx 1$) stage. The parameter g_j is related to the average distance that a particle travels in the transition regime ($\mathrm{Kn}\approx 1$) before colliding with another particle.

2.6 Mixture Model

The mixture model solves the governing equations for the mixture (gas and particles) and the continuity equation for the particulate phase. The generic mixture transport equation, in steady state, can be written in the following form:

$$\nabla \cdot \rho_m \vec{v}_m \phi_m - \nabla \cdot \Gamma_{\phi,m} \nabla \phi_m = S_{\phi,m} \tag{2-48}$$

The density of the mixture is given by

$$\rho_m = \sum_{k=1}^{n} \alpha_k \rho_k \tag{2-49}$$

where α_k is the volume fraction of the *k*th phase and ρ_k is the density of the *k*th phase. In general, any mixture-phase dependent variable is computed by

$$\phi_m = \sum_{k=1}^{n} \alpha_k \phi_k \tag{2-50}$$

The mixture-phase equations take on the same form as the gas-phase transport equations given in Table 2.1.

The continuity equation for the particulate phase is given by

$$\nabla \cdot \alpha_p \rho_p \vec{v}_p = S_p \tag{2-51}$$

where α_p is the particle volume fraction, ρ_p is the particle density, $\vec{v}_p$ velocity vector of the particle phase and S_p represents the mass generation or addition in the particulate phase from the interaction with the gas phase, for example, particle nucleation and growth.

2.7 Discrete-Phase Model

The discrete-phase model treats the particulate phase from a Lagrangian viewpoint in which the particle trajectories are tracked from its injection point in the flow field. The model consists of a coupled set of ordinary differential equations (ODEs) for the particle velocity, temperature, and composition along its trajectory with its residence time as the independent variable. In addition, the exchange of momentum, energy and mass between the particle and the gas phase is computed. The resulting source terms are then added to the gas-phase equations. The model formulation includes the following assumptions: (a) spherical particles and (b) no particle-particle interaction.

The equation of motion for a particle in a Lagrangian framework is given by

$$\frac{d\vec{v}}{dt} = \frac{3}{4} C_D \frac{\rho_g}{\rho_p} \frac{1}{d_p} |\vec{u} - \vec{v}|(\vec{u} - \vec{v}) + \frac{(\rho_p - \rho_g)}{\rho_p} \vec{g} \tag{2-52}$$

where $\vec{u}$ is the gas velocity vector, $\vec{v}$ is the particle velocity vector, ρ_g is the gas density, ρ_p is the particle density, d_p is the particle diameter, C_D is the drag coefficient and $\vec{g}$ is the gravity vector. Equation (2-52) states that the rate of change of particle momentum is equal to the forces acting upon it. The first and second terms on the right-hand side represent the aerodynamic drag force and the gravitational acceleration, respectively. The equation of energy [Equation (2-10)] for a particle moving along its trajectory was discussed in Subsection 2.3.2.

2.8 Numerical Solution

The numerical solution of the transport equations subject to the appropriate boundary conditions was obtained within the framework of the ANSYS FLUENT CFD

code (ANSYS, 2011). The reactor geometries were discretized on nonuniform grids. A finite volume approach was used to solve the gas-phase equations [Equations (2-3) through (2-8)] and the mixture model [Equations (2-48) through (2-51)]. The population balance model (PBM) [Equation (2-29)] was solved by means of the quadrature method of moments (QMOM) (McGraw, 1997), which allows the direct tracking of the particle size distribution (PSD).

3. COMPUTATIONAL MODELING OF CHEMICAL VAPOR SYNTHESIS OF WC NANOPOWDER FROM TUNGSTEN HEXACHLORIDE

3.1 Background

Due to the much desired properties of high hardness and good wear resistance, tungsten carbide (WC) is widely used as a hard material in many industrial applications such as metalworking, drilling and mining industries under high pressure, high temperature, and corrosive environments. Its mechanical properties such as hardness, compressive strength, and transverse rupture depend on the composition and microstructural parameters such as the grain size of WC (Fang et al., 2005; Lee and Kang, 2006; Petersson and Ågren, 2004; Upadhyaya, 2002). Previous investigations (Fu et al., 2001; Nersisyan et al., 2005; Shi et al., 2006; Wahlberg et al., 1997; Wu et al., 2004; Zawrah, 2007; Zhu and Manthiram, 1996) have shown that the reduction of tungsten carbide grain size provides a significant improvement in the mechanical properties. The reduction in size of the structure also means an increase in the dislocation density and the amount of grain boundaries per unit area. Furthermore, nanosized powder changes the response during sintering, which results in lower sintering temperatures and shorter times to attain dense but small grain size structures. Therefore, the production of nanosized tungsten carbide powder is critical.

Nanosized tungsten carbide powders have been produced by various methods such as thermo-chemical spray drying process (Ban and Shaw, 2002; McCandlish et al., 1992), mechanical alloying (MA) (Hasanpour et al. 2007; Liu et al. 2006; Mi and Courtney, 1997), and chemical vapor condensation (CVC) (Chang et al., 1994). Chemical vapor synthesis (CVS) is a process for making fine solid particles by the vapor-phase chemical reactions of precursors. The chemical vapor synthesis (CVS) process, which has been applied to the synthesis of metallic and intermetallic powders at the University of Utah, has several advantages in producing nanograined powders having compositional uniformity, high purity, and small grain sizes (Sohn and PalDey, 1998a, 1998b, 1998c).

The CVS process of WC is carried out by the reduction of vapor-phase reactant precursors and subsequent carburization by gaseous carburization agents such as hydrocarbon (Ryu et al., 2007). Tungsten metal compounds such as tungsten hexachloride (WCl_6) (Won et al., 1993), tungsten hexafluoride (WF_6) (Fitzsimmons and Sarin, 1995), and tungsten hexacarbonyl ($W(CO)_6$) (Kim and Kim, 2004) are generally favored as the precursor because of their relatively low volatilization temperatures as well as the ease of reduction by hydrogen. Several carburizing agents have also been used such as propane (C_3H_8), acetylene (C_2H_2), and methane (CH_4). Methane is the most commonly used carburizing agent because it is easy to control the amount of carbon reacted and is stable up to a high temperature (Gao and Kear, 1995).

Although considerable work to produce nanosized WC powder by gas-phase reactions has been conducted, the mechanism of WC particle formation is not well understood. This process is very complicated, with mass and heat transfer, chemical reactions, and particle formation all occurring simultaneously.

In this work, the model formulated in Section 2 was used to simulate the chemical vapor synthesis of WC in a tubular reactor. Tungsten hexachloride (WCl_6) was used as the precursor with reactant gases hydrogen (H_2) and methane (CH_4) as the reducing and carburizing agents, respectively. The CVS process was simulated to obtain the velocity profile, temperature profile, species concentration distribution, and particle size distribution (PSD).

3.2 Model Formulation

The partial differential equations shown in Table 2.1 were solved to compute the velocity, temperature, and species concentration distributions inside the tubular reactor. The following assumptions were made: (a) steady state, (b) axisymmetrical two-dimensional laminar flow, and (c) spherical particles.

A total of six species considered in this simulation were WCl_6, CH_4, H_2, WC, HCl, and Ar based on the following overall chemical reaction:

$$WCl_6(g) + CH_4(g) + H_2(g) = WC(s) + 6HCl(g) \qquad (3\text{-}1)$$

3.2.1 Particle Formation and Growth

The mechanisms of nucleation and growth of WC nanoparticles from the simultaneous reduction and carburization of WCl_6 are not well understood. The Kelvin equation [Equation (2-34)] predicts that the material critical nucleus size of tungsten carbide is smaller than the size of its monomer. Thus, every WC monomer formed by chemical reaction [Equation (3-1)] in the vapor phase can be regarded as a thermodynamically stable particle. Moreover, particle growth takes place by chemical

vapor deposition reactions of the precursors at the particle surface. This modeling method for particle formation and growth will be referred to as chemical kinetic approach.

The nucleation of WC particles is therefore driven by the kinetics of the chemical reaction [Equation (3-1)] that produces the monomers, and it is expressed by

$$J = k_n N C_{WCl_6} C_{CH_4} \tag{3-2}$$

where J is the nucleation rate, k_n is the nucleation rate constant, N is the Avogadro constant, and C_{WCl_6} and C_{CH_4} are the molar concentrations of WCl_6 and CH_4, respectively.

The growth of WC nanoparticles takes place due to the chemical reaction of WCl_6 and CH_4 at the particle surface and the mass transfer of precursors to the particle surface. The growth rate due to the surface chemical reaction (Bolsaitis et al., 1987; Kodas and Hampden-Smith, 1999) is thus given by

$$G_{rxn} = 2 v_{WC} k_g C_{WCl_6} C_{CH_4} \tag{3-3}$$

where v_{WC} is the molar volume of tungsten carbide (0.0125 m^3 $kmol^{-1}$) and k_g represents the growth rate constant. It is noted that even though hydrogen is included in the overall reaction [Equation (3-1)], the proposed rate expressions for particle nucleation [Equation (3-2)] and growth [Equation (3-3)] are not dependent on the hydrogen concentration, because hydrogen is in large excess.

The volumetric rate of growth of a particle under mass transfer control, assumed to be driven by the limiting reactant (WCl_6), is given by

$$\frac{dv_p}{dt} = v_{WC} \cdot \pi d_p^2 \cdot k_m \cdot \left(C_{WCl_6,b} - C_{WCl_6,s} \right) \tag{3-4}$$

where v_p is the particle volume, k_m is the convective mass transfer coefficient, and the subscripts *b* and *s* represent bulk and surface, respectively.

The growth rate in terms of the particle diameter is obtained by substituting the expression for the particle volume ($v_p = \pi d_p^3 / 6$) into [Equation (3-4)], which yields

$$\frac{dd_p}{dt} = 2v_{\mathrm{WC}} \cdot k_m \cdot C_{WCl_6,b} \,. \tag{3-5}$$

In this work, it was assumed that concentration of WCl_6(g) at the particle surface is negligible compared to its concentration at the bulk since Reaction (3-5) has a large equilibrium constant (e.g., $K = 3.5 \times 10^{22}$ at 1273 K).

The mass transfer coefficient (k_m) is calculated based on the assumption that the particles and gaseous mixture move at the same velocity. Thus, the correlation of Ranz and Marshall (Szekely et al., 1976) gives

$$\mathrm{Sh} = \frac{k_m \bar{d}_p}{D_{\mathrm{WCl_6}}} = 2.0 \tag{3-6}$$

where Sh is the Sherwood number, $D_{\mathrm{WCl_6}}$ is the diffusion coefficient of WCl_6(g) in the gaseous mixture, and $\bar{d}_p = m_1 / m_0$ is the number-weighted average particle diameter. By substituting Equation (3-6) into Equation (3-5), the particle growth rate under mass transfer control is given by

$$G_m = 4v_{\mathrm{WC}} \frac{D_{\mathrm{WCl_6}}}{\bar{d}_p} C_{\mathrm{WCl_6},b} \tag{3-7}$$

The overall growth rate G under the combined control of surface chemical reaction and mass transfer is given by Equation (2-40).

In this work, the growth rate under the control of surface chemical reaction was the limiting factor, which means that the growth rate under the control of mass transfer is much faster than the growth rate by the surface chemical reaction. This is because gas-solid mass transfer is extremely fast for small particles.

3.3 Simulation Strategy

Initial three-dimensional simulation runs considering the entire reactor geometry for reaction temperatures of 1473, 1573 and 1673 K showed that all species were mixed homogeneously before the reactant gases approached a temperature of 873, 993, and 1108 K, respectively. These values were then adopted as the inlet temperatures. The three-dimensional simulations also showed that the flow of the gaseous mixture became symmetric around the reactor centerline before the reaction zone was reached. This evidence allowed us to do the simulation in a two-dimensional axisymmetrical framework.

The governing equations (Table 2.1) were solved using the following boundary conditions in cylindrical coordinates:

Inlet: At $z = 0$ $\quad v_r = 0,\ v_z = v_o,\ T = T_o,\ Y_i = Y_{io},\ m_i = 0 \quad$ for all r (3-8)

Wall: At $r = \dfrac{D}{2}$

$$v_r = v_z = 0, \frac{\partial Y_i}{\partial r} = \frac{\partial m_i}{\partial r} = 0$$

$$T = \begin{cases} az + b & 0 \le z \le z_1 \\ T_{wall} & z > z_1 \end{cases} \qquad z_1 = 12\,\text{cm} \tag{3-9}$$

Outlet: At $z = H$ $\quad \dfrac{\partial v_r}{\partial z} = \dfrac{\partial v_z}{\partial z} = \dfrac{\partial T}{\partial z} = \dfrac{\partial Y_i}{\partial z} = \dfrac{\partial m_i}{\partial z} = 0 \quad$ for all r (3-10)

Symmetry: At $r = 0$ $\quad \dfrac{\partial v_r}{\partial r} = \dfrac{\partial v_z}{\partial r} = \dfrac{\partial T}{\partial r} = \dfrac{\partial Y_i}{\partial r} = \dfrac{\partial m_i}{\partial r} = 0 \quad$ for all r (3-11)

where v_r and v_z are the velocity components in the rth and zth directions, respectively, D is the reactor diameter, H is the reactor length, v_0 is the plug-flow velocity calculated based on the experimental volumetric flow rates, and a and b are the empirical constants obtained by fitting the experimentally measured temperature profile to a linear equation.

Figure 3.1 shows the experimental wall temperature profile and the simulated reactor geometry. The inner diameter and total length of reactor simulated were 5.4 and 38 cm, respectively. The temperature at the inlet was 1108 K and increased to 1273 and 1673 K after 3.5 cm and 12 cm in distance from the inlet, respectively. According to Hojo and coworkers (1978) and Ryu and coworkers (2007), substantial WC formation from WCl_6 starts to occur above 1273 K. The mass fractions of WCl_6, CH_4, and H_2 at the inlet were 0.0347, 0.0483, and 0.0152, respectively, based on the experimental conditions (Ryu et al., 2007).

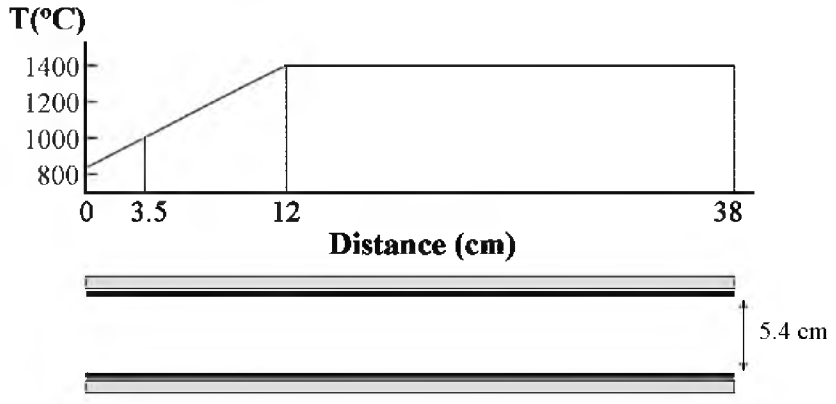

Figure 3.1: Reactor wall temperature profile and geometry.

3.4 Determination of Nucleation Rate and Growth Rate Constants

The nucleation rate and growth rate are important factors that determine the particle size distribution (PSD). However, it is extremely difficult to determine the nucleation rate constant (k_n) and growth rate constant (k_g) by experimental measurements for the synthesis of WC nanoparticles. Because there were no measured data on these parameters, we first obtained these parameters by adjusting k_n and k_g and comparing the computed results with experimental measurements of average particle diameter and the coefficient of variation in some cases. In the experimental results, in which WC was synthesized under the conditions of WCl_6 feeding rate of 0.04 g min^{-1}, H_2 flow rate of 0.25 L min^{-1} (298 K, 86.1 kPa), CH_4 flow rate of 0.1 L min^{-1} (298 K, 86.1 kPa), and Ar flow rate of 0.75 L min^{-1} (298 K, 86.1 kPa), and the reaction temperature of 1673 K, the average particle diameter based on specific surface area measurement was 22.2 nm and the coefficient variation (C.V.) was 0.18.

The experimental average particle diameter (d_{exp}) was calculated from the measured specific surface area (S_{exp}) under the assumption of spherical shape

$$d_{exp} = \frac{6}{\rho_s S_{exp}} \tag{3-12}$$

The coefficient of variation (c.v.) means the degree of spread of the size distribution. It is represented as the ratio of the standard deviation of a distribution (σ) to its mean size (μ), as follows

$$\text{c.v.} = \frac{\sigma}{\mu} \tag{3-13}$$

In the simulation results, the average particle size based on specific surface area was derived as follows

$$d_{3,2} = \frac{6}{\rho_p S_a} = \frac{6}{\rho_p \dfrac{A_p}{\rho_p V_p}} = \frac{6V_p}{A_p} = \frac{6 \cdot \dfrac{\pi}{6} \int_0^\infty d_p^3 n(d_p) dd_p}{\pi \cdot \int_0^\infty d_p^2 n(d_p) dd_p} = \frac{m_3}{m_2} \tag{3-14}$$

where $d_{3,2}$ is the computed local average particle diameter, S_a is the calculated specific surface area of the particles, A_p is the total surface area density of the particles, V_p is the total volume density of the particles, and m_2 and m_3 are the second and third moments of the PSD, respectively.

The local coefficient of variation (c.v.) is calculated in terms of the moments of the PSD as follows (Randolph and Larson, 1988)

$$\text{c.v.} = \frac{\left(\dfrac{1}{m_2} \int_0^\infty (d_p - d_{3,2}) d_p^2 n(d_p) dd_p \right)^{1/2}}{d_{3,2}} = \left(\frac{m_4 m_2}{m_3^2} - 1 \right)^{1/2} \tag{3-15}$$

To compare the experimental and simulation results, the corresponding average particle diameter of all the particles leaving the reactor was calculated from the computed radius-dependent flow rates of particle volume and surface area, as follows

$$\bar{d}_{3,2} = \frac{M_3}{M_2} \tag{3-16}$$

where $M_k = \int m_k \vec{v}_m \cdot d\vec{A}$ is the flow rate of the *k*th moment of the PSD, $\vec{v}_m$ is the mixture velocity vector, and $\vec{A}$ is the cross-sectional area vector. Here, it was assumed that the particles have the same velocity as the gas. Similarly, the C.V. at the reactor outlet is given by

$$\text{C.V.} = \left(\frac{M_4 M_2}{M_3^2} - 1 \right)^{1/2} \tag{3-17}$$

However, in the experimental results, the particle diameter measurement was from the rather limited number of particles. In view of this, the average particle size and the concentration of WCl_6 at outlet were used as the criteria to determine the values of k_n and k_g based on the experimental results that the reaction was complete at this temperature indicating no unreacted WCl_6.

Table 3.1 shows the computed average particle size, coefficient of variation and % unreacted WCl_6 at the reactor outlet for various sets of kinetic constants k_n and k_g. Even though the simulation with the set of constants $k_n = 10^{-1}$ m^3 $kmol^{-1}$ s^{-1} and $k_g = 400$ m^4 $kmol^{-1}$ s^{-1} resulted in an average particle diameter of 22.5 nm, which is closer to the experimental value of 22.2 nm, the kinetic constants $k_n = 1\times10^{-1}$ m^3 $kmol^{-1}$ s^{-1} and $k_g =$ 300 m^4 $kmol^{-1}$ s^{-1} that provide an average particle diameter of 20.4 nm were selected since they were obtained from a converged numerical solution.

From Table 3.1, it is observed that the calculated average particle diameter increases as the growth rate constant increases at a constant nucleation rate. Thus, to find the best set of nucleation rate and growth rate constants, first the nucleation rate constant was fixed and the growth rate constant varied based on the experimental average particle diameter and the concentration of unreacted WCl_6 at the outlet. From the results, if the nucleation rate constant was smaller than 1×10^{-1} m^3 $kmol^{-1}$ s^{-1}, the concentration of unreacted WCl_6 at the reactor outlet increased even though the predicted average particle diameter matched the experimental value. In addition, if this nucleation rate constant was higher than 1×10^{-1} m^3 $kmol^{-1}$ s^{-1}, it resulted in an unstable numerical process, leading to a divergent solution.

Table 3.1: Nucleation Rate and Growth Rate Constants with Average Particle Diameter and Unreacted WCl_6 Concentration.

k_n ($m^3 \cdot kmol^{-1} \cdot s^{-1}$)	k_g ($m^4 \cdot kmol^{-1} \cdot s^{-1}$)	$\bar{d}_{3,2}$ (nm)	C.V.	% unreacted WCl_6 at outlet	Comments on computation
1×10^{-5}	4.0×10^{0}	12.2	0.33	98	converged
	7.2×10^{0}	21.4	0.33	90	converged
	4.0×10^{1}	64.5	0.37	33	converged
1×10^{-4}	4.0×10^{0}	11.6	0.33	85	converged
	9.6×10^{0}	21.2	0.35	50	converged
	4.0×10^{1}	44.3	0.41	22	converged
1×10^{-3}	4.0×10^{0}	9.2	0.35	54	converged
	2.2×10^{1}	22.3	0.42	20	converged
	4.0×10^{1}	30.3	0.47	10	converged
1×10^{-2}	4.0×10^{0}	6.5	0.37	33	converged
	6.0×10^{1}	21.9	0.56	1.2×10^{-3}	converged
	4.0×10^{2}	39.6	0.66	2.4×10^{-14}	converged
1×10^{-1}	4.0×10^{0}	4.3	0.41	22	converged
	3.0×10^{2}	**21.7**	**0.67**	**1×10^{-19}**	converged
	4.0×10^{2}	23.9	0.67	1×10^{-23}	unstable, residuals do not approach asymptotic value
1	1.2×10^{3}	`-	-	-	divergence detected
10	6.0×10^{3}	-	-	-	not converged

Experimental conditions: WCl_6 (0.04 g min^{-1}), CH_4 (0.1 L min^{-1} at 298 K and 86.1 kPa), H_2 (0.25 L min^{-1} at 298 K and 86.1 kPa), Ar (0.75 L min^{-1} at 298 K and 86.1 kPa), and reaction temperature (1673 K).
Measured average particle diameter based on specific surface area: 22.2 nm.
WCl_6 is completely consumed in the reaction.

3.5 Distributions of Temperature, Velocity and Species Concentration

From the initial computed results (Table 3.1), the nucleation rate constant (k_n) and growth rate constants (k_g) were fixed at 1×10^{-1} m^3 $kmol^{-1}$ s^{-1} and 300 m^4 $kmol^{-1}$ s^{-1}, respectively, for further simulation work.

Figure 3.2 shows the temperature contours with fixed nucleation and growth rate constants obtained numerically as mentioned above. The velocity magnitude of the mixture is shown in Figure 3.3, in which the total linear velocity of reactant gases at the inlet was 0.0298 m s^{-1}. The inlet and the plateau wall temperatures were 1108 and 1673 K, respectively. The highest velocity was observed at the center of reaction zone and the lowest velocity was observed near the wall of the reactor. These converged results are reasonable as far as the temperature and velocity profile are concerned.

Figure 3.4 presents the contours and profile of WCl_6 mole fraction. The latter was generated by computing the local cup-mixing mole fraction as a function of the axial

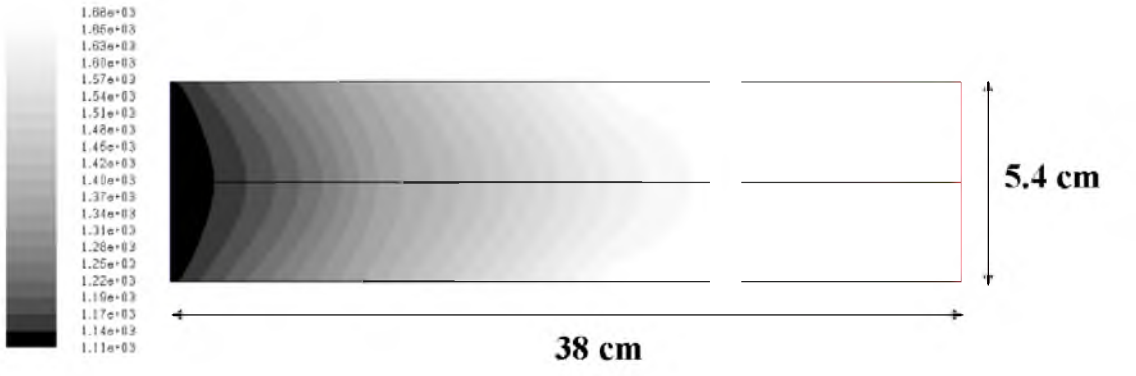

Figure 3.2: Contours of temperature inside the reactor. Values in kelvins.

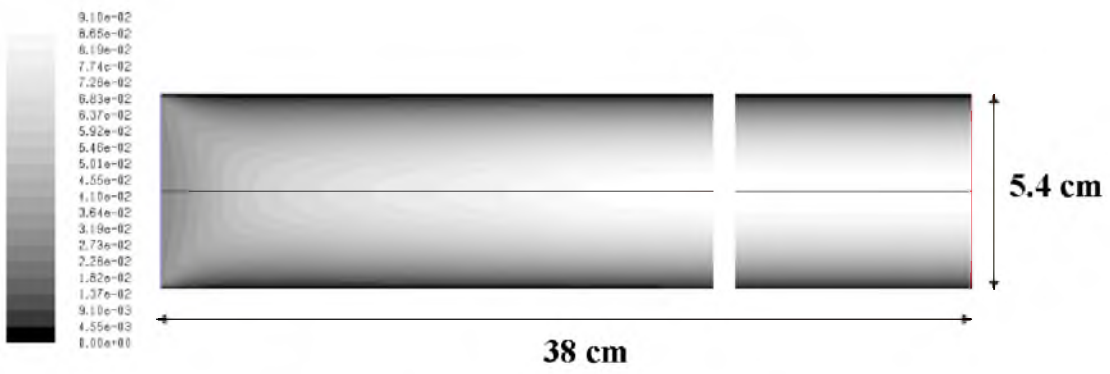

Figure 3.3: Contours of velocity magnitude. Values in m s^{-1}.

position. A cup-mixing quantity is a flow-weighted average (Bird et al., 2007). In this work, the cup-mixing WCl_6 mole fraction as a function of the axial position was obtained by

$$x_{\mathrm{WCl_6,\,cup\text{-}mix}}(z) = \frac{\int_0^{2\pi}\int_0^{\bar{R}} \rho_m(r,z)v_{m,z}(r,z)x_{\mathrm{WCl_6}}(r,z)r\,dr\,d\theta}{\int_0^{2\pi}\int_0^{R} \rho_m(r,z)v_{m,z}(r,z)r\,dr\,d\theta} \tag{3-18}$$

where ρ_m is the local mixture density, $v_{m,z}$ is the local axial component of the mixture velocity vector, and $x_{\mathrm{WCl_6}}$ is local WCl_6 mole fraction.

Figure 3.4 shows that WCl_6 was consumed completely and that the reaction with hydrogen and methane occurred rapidly. Figures 3.5 and 3.6 show the contours of mole fractions of hydrogen and methane, respectively, in which they are seen to be consumed rapidly for WC formation. These results were reasonable considering that the reaction in the vapor phase occurs rapidly.

The contours and profiles of nucleation rate and growth rate, obtained by applying

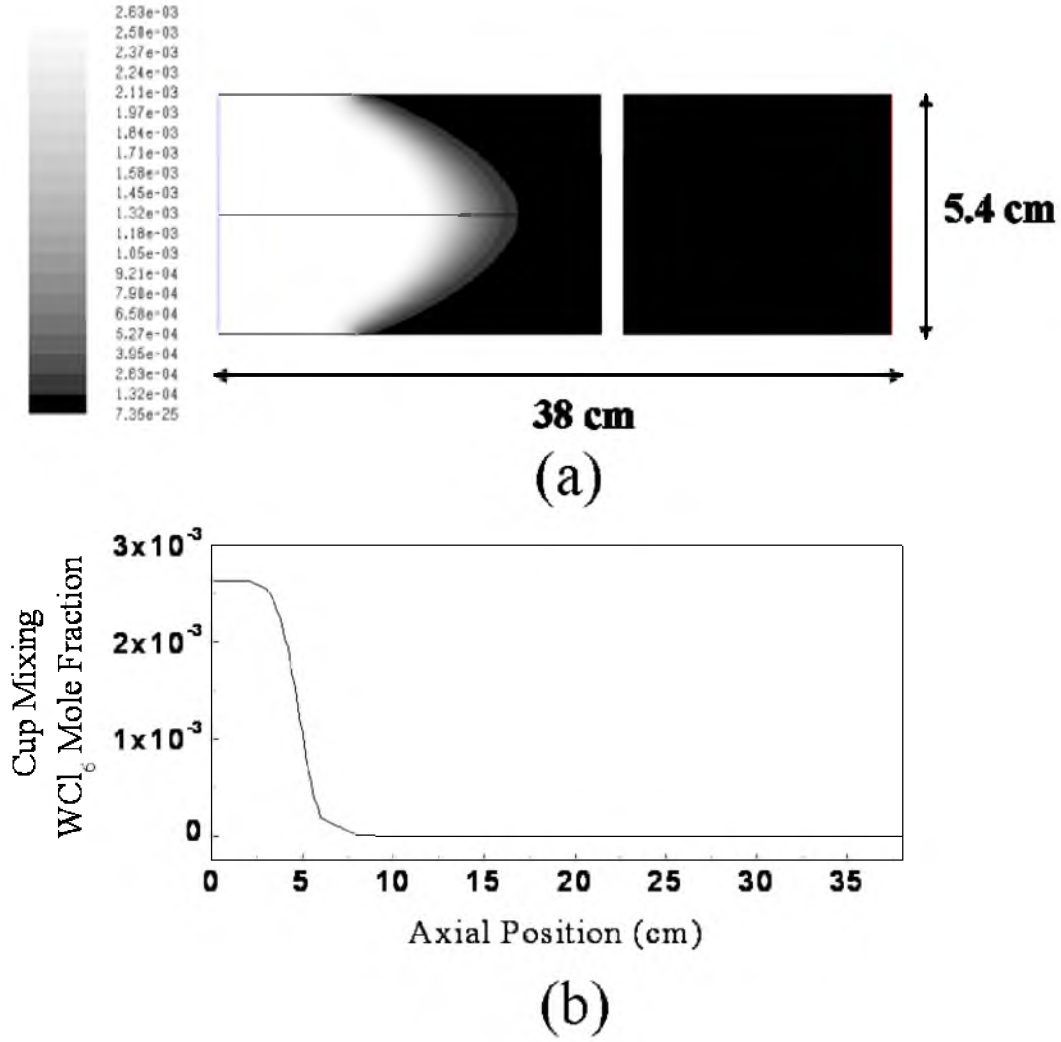

Figure 3.4: Contours (a) and profile (b) of mole fraction of WCl_6.
Profile is based on the local cup-mixing value.

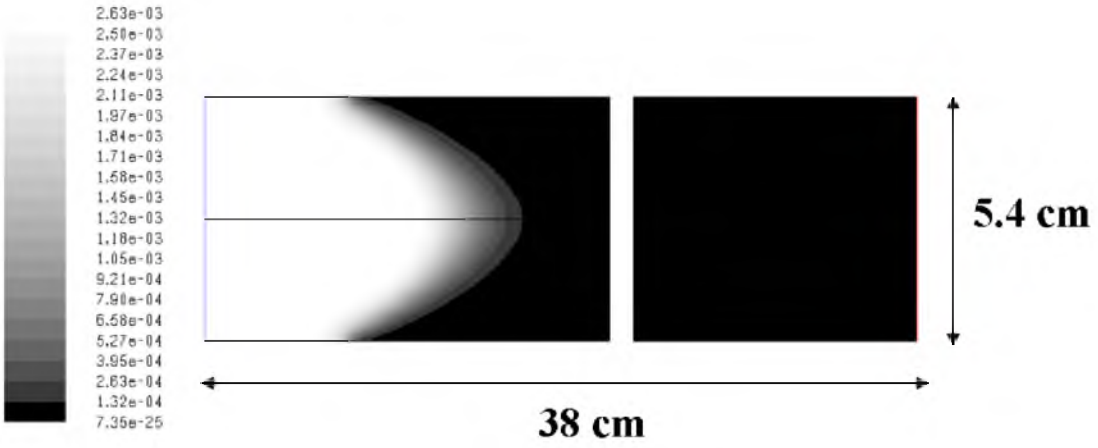

Figure 3.5: Contours of H_2 mole fraction.

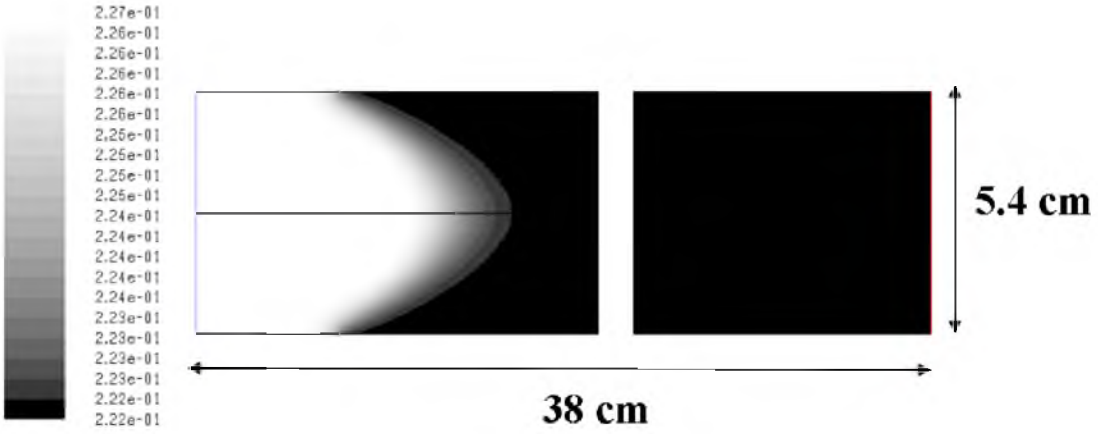

Figure 3.6: Contours of CH_4 mole fraction.

the kinetic constants as discussed previously, are shown in Figures 3.7 and 3.8. These results were in good agreement with the WC formation reaction, in which the nucleation and growth of WC particles start rapidly above 1273 K. It is also clearly seen that the nucleation and growth of WC particles take place rapidly as $WCl_6(g)$ is consumed.

Since the flow regime in this reactor is laminar, there is a parabolic velocity profile. As a result, the mass transfer by convection (bulk flow) in the axial direction is faster in the center of the reactor than near the walls. Therefore, at a fixed axial position the concentration of precursors at the center is higher than that near the wall (as shown in Figures 3.4 through 3.6). Consequently, the rates of nucleation and growth of the particles, which are proportional to the concentration of the gaseous precursors, are higher at the center and lower near the wall, at a fixed axial position.

3.6 Particle Size Distribution

As mentioned earlier, the nucleation rate and growth rate constants are two important factors that determine the particle size distribution. Figure 3.9 shows the contours and profile of computed WC average particle diameter in the tubular reactor, in which the nucleation rate constant and growth rate constant were fixed at 1×10^{-1} m^3 $kmol^{-1}$ s^{-1} and 300 m^4 $kmol^{-1}$ s^{-1}, respectively. It is observed that the largest average particle diameter of 41 nm was near the reactor wall, where the linear velocity of mixture is lowest, and the average particle diameter at the outlet was 21 nm, as shown in Figure 3.9(a). Figure 3.9(b) shows the profile of the local average particle diameter along the axial position. The decrease of its value at around 4 cm can be explained by the

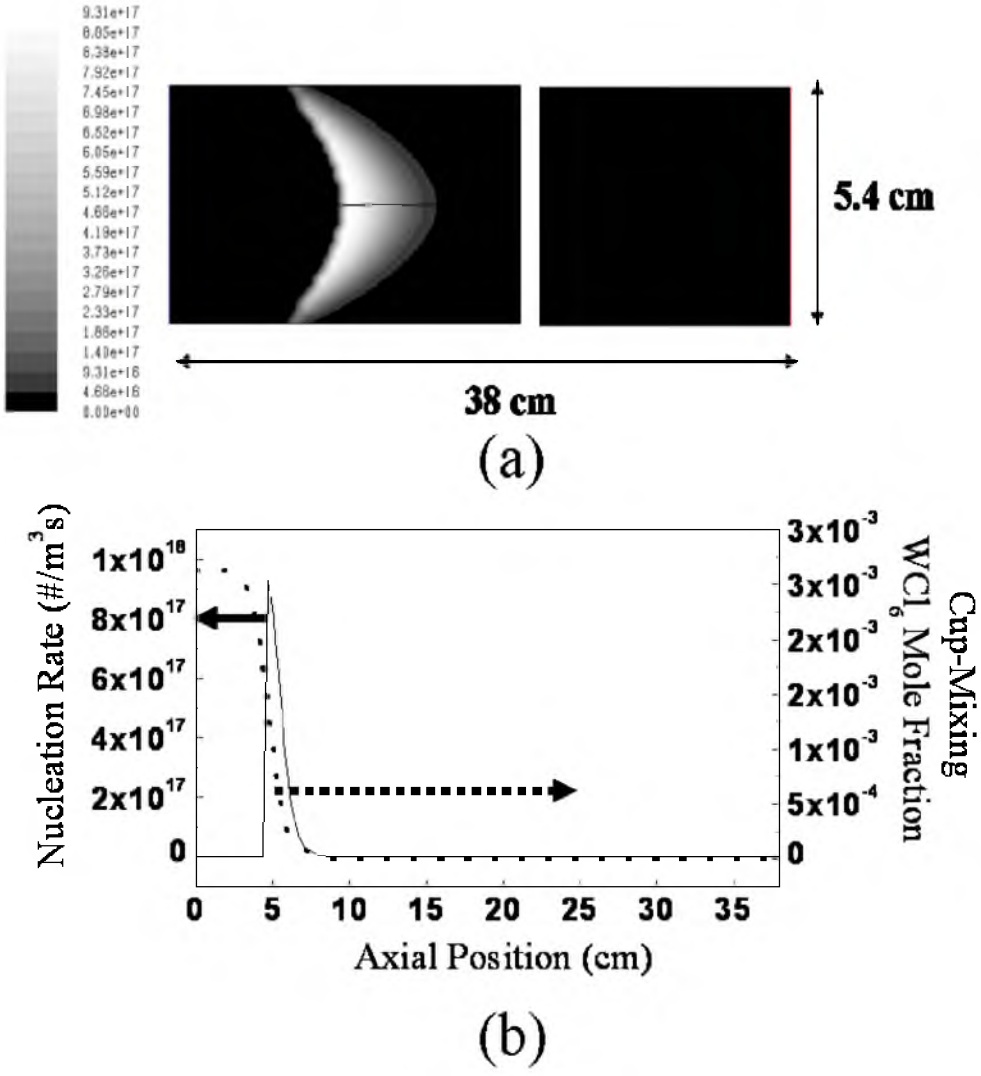

Figure 3.7: Contours (a) and profile (b) of nucleation rate of WC particles. Values in $\#\cdot m^{-3}\ s^{-1}$. Profile is based on the local value along the reactor axis.

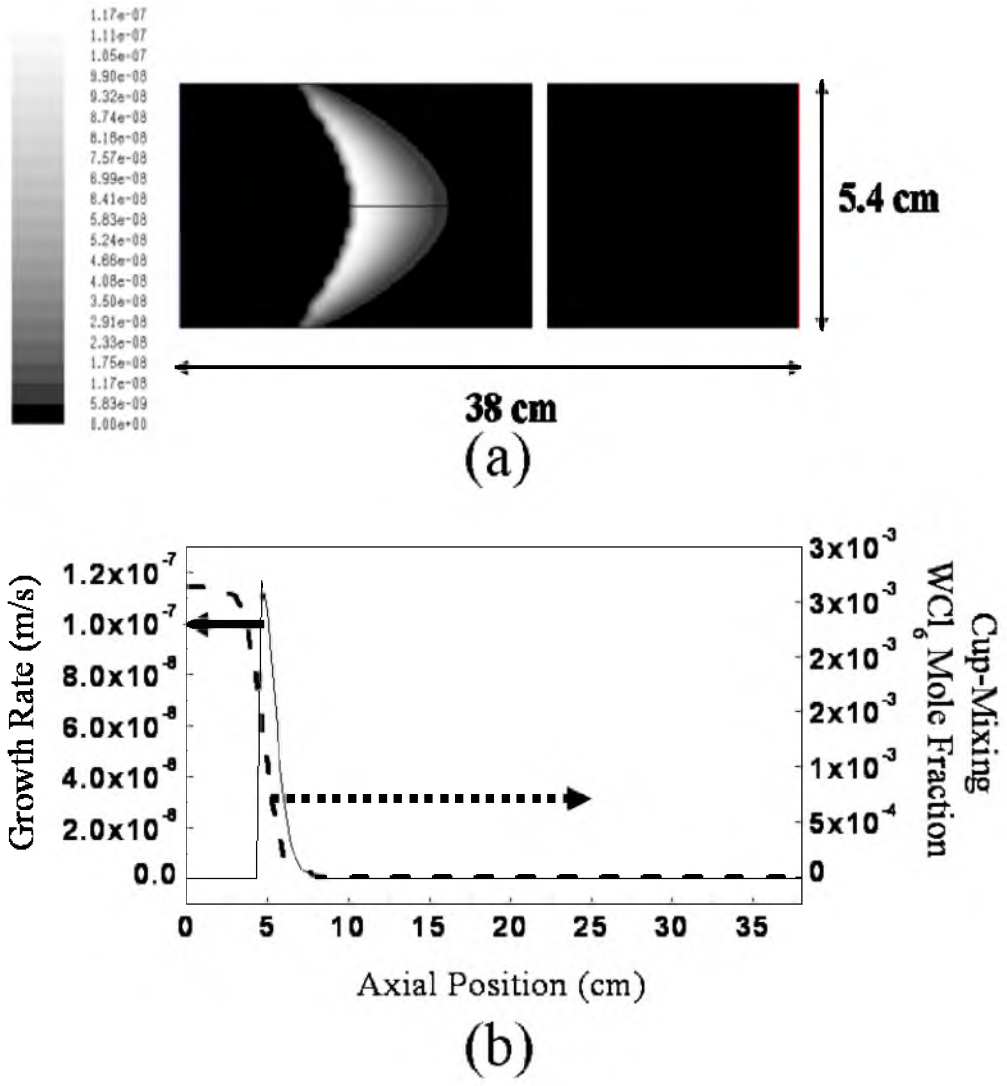

Figure 3.8: Contours (a) and profile (b) of growth rate of WC particles. Values in m s^{-1}. Profile is based on the local value along the reactor axis.

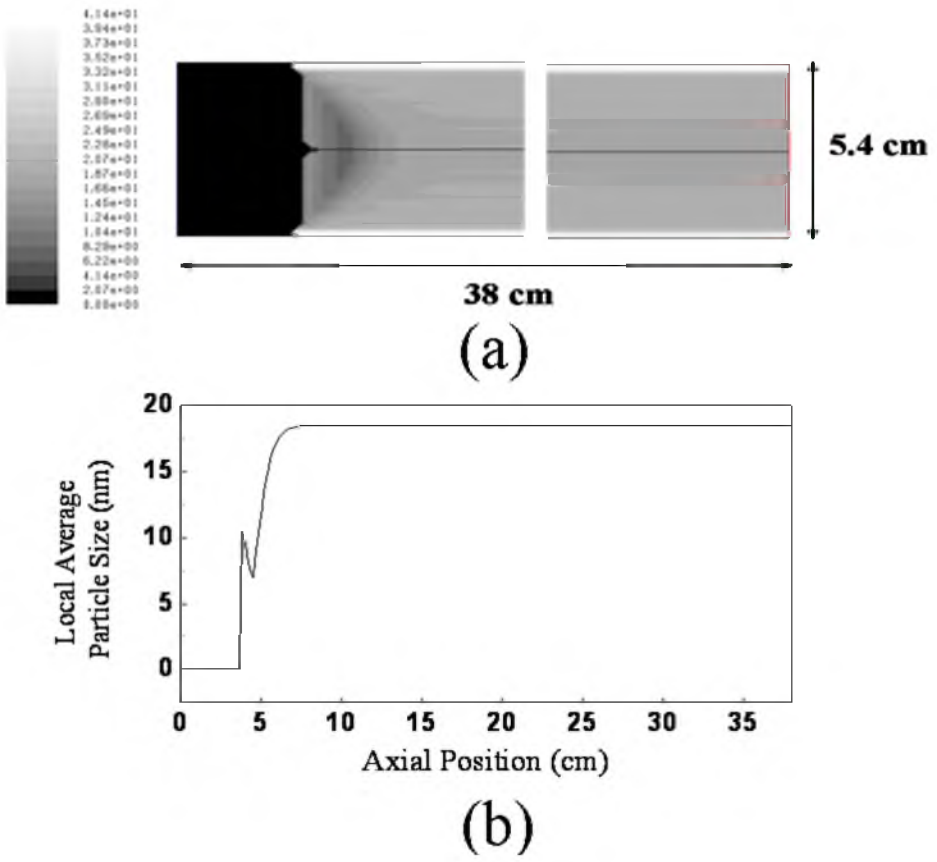

Figure 3.9: Contours (a) and profile (b) of WC average particle diameter. Values in nm. Profile is based on the local value along the reactor axis.

nucleation rate being a maximum at this point; that is, the number of particles is a maximum.

If more detailed experimental data on the average particle diameter are available, additional model verification and validation can be conducted. The nucleation rate (k_n) and growth rate (k_g) constants obtained at 1673 K of reaction temperature were applied to verify these constants by the comparison of the average particle diameter obtained at different CH_4/WCl_6 molar ratios in the reaction. Figure 3.10 shows the variation of the average particle diameter as a function of the CH_4/WCl_6 molar ratio.

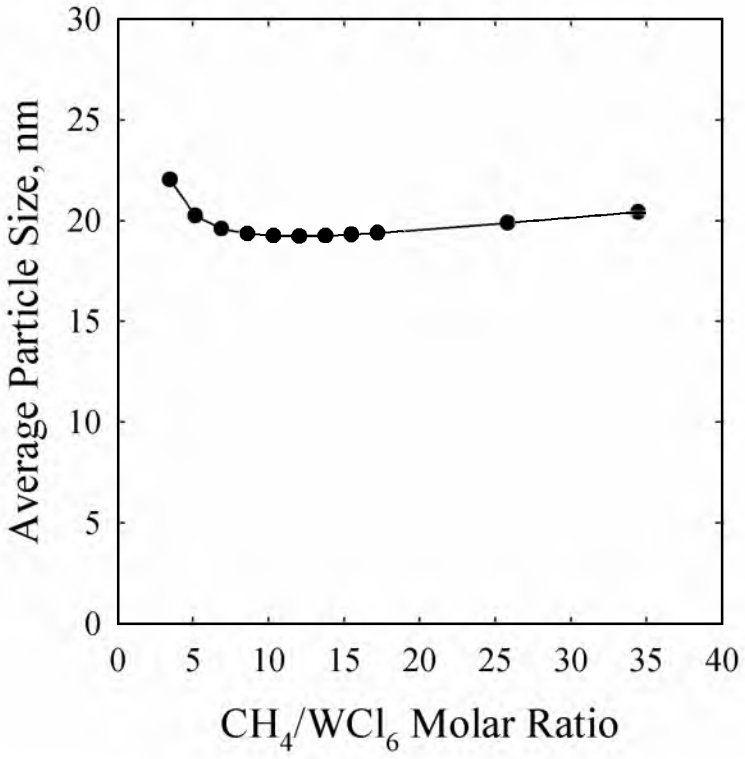

Figure 3.10: Effect of the CH_4/WCl_6 molar ratio on the average particle diameter.

For all CH_4/WCl_6 ratios, the methane concentration was varied at a fixed WCl_6 concentration and methane was always in excess. The simulation results show that the average particle diameter first decreased with the increase of the methane concentration up to the CH_4/WCl_6 ratio of 12 where the smallest average particle diameter was observed. After this ratio, the average particle diameter increased with the increase in methane concentration. This behavior is the result of the coupled interaction among the rates of nucleation and growth of WC particles as the concentration of methane increased. However, it is important to note that the variation of the average particle diameter with CH_4/WCl_6 ratio was not large. The experimentally determined average particle diameter

from a rather limited number of particles was not affected by methane concentration. Thus, the rather small variation (4 nm) in the simulation can be considered to be consistent with the experimental results.

The experimental results indicate that the average particle diameter decreased with a decrease in reaction temperature. To determine the best set of nucleation rate and growth rate constants at different reaction temperatures, the same approach of adjusting these values to obtain the average particle diameter close to the experimental results was applied. At each temperature, a set of constants was obtained to determine the temperature dependence of the nucleation and growth phenomena. The optimum values of nucleation rate and growth rate constants that matched the experimental data at 1573 and 1473 K were 1×10^{-1} m^3 $kmol^{-1}$ s^{-1} and 240 m^4 $kmol^{-1}$ s^{-1}, and 1×10^{-1} $m^3\cdot kmol^{-1}\cdot s^{-1}$ and 132 m^4 $kmol^{-1}$ s^{-1}, respectively.

These results indicate that the nucleation rate constant did not change with the variation of the reaction temperature. Ryu and coworkers (2007) defined the reaction temperature as the maximum temperature reached inside the reactor by external heating with a furnace as illustrated in Figure 3.1. Considering the fact that significant WC formation occurs above 1273 K (Hojo et al., 1978) and the overall chemical reaction [Equation (3-1)] is very fast, the nucleation rate constant was not affected by reaction temperature since the nucleation takes place rapidly once the gaseous reactants reached the temperature of 1273 K in this work. Experimental results (Ryu et al., 2007) showing the complete consumption of WCl_6 even at a low temperature of 1473 K supports our simulation approach. In addition, the products experimentally obtained in the range of the reaction temperature from 1473 to 1673 K were mostly WC. On the other hand, the

growth rate constant decreased with a decrease in the reaction temperature from 1673 to 1473 K. This indicates that the particle diameter was mainly affected by the dependence of the growth rate on the reaction temperature.

The temperature dependence of the growth rate constant is expressed by the following Arrhenius equation:

$$k_g = 1.412 \times 10^5 \exp\left(-\frac{10202}{T}\right) \tag{3-19}$$

which gives an apparent activation energy value of 84.8 kJ mol^{-1}, as shown in Figure 3.11. This result must be considered approximate because experimental data were obtained only at three reaction temperatures.

3.7 Comparison between the Simulation Results of SiO_2 and WC Nanoparticles

The direct determination of the actual kinetics of nucleation and growth of nanoparticles synthesized in the gas phase is a very complicated task. It may include the measurement of the gas-phase concentration of products and precursors inside the reactor by means of in situ spectroscopic techniques. Most of the previous modeling work on the gas-phase synthesis of nanoparticles involves one or several parameters fitted to yield agreements with the available experimental information such as average particle diameter, which is the most common and important parameter to be determined experimentally. In this laboratory, the simulation of the synthesis of SiO_2 nanoparticles in a flame reactor was also carried out. Simplified expression for the rate of nucleation and growth were proposed and two rate constants were adjusted as described in this article (Ji et al., 2007).

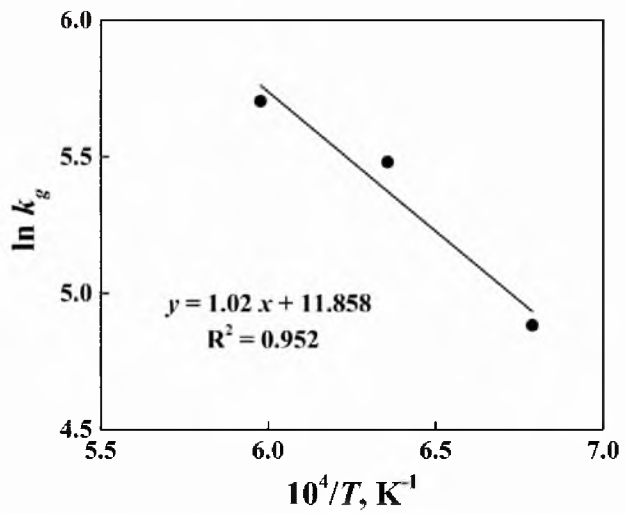

Figure 3.11: Arrhenius plot of the growth rate constant (k_g).
Values in $m^4\ kmol^{-1}\ s^{-1}$.

Although this fitting approach is empirical and the operating conditions (i.e., reaction temperature, residence time, etc.) of the synthesis processes of SiO_2 and WC nanoparticles are different, it is of interest to compare the predicted rates of nucleation and growth of particles in both processes. As a result, an order of magnitude comparison between both rate processes was performed. Since the average particle diameter was the target variable that was adjusted by fitting the rate constants, the comparison between the predicted average particle diameters in both synthesis processes will be meaningful. The average particle sizes were 15.6 and 21.7 nm for SiO_2 and WC nanoparticles, respectively. The magnitudes of the nucleation and growth rates of nanoparticles in both processes were in the order of 10^{18} # $m^{-3}\ s^{-1}$ and 10^{-7} m s^{-1}, respectively. This result correlates well with the fact that both materials, SiO_2 and WC, have high melting points.

This finding indicates that the proposed fitting approach is a reasonable representation of the actual phenomena taking place in both synthesis processes.

3.8 Concluding Remarks

The chemical vapor synthesis (CVS) of WC nanopowder from tungsten hexachloride in a tubular reactor was simulated by a two-dimensional multiphase computational fluid dynamic (CFD) model. A parametric study was conducted to determine the nucleation and growth rate constants. Experimental results obtained for the synthesis of WC nanopowder from WCl_6 with H_2 and CH_4 in a tubular reactor system were used to validate the model. The combination of nucleation rate and growth rate constants that yielded the best agreement with experimental data was determined.

The simulation will be improved further when more experimental results and more accurate nucleation and growth model are available. However, it should be noted that this work is the first application of CFD to the chemical vapor synthesis of WC nanopowder. The simulation results have been matched with the experimental data under the conditions tested. The model tested in this work will also predict experimental results for other sets of experimental conditions. This simulation tool shows significant potential for the optimization and scaling up of the chemical vapor synthesis process.

4. COMPUTATIONAL MODELING OF THE FLAME SPRAY PYROLYSIS PROCESS FOR SILICA NANOPOWDER SYNTHESIS*

4.1 Background

Silica (SiO_2) nanopowder is used as an additive in plastics and rubbers to improve the mechanical properties of elastomers, and in liquid systems to improve the suspension behavior. It is one of the most commonly produced commodities of the flame process (Pratsinis, 1998). This process provides a good control of particle size and crystalline structure and it can also continuously produce high-purity, thermally stable particles with minimal further treatments. The sizes of the flame-made particles range from a few to several hundred nanometers, depending on the operating conditions.

Silica nanopowder is typically obtained from the oxidation of silicon tetrachloride in a flame (Pratsinis, 1998). However, Jang and coworkers (Chang et al., 2008; Jang et al., 2006) have developed a flame process in which organic silicon precursors such as tetraethylorthosilicate (TEOS) and tetramethylorthosilicate (TMOS) obtained from the recycling of silicon sludge are used. This modeling work was related to the production of silica nanopowder from waste silicon sludge using a flame spray pyrolysis (PSP) synthesis reactor (Chang et al., 2008) developed at the Korea Institute of Geoscience and

*This section contains a significant part from Sohn, H. Y.; Olivas-Martinez, M.; Perez-Fontes, S. E. Mathematical Modeling of Nanopowder Production by Vapor-Phase Processes. In *Mathematical Modeling;* Brennan, C. R., Ed.; Nova Science Publishers, Inc.: Hauppauge, NY, 2011; pp 179-208; for which permission to use has been obtained from Nova Science Publishers, Inc., copyright owner.

Mineral Resources (KIGAM). Silica nanopowder was synthesized from the thermal oxidation of the volatile precursors: tetraethylorthosilicate (TEOS) and tetramethylorthosilicate (TMOS).

The final particle size and morphology of the product are determined by the flame temperature, the residence time of particles in the flame, and the aerodynamic conditions inside the reactor. Although experimental and theoretical work has been done on the flame synthesis process, the mechanisms of formation, growth and transport of nanoparticles in flames with rapid temperature changes, chemical reactions and complex fluid dynamics are still not well understood. As a result, the experimental design and scale-up of this process is a rather difficult task. Thus, mathematical models based on fundamental principles will provide a critical tool in the study and application of the FSP process.

Experimental and modeling studies on the flame synthesis of silica and other related metal oxide nanoparticles have been reported in the literature. Ulrich and coworkers (1976) conducted both experimental and theoretical work on the flame synthesis of silica particles using a flat-flame burner. The authors proposed a simple algebraic collision-coalescence model for particle growth with the sticking coefficient (defined as ratio of successful to actual collisions) as an adjustable parameter. They recognized that the morphology of silica nanoparticles produced in flames is seldom spherical. Rather, aggregates of primary particles are typically formed. Therefore, the rate of coalescence (sintering) of silica nanoparticles is finite.

Bolsaitis and coworkers (1987) studied, experimentally and theoretically, the formation of zinc oxide submicron particles in conditions similar to those found in a

diffusion flame. They proposed a simplified mathematical model incorporating mass transfer (radial mixing of zinc vapor and oxygen), chemical kinetics (generation of nuclei), and a sectional model for the nucleation and growth of particles. The authors introduced the concept of collision-controlled nucleation for metal oxide particles, which occurs when the vapor pressure of the nucleating species is very low. Under such conditions, the nucleation process is indistinguishable from the chemical reactions that produce the condensable products. These authors also recognized that the flame aerodynamic conditions (i.e., gas velocities, degree of turbulence and mixing) play a key role in the kinetics of particle formation and growth.

Johannessen and coworkers (2000) simulated the synthesis of alumina particles by the combustion of aluminum tri-sec-butoxide in a diffusion flame using a commercial CFD code. The model solves the governing equations for mass, momentum and energy in a two-dimensional axisymmetric geometry. A monodisperse model incorporating the kinetics of particle coagulation and coalescence was implemented. The authors determined the growth kinetic parameters by comparing the model predictions with available experimental data.

The literature review reveals that most of the previous models do not take into consideration the combined effects of the fluid flow, heat and mass transfer, and chemical kinetics on the particle size distribution. Therefore, it is necessary to approach the modeling from the point of view of computational fluid dynamics (CFD). As a result, Sohn and coworkers (Ji et al., 2007; Olivas-Martinez et al., 2008) proposed a modeling technique that combines CFD, a multiphase model (mixture model) and a population balance model for the flame synthesis of silica nanopowders (Ji et al. 2007; Olivas-

Martinez et al., 2008). In these works, the rates of nucleation and growth were computed using greatly simplified expressions. Since no experimental data are available on these rates, the kinetic parameters for nucleation and growth were treated as adjustable parameters.

Although the model by Sohn and coworkers (Ji et al. 2007; Olivas-Martinez et al., 2008) represented reasonably well the available experimental data, it is necessary to incorporate particle nucleation and growth models based on theory to make the model more realistic and to reduce the need of adjustable parameters.

In this work, the model formulated in Section 2 was used to simulate the synthesis of silica nanopowder from tetraethylorthosilicate (TEOS) in a bench-scale FSP reactor. The transport and evaporation of liquid droplets were simulated from a Lagrangian viewpoint. The quadrature method of moments (QMOM) was used to solve the population balance equation (PBE) for particles undergoing homogeneous nucleation and Brownian coagulation. In the next subsection, the specific approach for modeling the formation and growth of silica nanoparticles is described.

4.2 Model Formulation

Figure 4.1 shows a schematic representation of the simulated flame spray pyrolysis (FSP) reactor. It consists of an external two-fluid mixing nozzle, a burner, a flame cover and a particle collector.

The FSP process starts with the formation of a hydrogen-oxygen diffusion flame. A precursor solution containing tetraethylorthosilicate (TEOS) and ethanol is then

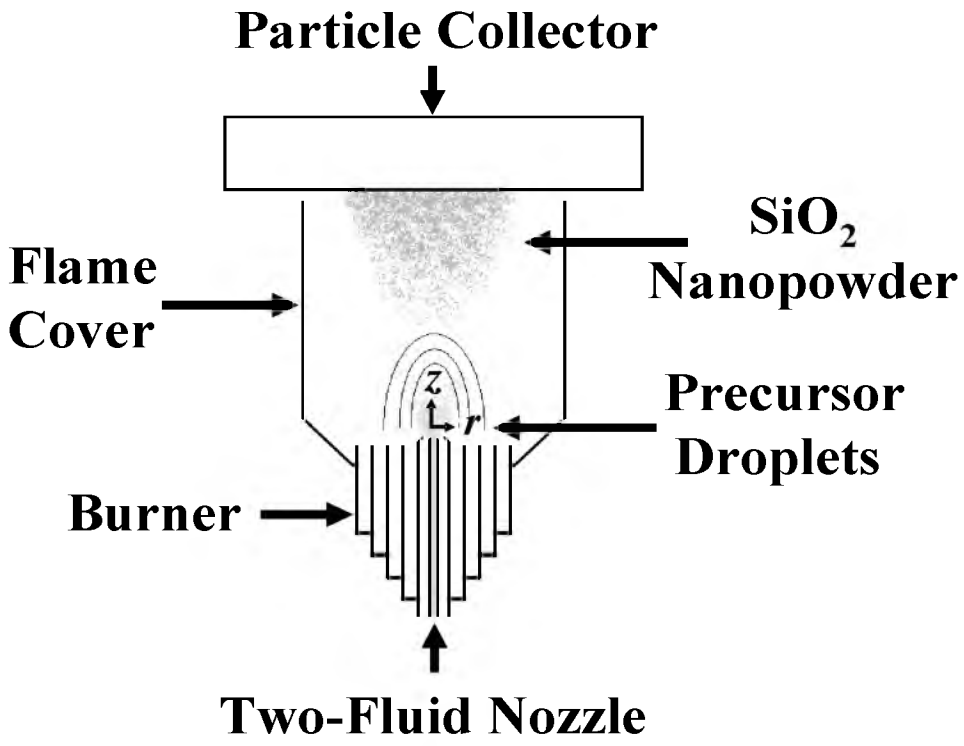

Figure 4.1: Schematic representation of the simulated FSP reactor.

sprayed into the flame through the nozzle. The spray droplets are vaporized and the resulting vapor is reacted producing condensable products that form particles.

4.2.1 Particle Nucleation

In the flame synthesis of silica particles, the Kelvin equation [Equation (2-34)] predicts that the critical nucleus size is smaller than the size of the monomer. As a result, it is widely accepted that the nucleation process is reaction-limited (Kodas and Hampden-Smith, 1999). Thus, the nucleation rate of silica particles was represented by the rate of reaction of the vapor precursors. In this work, it was considered that the vapor precursors are thermally decomposed and oxidized in the flame.

The flame synthesis of silica nanopowder by the vapor-phase thermal oxidation of tetraethylorthosilicate (TEOS) is represented by

$$Si(OC_2H_5)_4(g) \rightarrow SiO_2(s) + 4C_2H_4(g) + 2H_2O(g) \quad (4\text{-}1)$$

and

$$Si(OC_2H_5)_4(g) + 12O_2(g) \rightarrow SiO_2(s) + 8CO_2(g) + 10H_2O(g)\,. \quad (4\text{-}2)$$

Equations (4-1) and (4-2) correspond to the thermal decomposition and oxidation of TEOS, respectively. Since the nucleation rate of silica nanoparticles is represented by the rate of reaction of the vapor precursors, the nucleation rate based on the thermal decomposition of TEOS [Equation (4-1)] is then given by

$$J = k_d C_{TEOS} N \quad (4\text{-}3)$$

with the decomposition rate constant (k_d) expressed by the following equation (Chu et al., 1991):

$$k_d = 7.4 \times 10^{10} \exp\left(-\frac{49500}{RT}\right) \quad (4\text{-}4)$$

where C_{TEOS} is the molar concentration of TEOS in the vapor phase, and R = 1.987 cal mol^{-1} K^{-1}. The nucleation rate based on the oxidation of TEOS, Equation (4-2), was computed using the eddy-dissipation model (Magnussen and Hjertager, 1977) in which the rate of reaction is limited by the turbulent mixing of the reactants, considering the very rapid chemical kinetics at the high temperatures of the system.

4.2.2 Particle Coagulation

Particle growth was modeled by Brownian coagulation. In the case of silica nanoparticles, a collision efficiency factor (α_p) of unity in the collision frequency

function [Equation (2-42)] led to particle sizes ten times larger than the experimental value. This result is related to the assumption of infinitely fast coalescence rate. The morphology of silica nanoparticles produced in flames is seldom spherical. Rather, aggregates of primary particles are typically formed. Therefore, the rate of coalescence (sintering) of silica nanoparticles is finite. Various efforts (Ehrman, 1999; Lehtinen et al., 1996) have been made to develop a model to describe the sintering of silica nanoparticles. However, these models have a semi-empirical nature and then their ranges of applicability are limited to the corresponding experimental conditions (Ehrman et al., 1998). The finite sintering rate of silica nanoparticles is accounted for by setting a collision efficiency factor (α_p) smaller than unity. Its value is adjusted to match the experimentally measured average particle diameter.

4.2.3 Modeling of Spray Liquid Droplets

The modeling of the spray liquid droplets was conducted from a Lagrangian viewpoint in which the droplet trajectories are tracked from their injection points. The combustion rate of the fuel was calculated using the eddy-dissipation model (Magnussen and Hjertager, 1977). The simulation was conducted in a two-dimensional axisymmetric framework.

The Lagrangian model consists of a coupled set of ordinary differential equations (ODE's) for the velocity [Equation (2-52)], temperature [Equation (2-10)] and composition of a droplet along its trajectory with its residence time as the independent variable. The model formulation includes the following assumptions: (a) spherical droplets, (b) uniform initial droplet size, and (c) no droplet-droplet interaction.

The vaporization of a droplet is driven by the convective mass transfer from the droplet surface to the gas phase and its rate expression is given by

$$\frac{dm_{i,d}}{dt} = A_d M_i k_{c,i}\left(C_{i,s} - C_{i,b}\right) \tag{4-5}$$

The gas-phase concentration at the droplet surface ($C_{i,s}$) is calculated according to Raoult's law. The mass of the droplet (m_d) is then calculated as the sum of the masses of its constituting species by

$$m_d = \sum_i m_{i,d} \tag{4-6}$$

and the density of the droplet ρ_d is computed as the volume-averaged value of the densities of its components by

$$\rho_d = \left(\sum_i \frac{m_{i,d}}{m_d \rho_{i,d}} \right)^{-1} \tag{4-7}$$

The heat and mass transfer correlations needed to calculate the convective heat (h) and mass transfer ($k_{c,i}$) coefficients can be found elsewhere (Szekely et al., 1976).

4.3 Simulation Strategy

Figure 4.2 shows a schematic representation of the reactor geometry and inlet gas velocities used in the simulation runs. The inner/outer diameters of the four concentric tubes composing the burner were 32/35, 38/42, 45/48.5, 51.5/55 mm. The precursor solution feed rate was varied from 18.3 to 35.8 mL min^{-1}. Table 4.1 shows the experimental conditions used during the simulation runs.

Precursor solution droplets of an initial uniform size of 10 μm were injected into

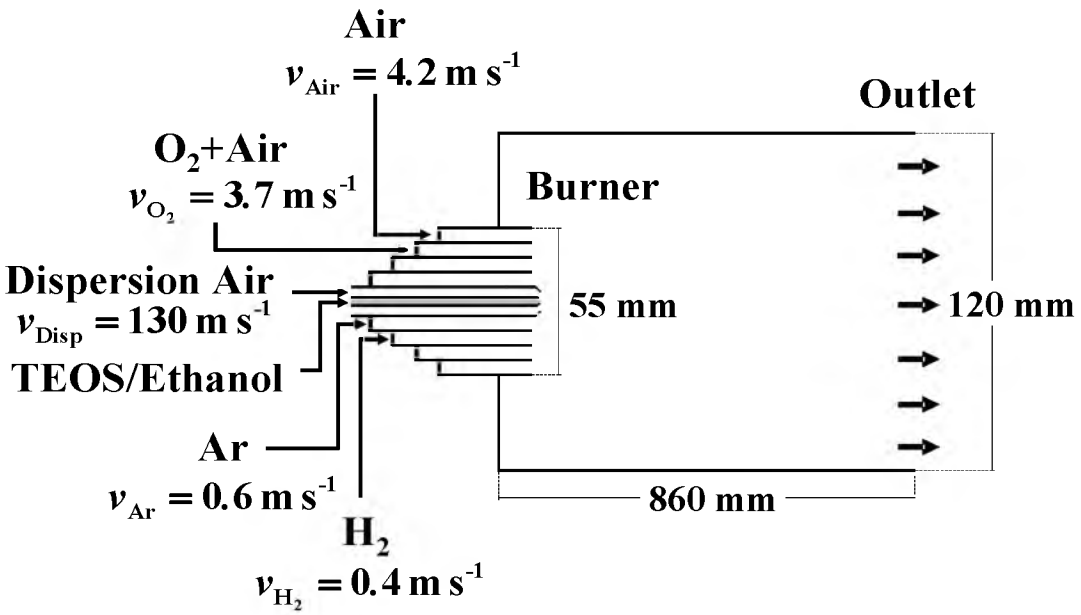

Figure 4.2: Schematic representation of the reactor geometry used in the simulation of the bench-scale FSP reactor. Inlet velocities converted from the experimental flow rates.

Table 4.1: Experimental Conditions for the Bench-Scale FSP Reactor.

Experimental Condition	Flow Rate of Dispersion Air, L min^{-1}	Feed Rate of Precursor, mL min^{-1}	Concentration of Precursor, % vol.	Particle Size, nm
Variation of the Dispersion Air Feed Rate				
JH060712_03	6	26.2	30	20.54
JH060714_03	8.3	26.2	30	13.41
JH060713_01	11	26.2	30	11.42
Variation of the Precursor Solution Feed Rate				
JH060719_02	11	18.3	50	10.57
JH060719_01	11	26.2	50	11.00
JH060802_01	11	35.8	50	14.41

the reactor at the position of the nozzle tip. Five droplet streams were defined at the injection port. Each stream supplied one-fifth of the total mass flow rate of the liquid solution. The linear velocity of the droplets was computed from the volumetric flow rate of the precursor solution and the cross-sectional area of the nozzle. The concentration of the droplets was defined according to the experimental conditions.

4.4 Distributions of Velocity, Temperature and Species Concentration

Figure 4.3 shows the contours of the velocity magnitude inside the FSP reactor. The shape of the high velocity contours resembles the jet of a high velocity spray. Figure 4.4 shows the comparison between the observed flame and computed gas temperature contours inside the FSP reactor. It is seen that the computer model reasonably reproduces the shape of the flame. More importantly, the computed maximum temperature is close to the calculated adiabatic flame temperature for a hydrogen-oxygen diffusion flame, but somewhat lower than the theoretical value as expected when the components concentrations are decreased by mixing.

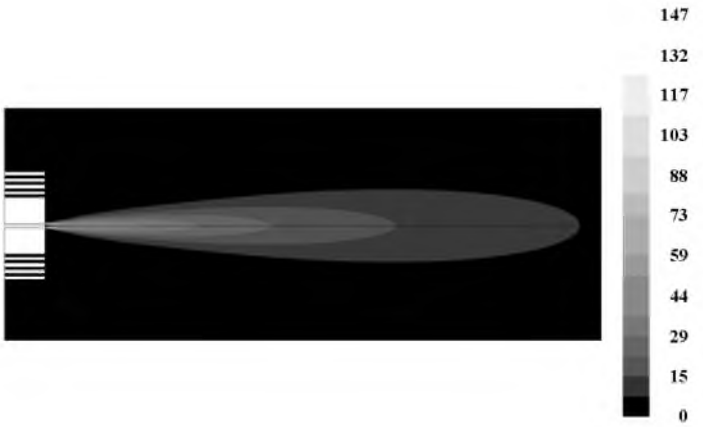

Figure 4.3: Contours of gas velocity magnitude inside the bench-scale FSP reactor. Scale values in m s^{-1}.

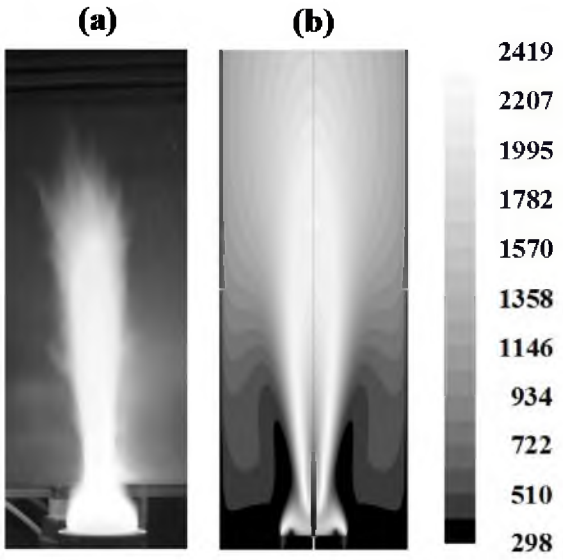

Figure 4.4: Photograph of the flame (a) and temperature contours (b) for the bench-scale flame reactor. Scale values in kelvins.

Figure 4.5 shows the effect of the dispersion air feed rate on the gas temperature. It is noted that the flame length decreases as the dispersion air feed rate increases. This means that gas-phase species mixing is enhanced and as a result, the rate of the chemical reactions is increased. Therefore, the fuel species are consumed faster at higher dispersion air feed rates, producing a shorter flame.

Figure 4.6 shows that the dispersion air variation dilutes the content of $C_2H_5OH(g)$ in the reactor and that the $C_2H_5OH(g)$ is completely combusted within a small area close to the vicinity of the burner. The latter result explains why the maximum flame temperature does not vary as the dispersion air feed rate is varied. Figure 4.7 shows that the concentration of TEOS(g) also decreases as the dispersion air increases. By comparing the concentration contours shown in Figures 4.6 and 4.7, it can be seen that the region of the highest ethanol concentration is located closer to the nozzle than that of

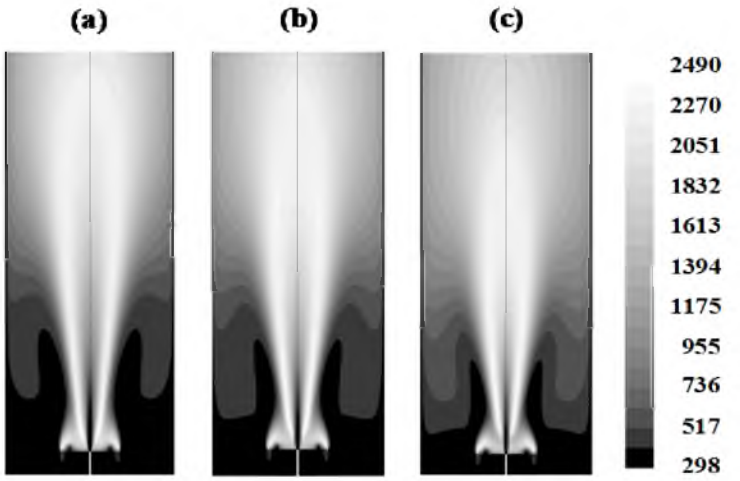

Figure 4.5: Contours of gas temperature in the entire simulated reactor geometry. Dispersion air flow rates: (a) 6, (b) 8.3, and (c) 11 L min^{-1}. Values in kelvins.

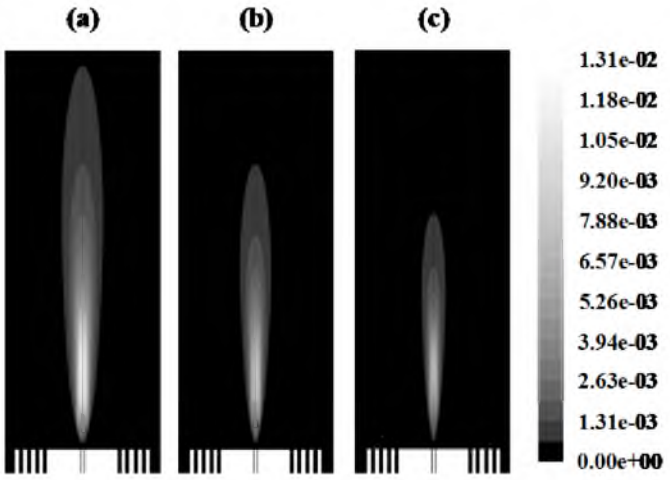

Figure 4.6: Contours of molar concentration of $C_2H_5OH(g)$ in the vicinity of the nozzle tip. Dispersion air flow rates: (a) 6, (b) 8.3, and (c) 11 L min^{-1}. Values in mol L^{-1}. The contours area shown is 0.029 x 0.15 m^2.

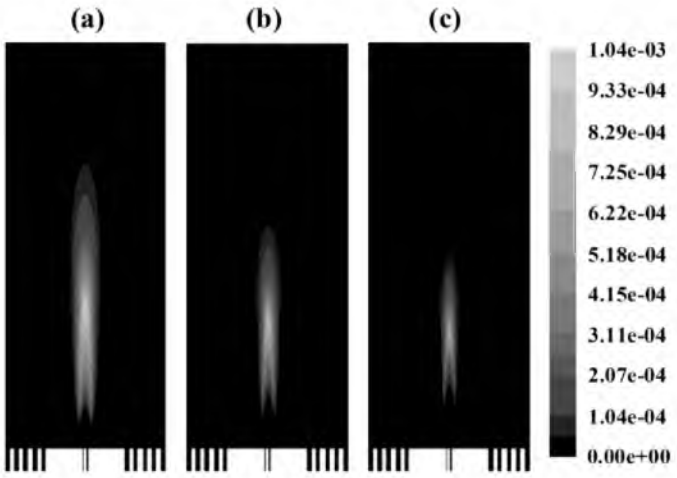

Figure 4.7: Contours of molar concentration of TEOS(g) in the vicinity of the nozzle tip. Dispersion air flow rates: (a) 6, (b) 8.3, and (c) 11 L min^{-1}. Values in mol L^{-1}. The contours area shown is 0.029 x 0.15 m^2.

the highest TEOS. This means the ethanol vaporizes faster than TEOS. This result is in agreement with the boiling points of ethanol and TEOS which are 351.6 and 442 K, respectively.

Figure 4.8 shows that the flame length is increased as the precursor feed rate increases. This is caused due to the addition of more fuel (ethanol) to the reactor. Here, the dispersion air feed rate is maintained constant, thus the increase in the rate of combustion is not related to mixing but to an increase in the fuel concentration as shown in Figure 4.6.

4.5 Particle Size Distribution

In this work, the processes of formation and growth of silica nanoparticles were represented by homogeneous nucleation (Subsection 4.2.1) and Brownian coagulation

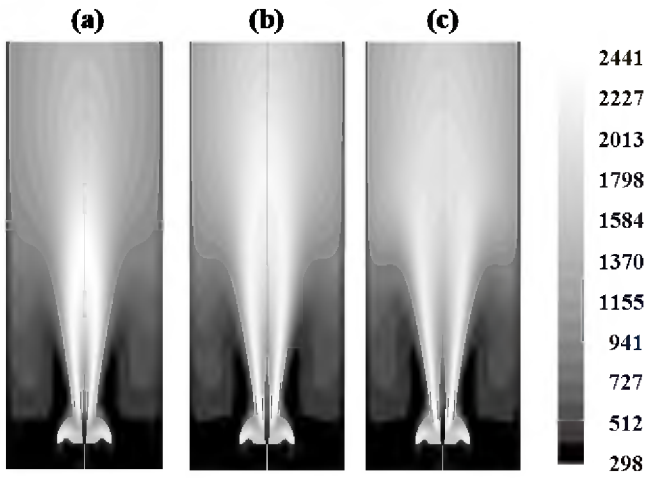

Figure 4.8: Contours of gas temperature in the entire simulated reactor geometry. Precursor solution feed rates: (a) 18.3, (b) 26.2, and (c) 35.8 mL min^{-1}. Values in kelvins.

(Subsection 4.2.2), respectively. The nucleation rate was computed with no adjustable parameters and only the collision efficiency factor α_P, which appears in Equation (2-40), was adjusted to match the experimentally measured average particle diameter. A value of $\alpha_P = 4\times10^{-4}$ was found to provide reasonable results for all experimental conditions. As discussed in Subsection 4.2.2, the value of the collision efficiency factor α_p represents the coalescence of primary particles. Such a small value can thus be expected since the coalescence rate is not only finite but also slower than the rate of particle coagulation.

The experimental average particle diameter (d_{exp}) was obtained from the measured specific surface area (S_{exp}) under the assumption of spherical shape as follows

$$d_{\text{exp}} = \frac{6}{\rho_p S_{\text{exp}}} \tag{4-8}$$

where ρ_p is the particle density. This average particle diameter is also known as Sauter diameter. The corresponding average particle diameter based on the model solution was derived as follows

$$d_{3,2} = \frac{6}{\rho_p S_a} = \frac{6}{\rho_p \frac{A_p}{\rho_p V_p}} = \frac{6V_p}{A_p} = \frac{6\frac{\pi}{6}\int_0^\infty d_p^3 n(d_p) dd_p}{\pi \int_0^\infty d_p^2 n(d_p) dd_d} = \frac{m_3}{m_2} \tag{4-9}$$

where $d_{3,2}$ is the computed local average particle diameter, S_a is the computed specific surface area of the particles, A_p is the total surface area density of the particles, V_p is the total volume density of the particles, and m_2 and m_3 are the second and third moments of the particle size distribution, respectively.

To compare the experimental and simulation results, the corresponding average particle diameter of all the particles leaving the reactor was calculated from the computed radius-dependent flow rates of the appropriate moments of the particle size distribution. The predicted Sauter diameter ($d_{3,2}$) was then obtained by

$$\bar{d}_{3,2} = \frac{M_3}{M_2} \tag{4-10}$$

where $M_k = \int m_k \vec{v}_m \cdot d\vec{A}$ is the flow rate of the *k*th moment of the particle size distribution, $\vec{v}_m$ is the mixture velocity vector, and $\vec{A}$ is the cross-sectional area vector.

The comparison between the experimental and computed average particle diameters as a function of the dispersion air feed rate is presented in Figure 4.9. Overall, the model predictions showed reasonable agreement with the experimental data. As the

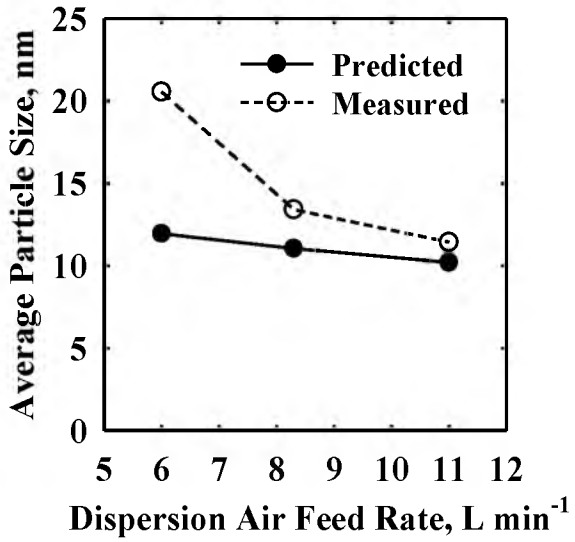

Figure 4.9: Effect of the dispersion air feed rate on the average particle diameter. Precursor liquid solution with feed rate of 26.2 mL min^{-1} and composition of 30 % TEOS by volume.

dispersion air feed rate increases, the average particle diameter decreases. The decrease in the concentration of TEOS(g) and the shortening of the flame length are likely the dominant factors. Considering the fact that the particle nucleation is controlled by gas-phase reactions of TEOS(g) and particle growth by Brownian coagulation, the decrease of the precursor concentration with increasing dispersion air flow rate will limit the maximum attainable particle diameter. In addition, the flame length plays an important role on the particle formation and growth by affecting the length of time reactants and particles remain in the reaction zone.

Figure 4.10 shows the comparison between the experimental and computed average particle diameters when the precursor feed rate was varied. The model is capable

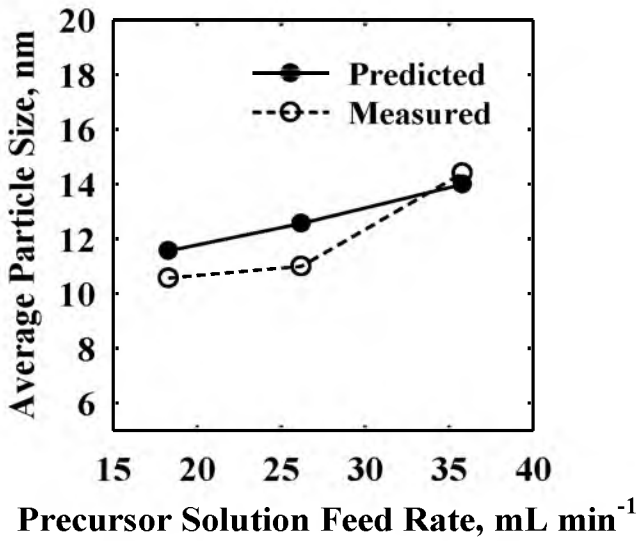

Figure 4.10: Effect of the precursor solution feed rate on the average particle diameter. Flow rate of dispersion air of 11 L min^{-1} and a precursor liquid solution with a composition of 50 % TEOS by volume.

of reproducing reasonably well the magnitude and trend observed for the average particle diameter as the precursor feed rate increases.

Figure 4.11 depicts the contours of the average particle diameter inside the reactor. It is of interest to note that the particle diameter is larger close to the center line of the reactor and smaller close to the wall. Particles nucleate in the flame and are carried by the bulk flow. This causes the particle concentration to be higher near the reactor axis than close to the walls. The coagulation rate in the center of the reactor is therefore enhanced by the high particle concentrations and high temperature. As a result, particle size is larger around the reactor axis.

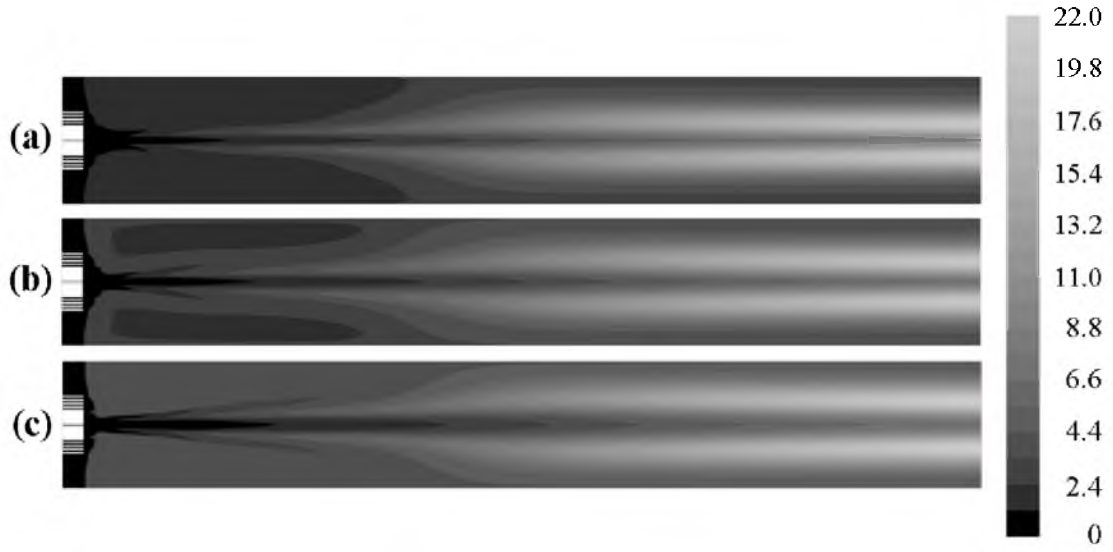

Figure 4.11: Contours of average particle diameter inside the FSP reactor. Precursor solution feed rate: (a) 18.3, (b) 26.2, and (c) 35.8 mL min^{-1}.Scale values in nm.

4.6 Concluding Remarks

In this work, a CFD model for the flame spray pyrolysis (FSP) synthesis of silica nanopowder from volatile precursors was developed. The incorporation of a Lagrangian model to represent the spray droplets provided realistic predictions of the flame temperature and the rate of vaporization of the droplets. The nucleation rate of silica nanoparticles is computed based on the rates of thermal decomposition and oxidation of the volatile precursor. Brownian coagulation was included as the particle growth mechanism.

The model was used to simulate the synthesis of silica nanopowder from tetraethylorthosilicate (TEOS) in a bench-scale FSP reactor. Computed results showed that the model is capable of reproducing the magnitude as well as the variations of the average particle diameter with different experimental conditions using a single value of

the collision efficiency factor. Overall, the model has proved to be a promising a tool for the design and scale-up of industrial-size FSP units.

5. COMPUTATIONAL MODELING OF CHEMICAL VAPOR SYNTHESIS OF ALUMINUM NANOPOWDER*

5.1 Background

Aluminum (Al) nanopowder is an important starting material for numerous aluminum-containing compounds such as AlH_3, $NaAlH_4$, $LiAlH_4$, and $Mg(AlH_4)_2$, which have been identified as having high potential as hydrogen storage materials, especially for automotive applications (Choi et al., 2010). At the University of Utah, a chemical vapor synthesis (CVS) process has been developed to produce aluminum nanopowder from the reduction of aluminum chloride ($AlCl_3$) vapor with magnesium (Mg) vapor in a wall-heated tubular reactor (Choi et al., 2010; Sohn et al., 2007). Experimental results showed average particle sizes between 20 and 100 nm.

Several researchers have worked on the modeling of synthesis processes of ultrafine aluminum particles and other materials such as silicon. Panda and Pratsinis (1995) developed a simplified plug-flow model for an aerosol flow reactor operating at nonisothermal conditions. A carrier gas saturated with aluminum vapor was flowed into a horizontal tubular reactor. As the gas mixture cooled down, particle formation and growth took place. The proposed model includes particle nucleation, condensation and coagulation. In this approach, the authors assumed a monodisperse particle size

*This section contains a significant part from Sohn, H. Y.; Olivas-Martinez, M.; Perez-Fontes, S. E. Mathematical Modeling of Nanopowder Production by Vapor-Phase Processes. In *Mathematical Modeling;* Brennan, C. R., Ed.; Nova Science Publishers, Inc.: Hauppauge, NY, 2011; pp 179-208; for which permission to use has been obtained from Nova Science Publishers, Inc., copyright owner.

distribution. Their results agreed qualitatively with the available experimental data. Schefflan and coworkers (2006) proposed a model for a lab-scale tubular reactor in which a plug of aluminum is heated with microwave energy in order to produce aluminum gas that is carried by helium. The model solves the general dynamic equation (GDE) through a sectional method with particle volume and reactor holding time as the independent variables. The authors reported on the changes in particle size distribution with the residence time as a parameter. Prakash and coworkers (2003) described a simple numerical method to solve the GDE based on a sectional approach in which the particle size distribution domain is discretized into finite-sized sections. The model involves nucleation, surface growth, and coagulation. Computed results were shown for the synthesis of aluminum particles in an aerosol flow reactor.

Setyawan and Yuwana (2008) presented an evaporation-condensation model in which the carrier gas was completely saturated with Al vapor. The authors investigated the effect of the vaporization temperature, cooling rate and pressure on the resulting particle size distribution. Computed results indicated that the particle formation and growth take place in a narrow temperature range. In this particular case, the average particle size was dominated by surface growth. Furthermore, Schwade and Roth (2003) simulated the synthesis of silicon particles from silane in a wall-heated tubular reactor using a commercial CFD code. The model solves the governing equations for mass, momentum and energy in a two-dimensional axisymmetric geometry. A population balance model incorporating nucleation and coagulation was solved by a moment method in which the particle size distribution was assumed to be lognormal.

It is important to note that most of the previous models do not take into consideration the effects of the fluid flow, heat and mass transfer, and chemical kinetics on the particle size distribution. These models are acceptable when the synthesis reactor has a simple geometrical configuration such as tubular reactor. Unfortunately, this type of systems is rarely encountered in practice. Therefore, if the synthesis reactor presents complex flow configurations then it is necessary to approach the modeling from the point of view of computational fluid dynamics (CFD).

Sohn and coworkers (Ji et al., 2007; Olivas-Martinez et al., 2008) proposed a CFD model for the vapor-phase synthesis of nanopowders. The model was used to simulate a lab flame reactor for the synthesis of silica nanopowder and a CVS reactor for the synthesis of tungsten carbide nanopowder. In these works, the rates of nucleation and growth were computed using greatly simplified expressions. Since no experimental data are available on these rates, the kinetic parameters for nucleation and growth were treated as adjustable parameters.

In this work, the model formulated in Section 2 was used to simulate the chemical vapor synthesis of aluminum nanopowder from the reduction of aluminum chloride ($AlCl_3$) vapor with magnesium (Mg) vapor in a wall-heated tubular reactor. The main objective was to make the present CFD model more realistic and to reduce the need of adjustable parameters. To achieve this, the rate of particle nucleation was computed by an expression based on the classical nucleation theory and the growth rate of particles was modeled by vapor condensation and coagulation.

5.2 Model Formulation

The mathematical modeling of the various processes involved in the chemical vapor synthesis (CVS) of aluminum nanopowder requires the coupled solution of the gas-phase transport equations; that is, fluid flow, heat and mass transfer, chemical reaction kinetics, and the particle population balance model (PBM). In this work, the modeling framework described in Section 2 was used. The model formulation includes the following two general assumptions: (a) steady state and (b) negligible effect of the particles on the aerodynamic behavior of the gas phase.

The chemical vapor synthesis (CVS) of nanopowders starts with the mixing and reaction of the vapor reactants to form condensable products. Here, aluminum chloride ($AlCl_3$) vapor is reduced by magnesium (Mg) vapor according to the following overall chemical reaction:

$$AlCl_3(g) + 3/2Mg(g) \rightarrow Al(g) + 3/2MgCl_2(g) \qquad (5\text{-}1)$$

The produced aluminum vapor is then condensed, that is, nucleation and vapor condensation, as follows

$$Al(g) \rightarrow Al(s,l) \qquad (5\text{-}2)$$

where Al(s,l) is the condensed phase that could be liquid or solid depending on the local temperature.

Because the kinetic parameters of Equation (5-1) are unknown and the reactor is operated at high temperature, it is assumed that the intrinsic reaction rate is very fast and thus the reaction rate is controlled by the turbulent mixing of the vapor reactants. This approach is often used for this type of reaction (Magnussen and Hjertager, 1977). As a

result, the rate of reaction of Equation (5-1) was calculated using the eddy-dissipation model.

The Kelvin equation [Equation (2-34)] predicts that the critical nucleus size of an aluminum particle is larger than its monomer size under this experimental condition. Therefore, the nucleation rate of aluminum particles was computed using the expression in Equation (2-36), based on the classical nucleation theory.

Particle growth was modeled by vapor condensation [Equation (2-37)] and Brownian coagulation [Equation (2-42)]. The collision efficiency factor α_p for aluminum particles was set equal to unity based on the fact that the reaction temperature is higher than the melting point of aluminum. This assumption is further supported by the experimental results (Choi et al., 2010) that yielded spherical particles.

5.3 Simulation Strategy

Figure 5.1 shows the geometry of the simulated reactor and the computational mesh. To minimize the computational time, the geometry was divided into two regions, namely, Region I and Region II, as shown in Figure 5.1(b). Then, three-dimensional meshes were made for each region. The solution using Region I, which considered only the first part of the reactor, was used to obtain profiles of the dependent variables at a plane perpendicular to the flow direction at an axial position (0.6 m from the beginning of Region I) before the end of the injection tubes. At this axial position, particles have not formed yet and thus only the gas-phase problem was solved. The obtained profiles which included temperature, velocity components, species mass fraction of Mg, $AlCl_3$, $MgCl_2$,

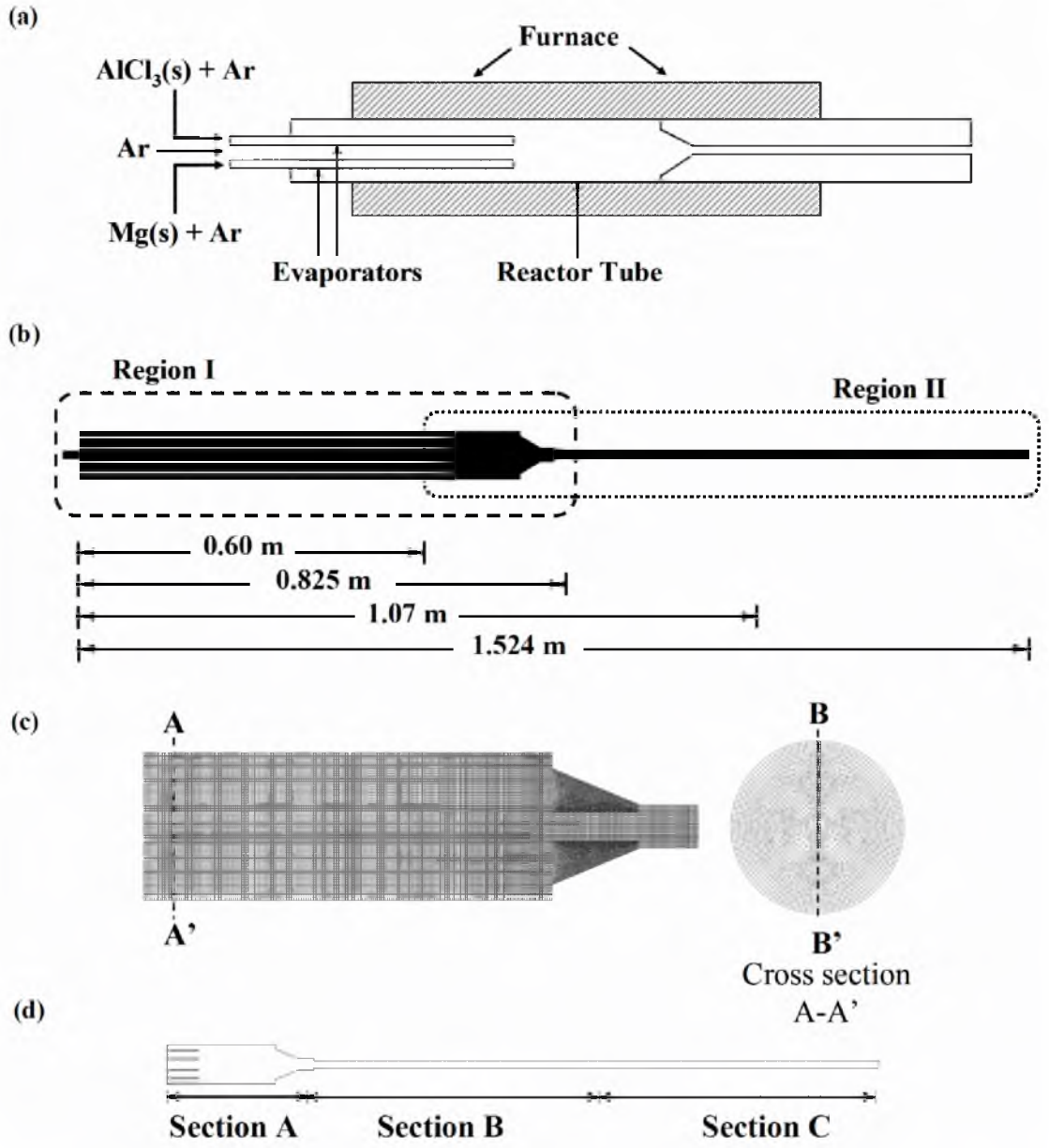

Figure 5.1: Geometry of the simulated reactor: the left side of the figure's parts represent the inlet of the reactants while the right sides represent the reactor outlet. (a) Actual reactor, (b) geometries used for the simulation, (c) magnified view of the mesh design, (d) sections for illustration of Region II.

Al and Ar, turbulence kinetic energy and turbulent dissipation rate were used as inlet boundary conditions for the simulation of Region II. With this geometry the full multiphase problem was solved.

Of particular importance for particle coagulation is the reactor zone located outside the furnace on the right-hand side of Figure 5.1(a). Simulation runs with a reduced reactor length resulted in smaller particle sizes. Table 5.1 shows the operating conditions for the simulations presented in this work. The experimental temperature profile (Figure 5.2) was used as a boundary condition at the furnace wall. The left-hand side of Region II [Figure 5.1(b)] represents the inlet where the profiles were included, while the right-hand side represents the reactor outlet. The total numbers of cells for the simulations of Regions I and II were 288,342 and 385,076, respectively. The cross-sectional view of the mesh in Section A is shown in Figure 5.1(c).

Table 5.1: Operating Conditions for the Simulations of the CVS Reactor for Aluminum Nanopowder.

	Parameter	Value
System	Environment	Argon
	Precursors	$AlCl_3$, Mg
Carrier Ar	Flow rate	1.3 L min^{-1} in $AlCl_3$ and Mg tubes
	Temperature	298 K at inlet
Dilution Ar	Flow rate	4, 6, 8 and 10 L min^{-1}
	Temperature	298 K at inlet
Total Ar flow	Flow rate	10.6 L min^{-1}
Precursor	Precursor feeding rates	$AlCl_3$: 0.1 g min^{-1} Mg: 0.03 g min^{-1}
Furnace	Wall temperature	See Figure 5.2

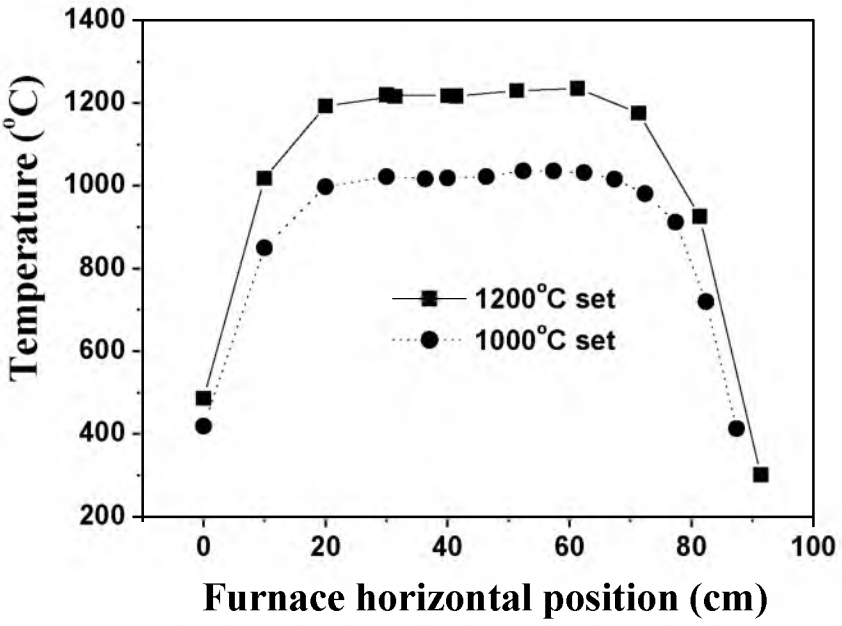

Figure 5.2: Experimental temperature profiles of the reactor wall.

5.4 Distributions of Velocity, Temperature and Species Concentration

The velocity field of the particle-laden flow has a strong effect on the characteristics of the final product. Due to the assumption of a negligible effect of the particles on the aerodynamic behavior of the gas phase, the velocity field establishes the particle residence times which determine the final particle size; shorter residence times lead to smaller particle sizes, whereas the opposite is true for larger particle sizes. Figure 5.3 shows the contours of the magnitude of the velocity field along the B-B' plane [Figure 5.1(c)]. The grey scale indicates the magnitude of the velocity field. The velocity magnitude in the zone after the funnel has the highest value, 16 m s^{-1}, due to the reduced gas passage area (Section B).

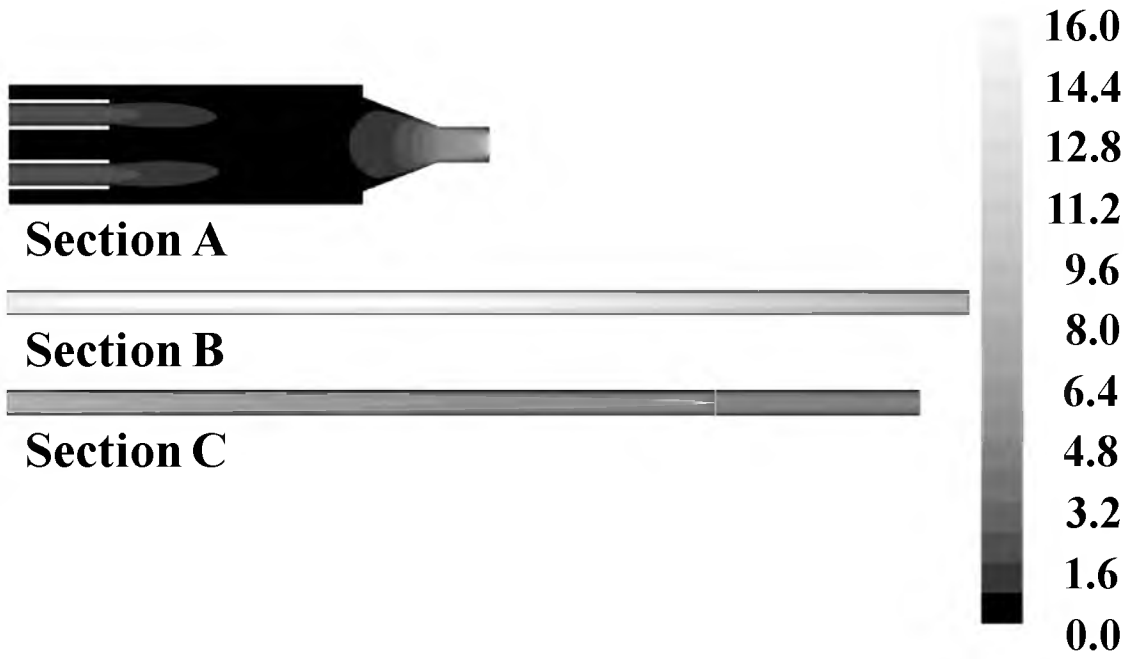

Figure 5.3: Contours of velocity magnitude along the B-B' plane in Figure 5.1 Scale values in m s^{-1}. Ar flow rate of 8 L min^{-1} (86.1 kPa and 298 K).

Figure 5.4 presents the contours of the temperature in the reactor. The reactants and carrier gas enter at room temperature (298 K). Due to the radiation heat transfer from the reactor wall, the temperature [Figure 5.4(a)] of the feeding tubes increases rapidly. The heat transfer from the feeding tubes to the carrier gas and precursor powders is then enhanced. As a result, the precursors are vaporized and the gaseous mixture is uniformly heated to the maximum reaction temperature by the end of the feeding tubes. After the funnel position [Figure 5.4(b)], the mixture temperature gradually decreased towards the end of the reactor.

Figures 5.5 through 5.8 show the mole fraction contours of the gaseous species inside the reactor. $AlCl_3$ and Mg vapors enter into the reactor through the feeding tubes. The dilution Ar stream hinders the mixing of the reactants by separating the streams of

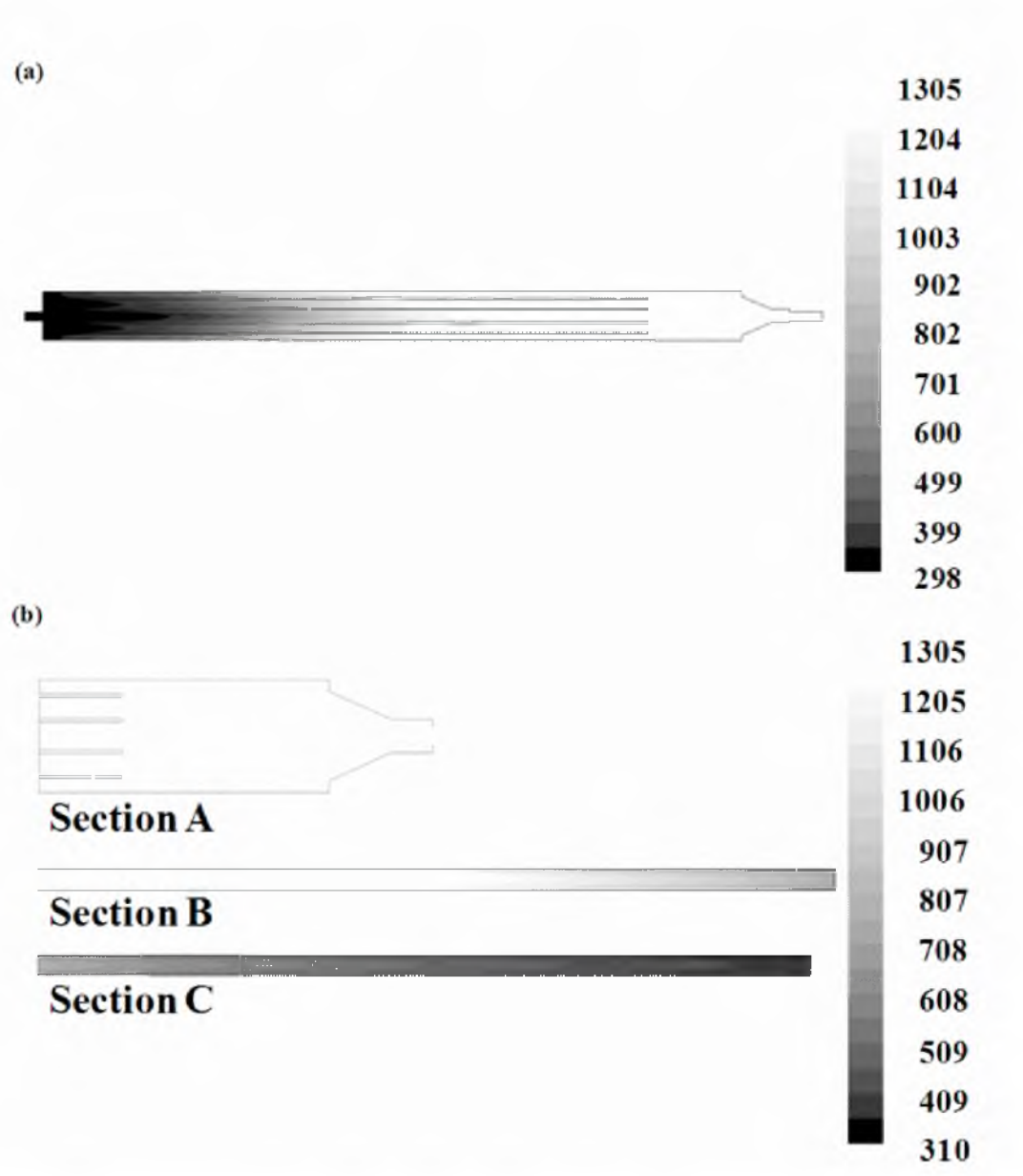

Figure 5.4: Contours of mixture temperature along the B-B' plane in Figure 5.1.Scale values in kelvins. (a) Region I and (b) Region II. Ar flow rate of 8 L min^{-1} (86.1 kPa and 298 K).

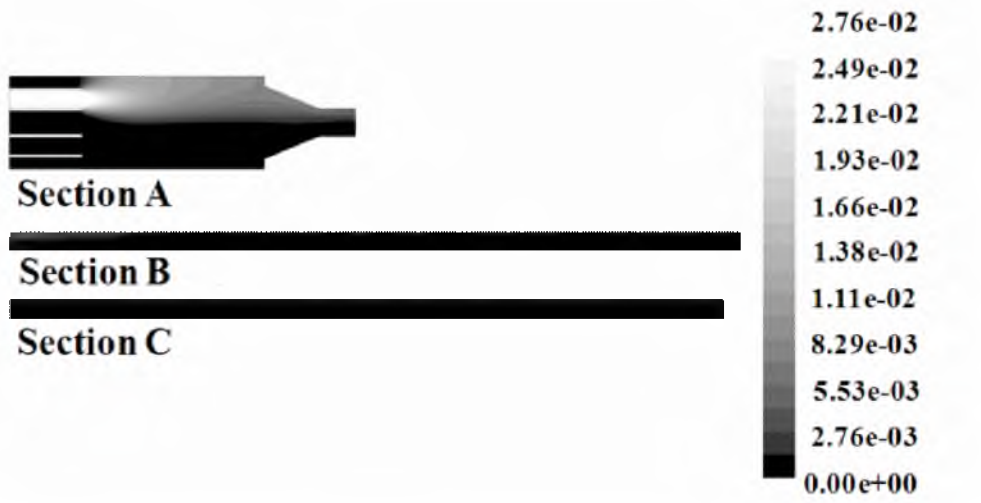

Figure 5.5: Contours of mole fraction of Mg(g) along the B-B' plane in Figure 5.1. Ar flow rate of 8 L min^{-1} (86.1 kPa and 298 K).

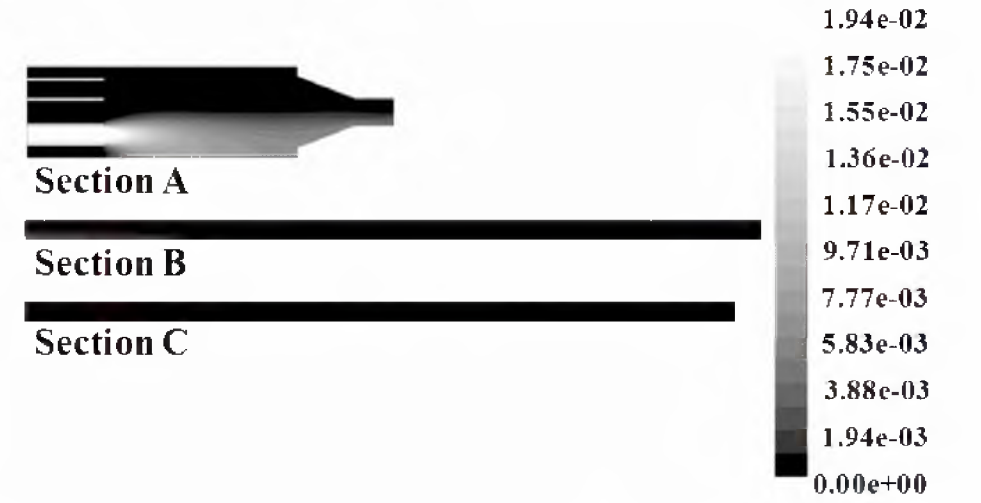

Figure 5.6: Contours of mole fraction of $AlCl_3$(g) along the B-B' plane in Figure 5.1. Ar flow rate of 8 L min^{-1} (86.1 kPa and 298 K).

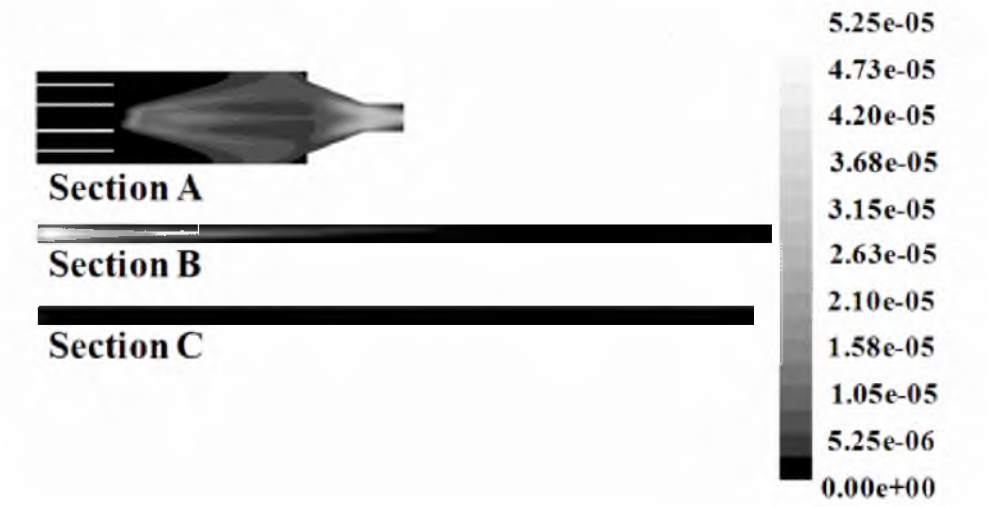

Figure 5.7: Contours of mole fraction of Al(g) along the B-B' plane in Figure 5.1. Ar flow rate of 8 L min^{-1} (86.1 kPa and 298 K).

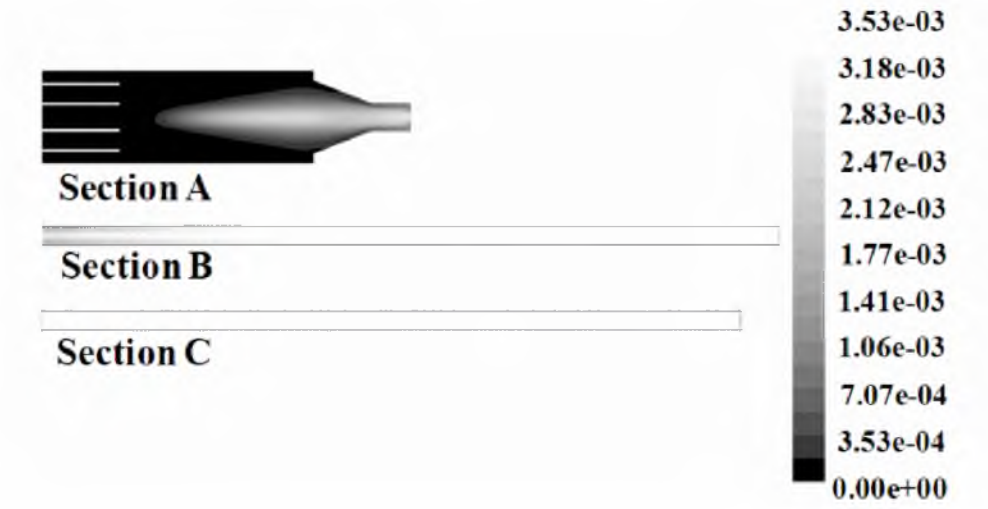

Figure 5.8: Contours of mole fraction of $MgCl_2$(g) along the B-B' plane in Figure 5.1. Ar flow rate of 8 L min^{-1} (86.1 kPa and 298 K).

$AlCl_3$(g) and Mg(g), thus preventing premature nucleation. However, the funnel reduces the area, by which the mixing path in the radial direction decreases, facilitating the gas-phase reaction. Figures 5.5 and 5.6 show that Mg(g) and $AlCl_3$(g) are fully reacted within a short distance from the end of the funnel. Figure 5.7 shows the mole fraction contours of aluminum vapor Al(g), which was completely consumed at the reactor outlet as a result of particle nucleation and vapor condensation onto the existing particles. Figure 5.8 shows the mole fraction contours of $MgCl_2$(g), which is formed where the reactant streams are mixed, and shows its maximum value after the funnel.

5.5 Particle Size Distribution

Figure 5.9 shows a comparison between the simulation results with experimental average particle size as a function of total Ar flow rate. The average particle size was calculated from the value of m_1/m_0 that describes the average particle size based on the total length of the particle diameters divided by the number of particles, that is, the number-average size. Experimentally, the particle size distribution (PSD) was determined by ZetaPALS analysis and was a number-averaged PSD. This was the reason for calculating a number-average size in the simulation.

In general, the predicted average particle size shows a reasonable agreement with the experimental data, within 10 nm error range, without the use of adjustable parameters. Thus, the model proposed in this work can be applied to other similar systems with much more confidence even without the need of any experimental data.

Figure 5.10 shows the particle number density (m_0) computed along the reactor

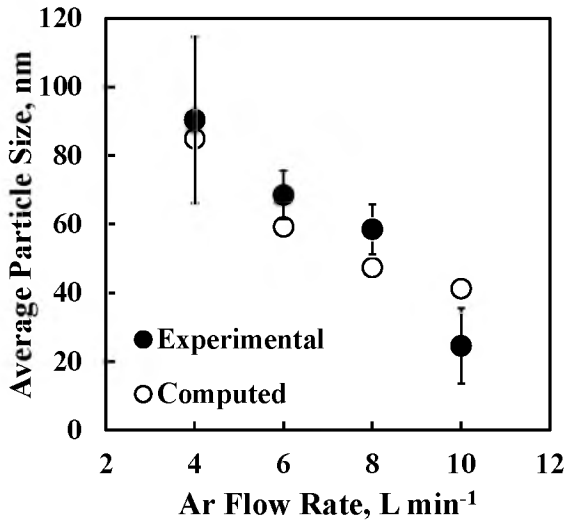

Figure 5.9: Comparison of computed and experimental average particle sizes. The vertical bars represent the experimental errors obtained from five repeated runs in each case.

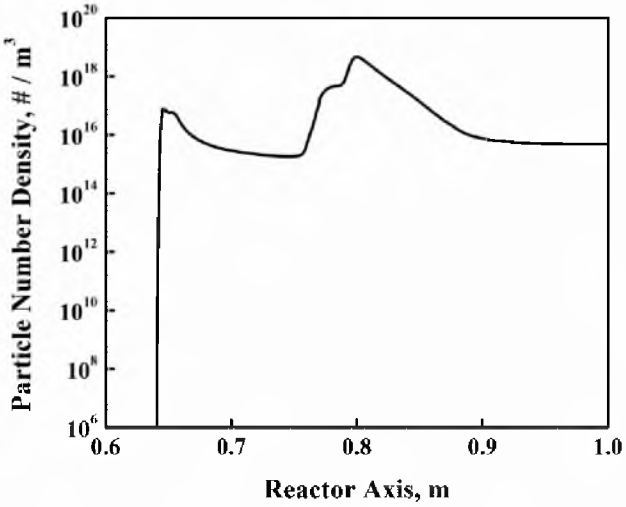

Figure 5.10: Computed particle number density (m_0) along the reactor axis. Ar flow rate of 8 L min^{-1} (86.1 kPa and 298 K).

axis in the length interval where the nucleation process takes place. It is noted that there are two main nucleation zones: (1) right after the feeding tubes (0.64 m from the beginning of Region I) where the precursors react and (2) at the starting position of the funnel in the middle of Section B (0.74 ~ 0.90 m from the beginning of Region I). This is the result of the combined effect of the degree of supersaturation on the nucleation rate and particle coagulation.

Figure 5.11 shows the contours of average particle size (APS) which is mainly affected by nucleation and growth processes. Most nucleation takes place at the entrance of the funnel. Thereafter the particles grow by condensation of aluminum vapor onto the existing particles and coagulation. Since the reaction temperature was higher than the melting point of aluminum, the coalescence rate was extremely fast and thus spherical particles were formed after coagulation. Therefore, the coagulation process determined the final particle size. Computed results without coagulation (not shown here) showed particle sizes smaller than 10 nm for all experimental conditions tested (Choi et al., 2010), which is much smaller than the experimental values. The distribution of the APS at the outlet is given in Figure 5.12. Near the wall, the average particle size is large because the velocity is lower there, which promotes particle growth. However, most of the particles at the outlet were less than 50 nm.

The geometric standard deviation, σ_{gs}, is commonly used as a measure of the degree of spread of the particle size distribution (PSD) of powders synthesized from the vapor phase, even in cases in which the PSD is not truly lognormal. This approach is justified by the fact that several types of aerosol processes are approximately represented

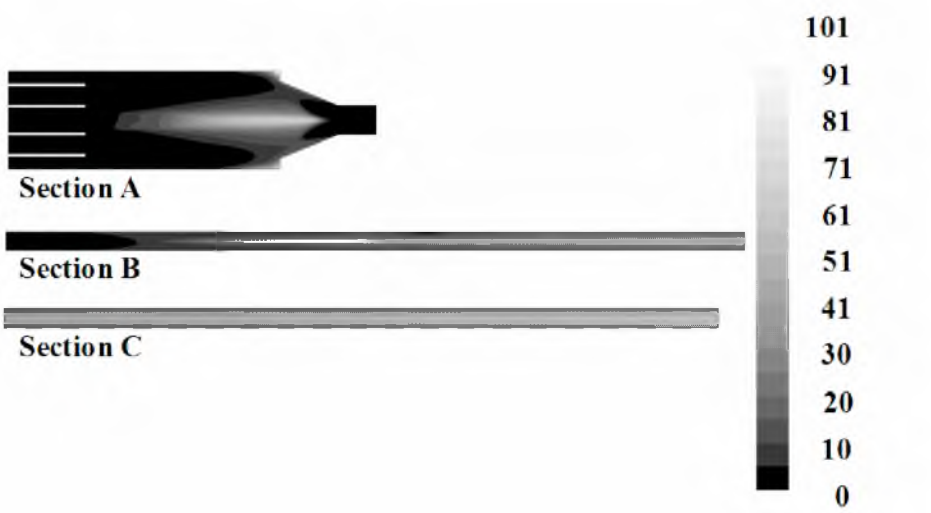

Figure 5.11: Contours of average particle size along the B-B' plane in Figure 5.1. Scale values in nm. Ar flow of rate 8 L min^{-1} (86.1 kPa and 298 K).

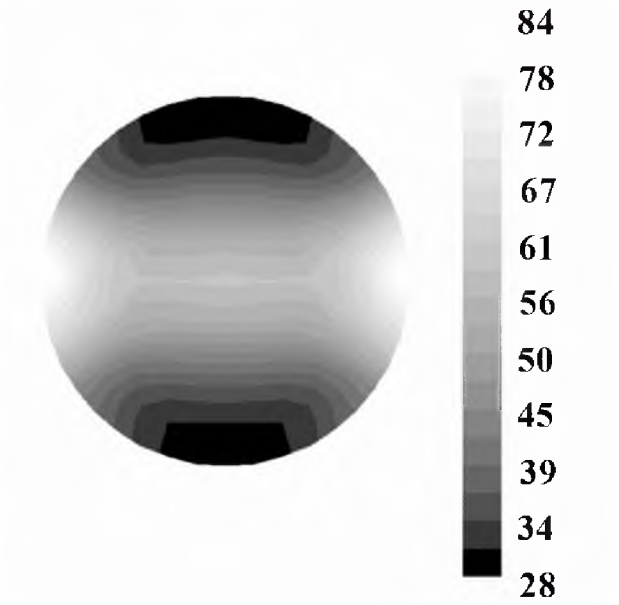

Figure 5.12: Contours of the average particle size at the reactor outlet. (A-A' plane in Figure 5.1). Scale values in nm. Ar flow rate of 8 L min^{-1} (86.1 kPa and 298 K).

by the lognormal distribution (Kodas and Hampden-Smith, 1999). The general moment expression of the size distribution function for a lognormal distribution is given by (Friedlander, 2000)

$$\ln \frac{m_i}{m_0} = i \ln d_{pg} + \frac{i^2}{2} \ln^2 \sigma_{gs} \tag{5-3}$$

where d_{pg} is the geometric mean diameter.

By defining equations for the first three moments (i = 0, 1, 2), an expression for the geometric standard deviation can be obtained as follows

$$\ln^2 \sigma_{gs} = \ln \frac{m_0 m_2}{m_1^2} \tag{5-4}$$

Figure 5.13 shows the effect of the carrier gas flow rate on the profiles of σ_{gs} along the reactor axis. It is seen that all profiles approached a single value of σ_{gs} ($\approx$ 1.44). This value indicates the narrowest particle size distribution that can be obtained at the given conditions. It also indicates that the bulk flow has no effect on the spread of the distribution provided that enough reactor length is available. An interesting piece of information that can be obtained from the axial profile of σ_{gs} is the necessary reactor length to attain the narrowest particle size distribution. Thus, reactor overdesign could be avoided.

5.6 Concluding Remarks

A three-dimensional computational fluid dynamic model incorporating fluid flow, heat and mass transfer, chemical kinetics and population balance was developed for the chemical vapor synthesis of aluminum nanopowder. The nucleation rate was computed

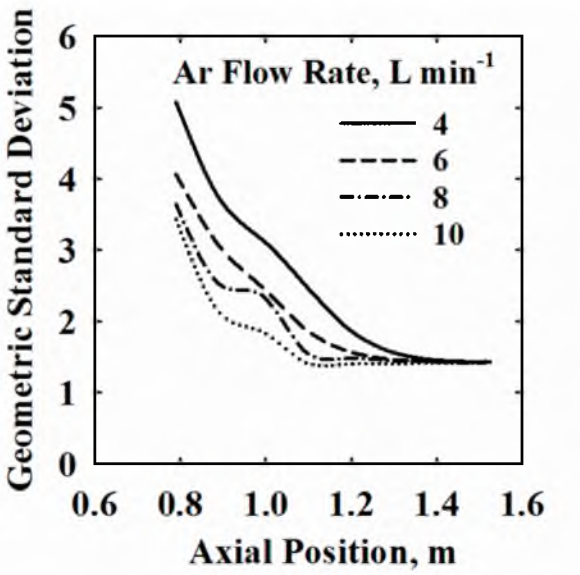

Figure 5.13: Axial profiles of the geometric standard deviation (σ_{gs}).
Flow rates at 86.1 kPa and 298 K.

using an expression from the classical nucleation theory. The growth rate was obtained by the combined effect of vapor condensation and coagulation.

The comparison of the model predictions with the available experimental data showed good agreement under different operating conditions. Computed results indicated that particle aggregation determined the final particle size in the simulated CVS reactor. The model proposed in this work can be applied to other similar systems with confidence even without the need of any experimental data, and can be used for scale-up of the process.

6. COMPUTATIONAL MODELING OF A NOVEL FLASH IRONMAKING PROCESS: GAS-PHASE VALIDATION AND THREE-DIMENSIONAL SIMULATION OF VELOCITY, TEMPERATURE AND SPECIES CONCENTRATIONS, AND OF PARTICLE TRAJECTORIES IN A LAB FLASH REACTOR

6.1 Background

The University of Utah, with support from the American Iron and Steel Institute (AISI), is developing an entirely new transformational technology for alternate ironmaking. This novel technology is based on the direct gaseous reduction of iron oxide concentrates in a flash reduction process. The ultimate objective is to significantly increase energy productivity and reduce environmental emissions, especially CO_2 emissions, in contrast to the conventional blast furnace (BF) route. The considerable energy and environmental benefits arise largely from the elimination of cokemaking and pelletization/sintering steps in the predominant ironmaking technology (BF route). The proposed novel flash ironmaking process uses gaseous reducing agents, such as natural gas, hydrogen, other syngas, or a combination thereof.

The fundamental question regarding the feasibility of adapting the flash furnace to ironmaking concerned the speed of reaction; that is, could iron oxide concentrates be completely reduced in the few seconds of residence time typically available in a flash furnace? Previous experimental results (Choi and Sohn, 2010) using iron oxide

concentrates (~30 μm size) showed that 90–99% reduction can be achieved within 2–7 seconds of residence time at temperatures 1473 K or higher. This was verified by larger laboratory-scale testing. Thus, the question on whether the reduction rate of concentrate particles is fast enough for a flash reduction process has been resolved conclusively to be affirmative.

In this process, iron oxide concentrate particles are injected directly into a refractory-lined reaction chamber, and they are reduced in flight by hot reducing gases produced by the partial combustion of natural gas, hydrogen or syngas. The reducing gas is introduced through oxy/fuel burners on top of the vessel. The concentrate powder can be fed through the burners and/or various auxiliary ports located on the vessel roof. After reduction, the reduced concentrate particles fall to the bottom of the vessel. The vessel's operating temperature ranges from 1473 to 1873 K.

The reduction degree of the iron oxide concentrate particles is determined by the reaction temperature, residence time of the particles in the reaction zone, gas composition, and aerodynamic condition inside the reactor. These operating conditions originate from complex interactions between various physical and chemical processes occurring inside the reactor; namely, fluid flow, heat and mass transfer, gas-phase reactions, and the reaction of solid particles with a hot gaseous stream. Therefore, the understanding of these rate processes plays a critical role in the development and operation of this process.

The study and analysis of chemically reacting particle-laden flows solely by traditional experimental methods is difficult because these methods do not provide information on the local gradients of velocity, temperature, and species concentrations,

which the reacting particles experience inside the reactor. Consequently, the experimental design and scale-up of these processes is a rather difficult task. Mathematical models based on fundamental principles will thus provide a critical tool in the study and application of such processes.

The overall objective was to develop a three-dimensional mathematical model based on computational fluid dynamics (CFD) capable of describing the various processes occurring in this novel flash ironmaking process. This CFD model will thus be instrumental for major technology development tasks such as burner and powder injector design, experiment planning and analysis of lab and bench flash reactor operations, and eventual design of pilot and industrial plants.

In this work, the model formulation described in Section 2 was applied to the novel flash ironmaking process operated using hydrogen as a fuel/reductant. Particular model features include the use of a simplified chemical reaction mechanism for the partial combustion of hydrogen with oxygen and the tracking of iron oxide concentrate particles in a Lagrangian framework. Computed results of the simulation of benchmark experiments reported in the literature for a nonpremixed hydrogen jet flame are then presented for model validation. The design of a nonpremixed H_2-O_2 burner is discussed. The distributions of velocity, temperature, and species concentrations, and the concentrate particle trajectories in a lab flash reactor were computed and analyzed.

6.2 Model Formulation

6.2.1 Combustion Modeling

In the flash ironmaking reactor, the required process heat (i.e., endothermic reduction heat, sensible heat of products, and reactor heat loss) will be generated internally by the partial combustion of a fuel (e.g., hydrogen or natural gas) with oxygen. This subsection describes the modeling approach used in this work to compute the combustion rate of a H_2-O_2 mixture.

In processes in which complete combustion occurs and the mixing of the fuel and oxidant takes place outside the burner (i.e., nonpremixed burner), it is customary to assume that the intrinsic gas-phase reaction rate is very fast and thus the reaction rate is controlled only by the turbulent mixing of the reactants. The combustion rate can therefore be calculated using the eddy-dissipation model (EDM) (Magnussen and Hjertager, 1977).

In initial modeling efforts, the partial combustion of hydrogen with oxygen was modeled by the EDM. Computed results showed flame temperatures much higher than the adiabatic flame temperature; that is, the model significantly overpredicted the combustion rate. The heat evolution in H_2-O_2 flames may be dominated by the reactions of intermediate species such as H and OH radicals and, consequently, the simple mixed-and-burnt approach (EDM) is not appropriate. A more realistic approach considering the reaction rates of these intermediate species was then required.

In this work, a simplified reaction mechanism for H_2-O_2 composed of seven elementary reactions representing the combustion process was adopted along with the eddy dissipation concept (EDC) approach (ANSYS, 2011; Magnussen, 1981) to represent

the turbulence chemistry interaction. In the EDC approach, finite reaction rates are computed in control (differential) volumes which behave as small constant-pressure reactors; the dimensions of which are defined by the length of the small scales of turbulence.

The gas-phase reaction mechanism (Table 6.1) adopted in this work was proposed by Eklund and coworkers (1990). It consists of seven chemical reactions involving six species: H_2, O_2, H_2O, OH, H, and O. The chemical reactions were represented by the general form:

$$aA(g) + bB(g) = cC(g) + dD(g) \tag{6-1}$$

for which the molar reaction rate was defined by

$$R_j = k_{f,j} C_A^a C_B^b - k_{r,j} C_C^c C_D^d \tag{6-2}$$

The forward and reverse rate constants in Equation (6-2) were computed from

$$k_{f,j} = A_j T^{\beta_j} \exp\left(\frac{-E_{a,j}}{RT}\right) \tag{6-3}$$

$$k_{r,j} = \frac{k_{f,j}}{K_{c,j}} \tag{6-4}$$

Table 6.1: Gas-Phase Reaction Mechanism for H_2-O_2 Combustion.

	Reaction	A ($cm^3\ mol^{-1}\ s^{-1}$)	β (Dimensionless)	E_a ($cal\ mol^{-1}$)
1	$H_2 + O_2 = OH + OH$	0.170×10^{14}	0.0	48151
2	$H + O_2 = OH + O$	0.142×10^{15}	0.0	16401
3	$OH + H_2 = H_2O + H$	0.316×10^{08}	1.8	3030
4	$O + H_2 = OH + H$	0.207×10^{15}	0.0	13750
5	$OH + OH = H_2O + O$	0.550×10^{14}	0.0	7000
6	$H + OH = H_2O + M$	0.221×10^{23}	-2.0	0
7	$H + H = H_2 + M$	0.653×10^{18}	-1.0	0

6.2.2 Particle-Phase Equations

The modeling of the iron oxide concentrate particles was carried out from a Lagrangian viewpoint in which the particle trajectories are tracked from its injection point in the flow field. The model consists of a coupled set of ordinary differential equations (ODEs) for the particle velocity and temperature along its trajectory with its residence time as the independent variable. In addition, the exchange of momentum, energy and mass between the particle and the gas phase is computed. The resulting source terms are then added to the gas-phase equations. The model formulation includes the following assumptions: (a) spherical particles and (b) no particle-particle interaction.

The equation of motion for the concentrate particles in a Lagrangian framework is given by

$$\frac{d\vec{v}}{dt} = \frac{3}{4} C_D \frac{\rho_g}{\rho_p} \frac{1}{d_p} |\vec{u} - \vec{v}|(\vec{u} - \vec{v}) + \frac{(\rho_p - \rho_g)}{\rho_p} \vec{g} \tag{6-5}$$

where $\vec{u}$ is the gas velocity vector, $\vec{v}$ is the particle velocity vector, ρ_g is the gas density, ρ_p is the particle density, d_p is the particle diameter, C_D is the drag coefficient and $\vec{g}$ is the gravity vector. Equation (6-5) states that the rate of change of particle momentum is equal to the forces acting upon it. The first and second terms on the right-hand side represent the aerodynamic drag force and the gravitational acceleration, respectively.

The cloud model (ANSYS, 2011) was used to describe the dispersion of particles. In this model, the mean trajectory [Equation (6-5)] and concentration of a particle cloud consisting of identical particles with the same initial conditions are computed. Within a cloud, all particles behave identically. All the particle equations are thus formulated for a single particle following the mean trajectory of the cloud to which it belongs.

The equation of energy for a particle moving along its trajectory is

$$m_p c_p \frac{dT_p}{dt} = h_s A_p \left(T_g - T_p\right) + Q_{rp} + H_r \tag{6-6}$$

where T_p is the particle temperature. Equation (6-6) states that the rate of change of the particle temperature is due to the heat transfer by convection (first term on the RHS), the net radiation received by the particles (second term on the RHS), and the net rate of heat production (third term on the RHS) by the reactions involving the particles. Equation 6-6 assumes that there is negligible internal resistance to heat transfer, which means that a particle is at uniform temperature throughout. The heat transfer correlation needed to calculate the convective heat transfer coefficient (h_s) can be found in the literature (Szekely et al., 1976). The details of the radiation heat transfer are described in Section 2.

6.3 Gas-Phase Model Validation

The flash ironmaking process will depend on one or more oxy/fuel burners as the main heat source. One of the key features of a computer model of this process is an appropriate description of the combustion aerodynamics of the burner(s). With the purpose of validating the gas-phase mathematical treatment, benchmark experiments reported in the literature for a nonpremixed hydrogen jet flame (Barlow, 2003; Barlow and Carter, 1994, 1996) were simulated in this work. The model predictions were compared with experimental data in terms of temperature and concentration of major species.

Barlow (2003) simultaneously measured the gas temperature, mass fractions of major species (O_2, N_2, H_2, H_2O), and mass fraction of OH and NO in a turbulent

nonpremixed hydrogen jet flame at various axial and radial positions. These multiscalar measurements were obtained by combining spontaneous Raman scattering, Rayleigh scattering, and laser-induced fluorescence. Further information on the experimental setup and details of the data can be found elsewhere (Barlow, 2003; Barlow and Carter, 1994, 1996).

In this work, the model predictions of gas temperature and mass fractions of H_2, O_2, H_2O, and OH were compared with Favre averaged measurements. Table 6.2 presents the model parameters used in the simulations. Figure 6.1 shows a schematic representation of the geometry of the experimental hydrogen jet flame, which was simulated in this work for validation of CFD model. It also shows the computational domain used in the simulation. Due to the axial symmetry of the experimental setup, one-half of the physical domain was sufficient for simulation. Along the symmetry axis and the far-field boundary in the radial direction, the gradient of all dependent variables was set equal to zero, whereas the remaining boundary conditions were specified according to Table 6.2.

Figure 6.2 shows predicted and experimental radial gas temperature profiles at various axial positions. In spite of the complex interaction of turbulence, gas-phase chemistry and aerodynamics, the computer model yields a satisfactory prediction of the flame temperature.

Figures 6.3–6.6 show the comparison between experimental and computed radial mass fraction for the following gas-phase species: H_2, O_2, H_2O, and OH. Overall, the computer model showed good agreement with the trends observed in the experimental

Table 6.2: Boundary Conditions for the Simulation of the Nonpremixed Hydrogen Jet Flame. Data Source: Barlow (2003).

Parameter	Value
Geometry, mm	
H_2 inlet radius, R_{fuel}	1.875
Visible flame length, L	675
Hydrogen Jet	
Velocity components, m s^{-1}	
Axial	296
Radial	0
Turbulent model parameters	
Intensity, %	5
Hydraulic diameter, m	0.00375
Temperature, K	295
Mass Fraction, kg kg^{-1}	1.0
Air Coflow	
Velocity components, m s^{-1}	
Axial	1.0
Radial	0.0
Turbulent model parameters	
Intensity, %	5
Hydraulic diameter, m	0.295
Outlet	
Turbulent model parameters	
Intensity, %	5
Hydraulic diameter, m	0.3

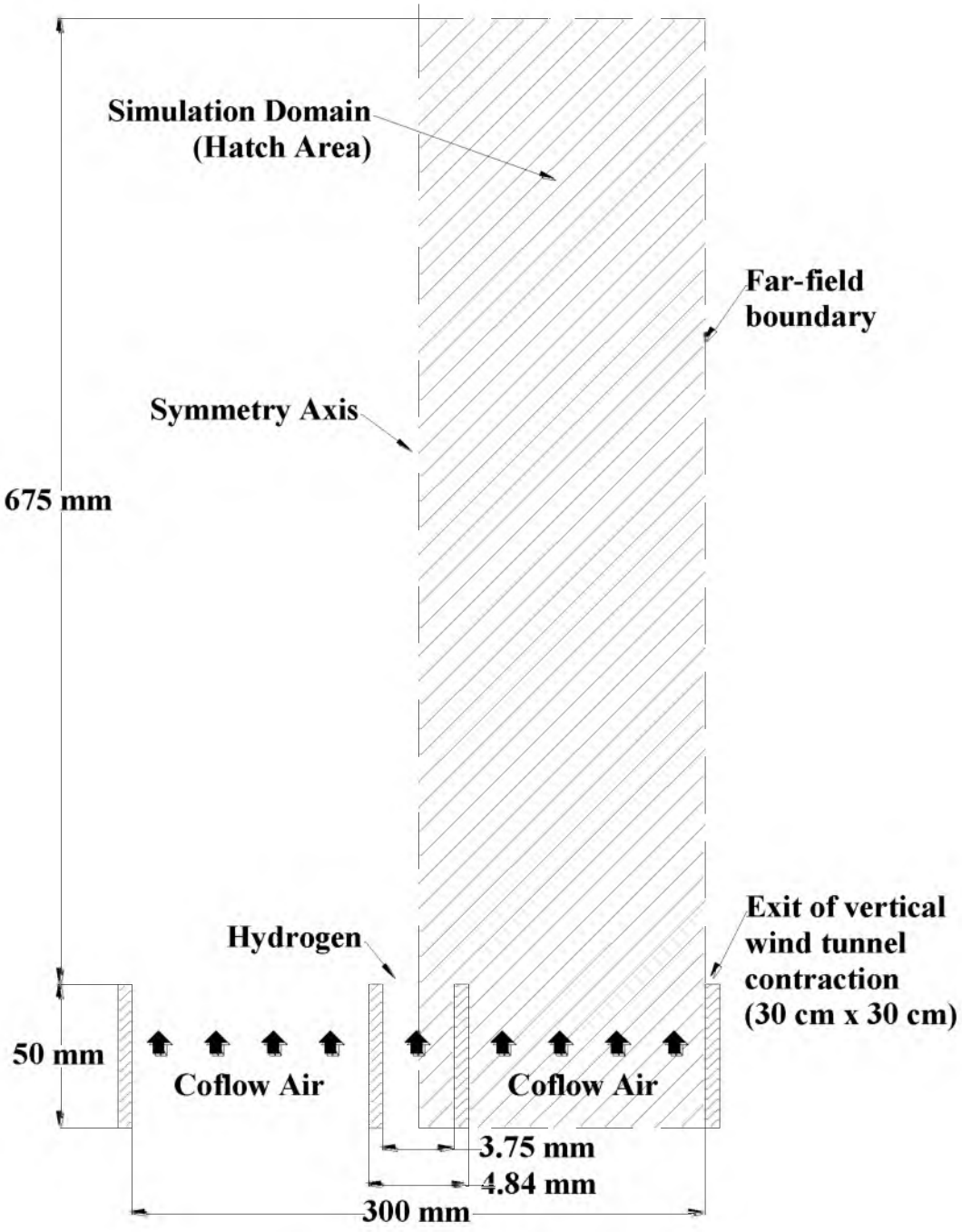

Figure 6.1: Schematic representation of the geometry of the experimental hydrogen jet flame (Barlow, 2003), which was simulated in this work for validation of the CFD model.

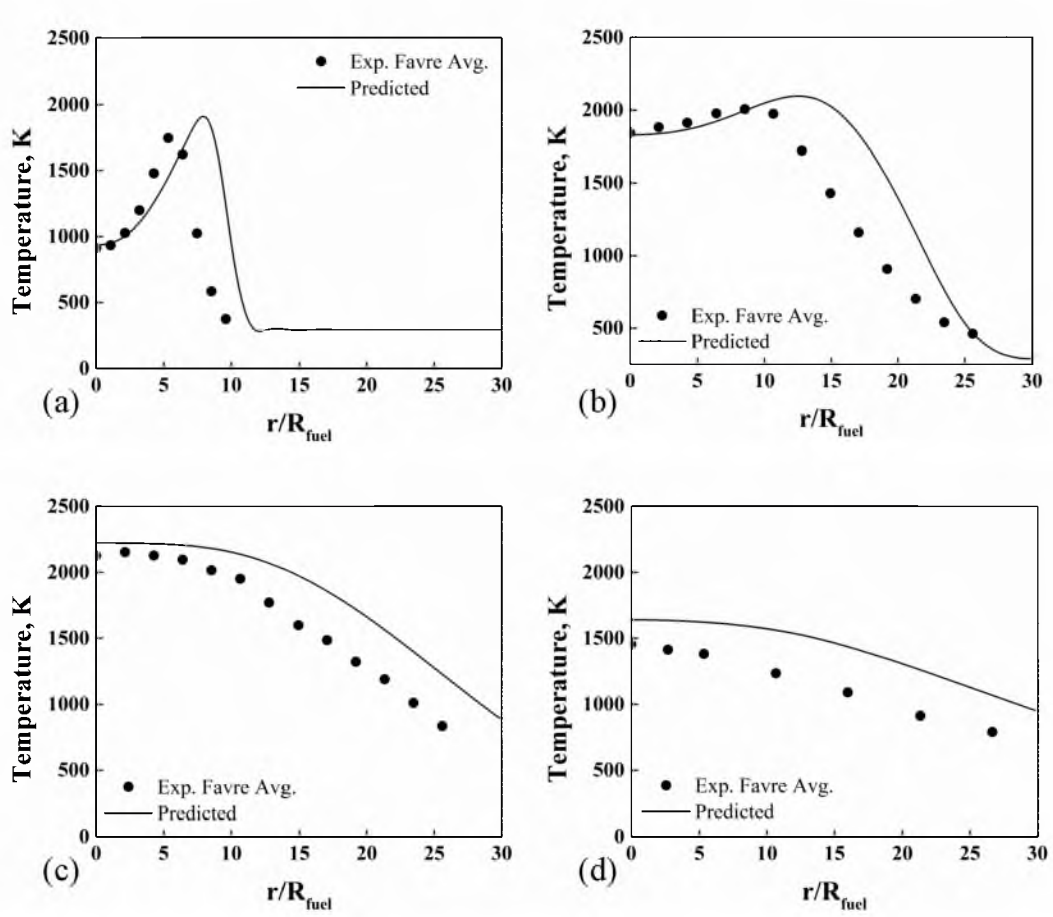

Figure 6.2: Radial gas temperature profiles at various axial positions.
z/L = (a) 1/8, (b) 3/8, (c) 5/8, and (d) 1.

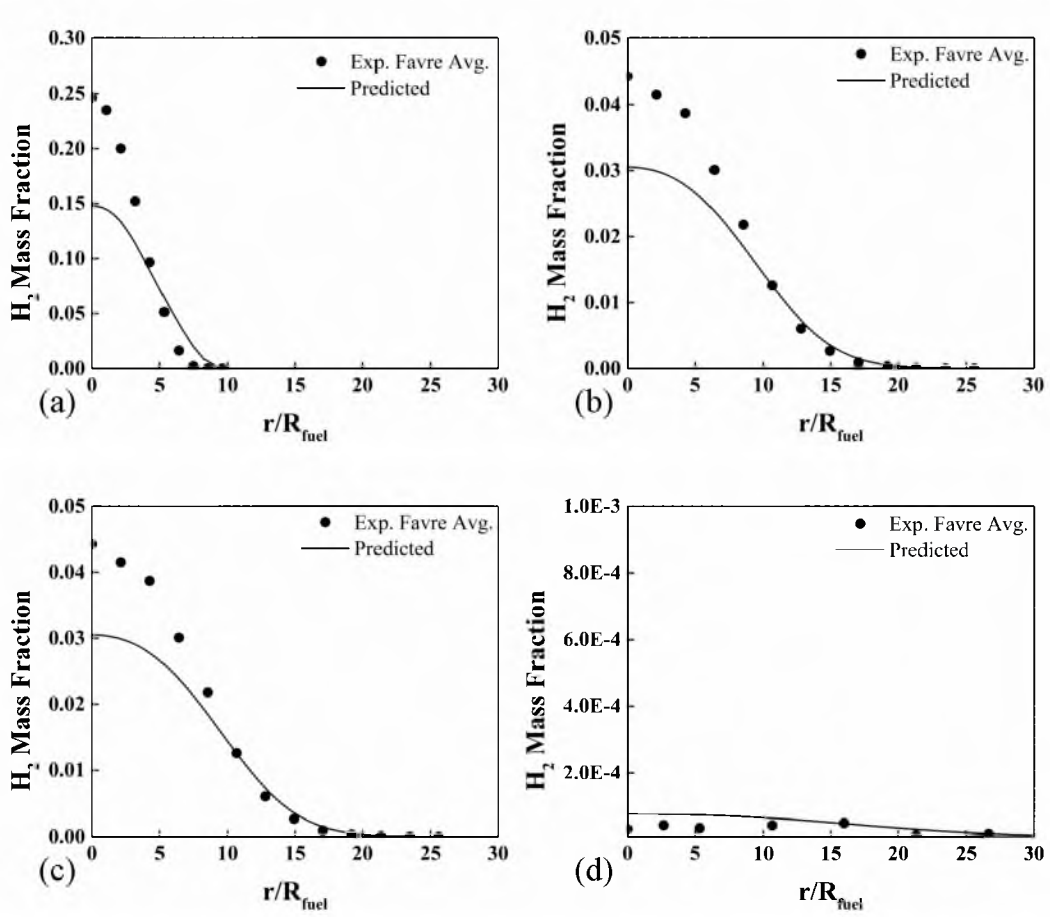

Figure 6.3: Radial H_2 mass fraction profiles at various axial positions. z/L = (a) 1/8, (b) 3/8, (c) 5/8, and (d) 1.

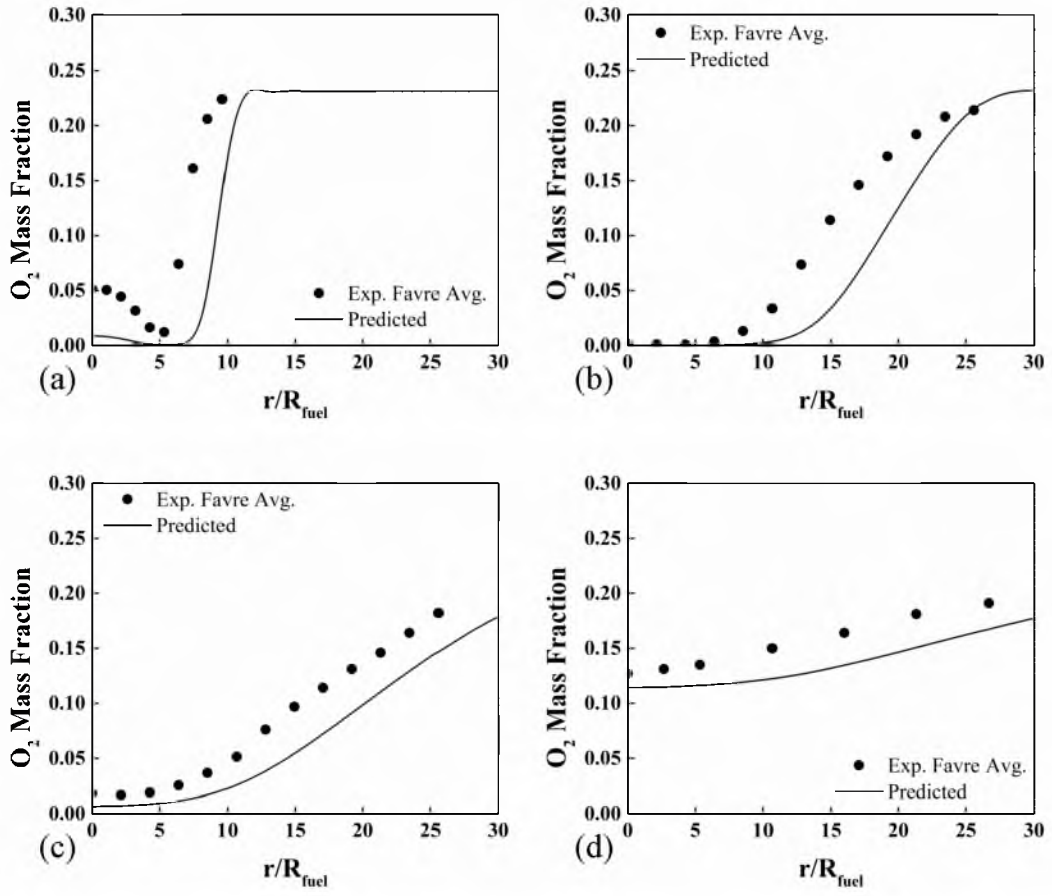

Figure 6.4: Radial O_2 mass fraction at various axial positions.
z/L = (a) 1/8, (b) 3/8, (c) 5/8, and (d) 1.

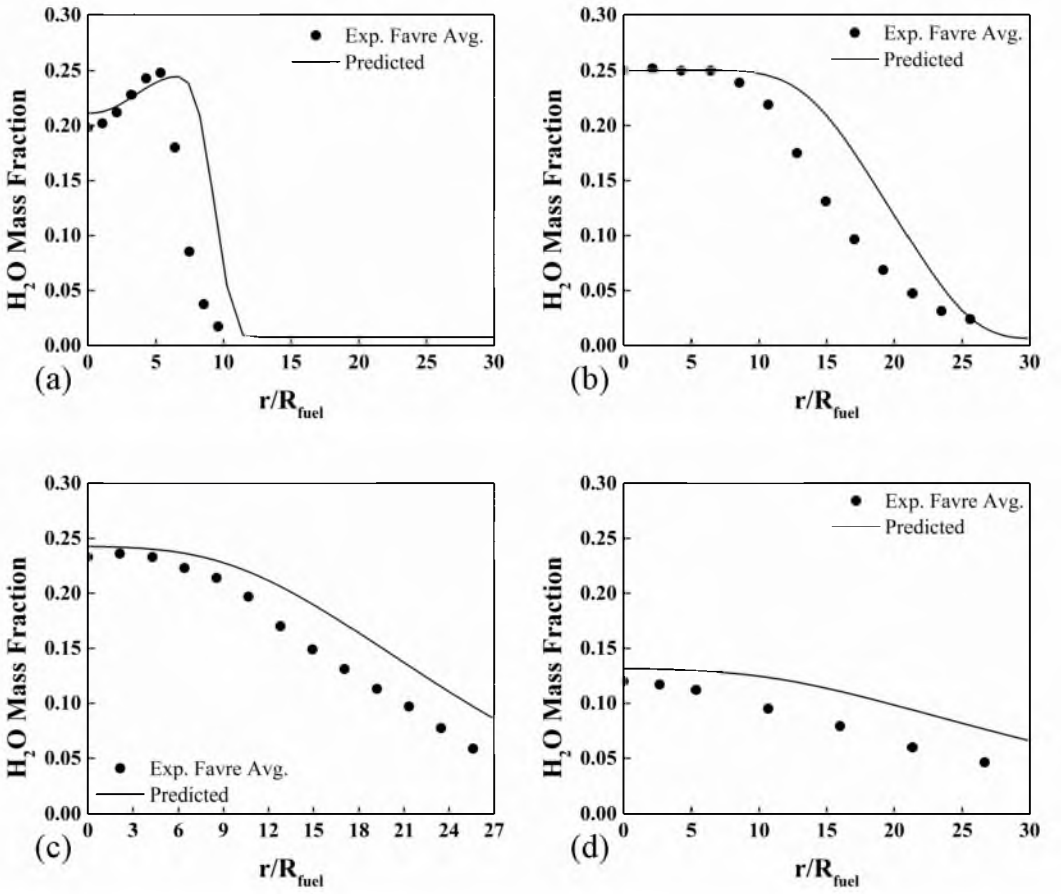

Figure 6.5: Radial H_2O mass fraction profiles at various axial positions. z/L = (a) 1/8, (b) 3/8, (c) 5/8, and (d) 1.

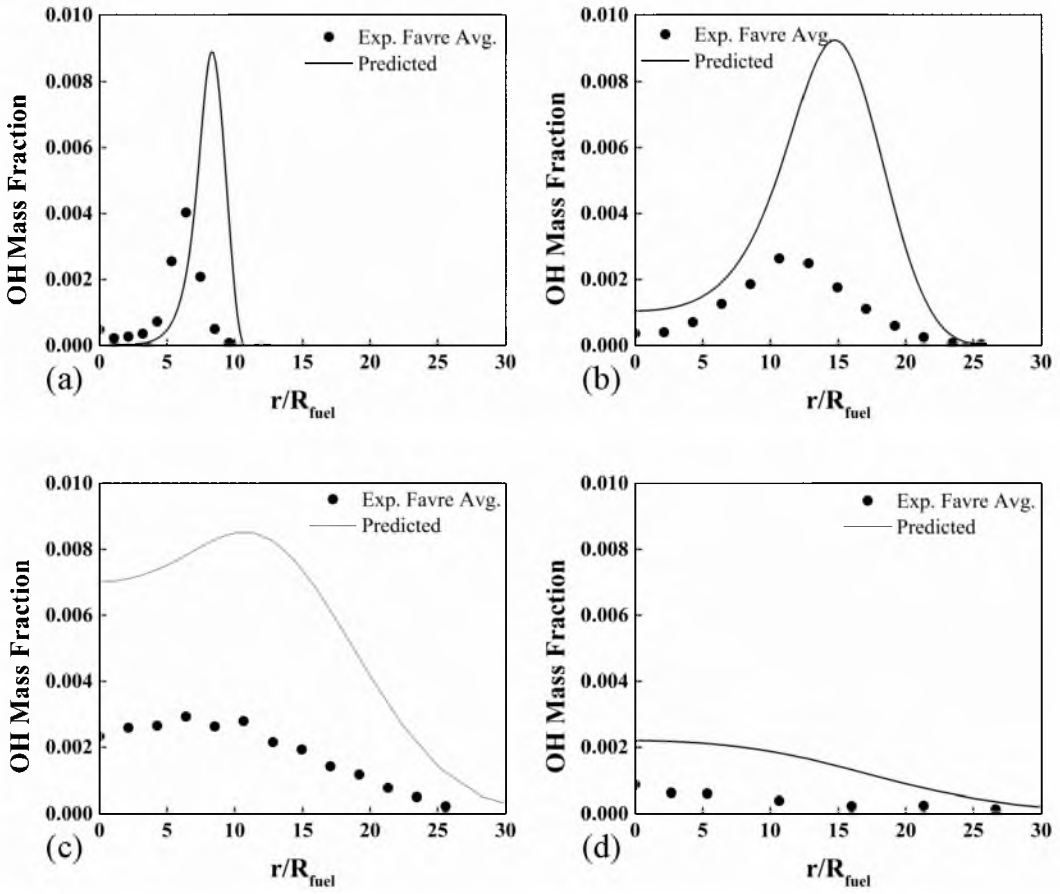

Figure 6.6: Radial OH mass fraction profiles at various axial positions.
z/L = (a) 1/8, (b) 3/8, (c) 5/8, and (d) 1.

measurements. The model overpredicts the consumption rate of oxygen (Figure 6.4) and the production rate of OH radicals (Figure 6.6). This behavior may be explained by the simplified nature of the adopted reaction mechanism (Subsection 6.2.1).

An exhaustive comparison between experimental data and model predictions is beyond the scope of this work. Such a study may require the implementation of advanced numerical techniques such as direct numerical simulation (DNS) and a comprehensive gas-phase reaction mechanism including hundreds of elementary reactions. These types of studies commonly contribute to the understanding of various specific phenomena occurring in flames such as the turbulence-chemistry interaction and the effect of various elementary chemical steps on flame ignition and stability.

Furthermore, these complex simulations are restricted to physical systems with simple flow configurations due to their large demand for computing time and resources. It is anticipated that the burner and injector geometries for the flash ironmaking reactor will involve complicated three-dimensional particle-laden flows (e.g., swirling flows). In this work, the objective was to develop a reliable simulation tool capable of representing complex particle-laden flows in a combusting environment. Thereby, predicting with reasonable accuracy the gas temperature and species distributions of a nonpremixed H_2-O_2 jet flame suffices.

6.4 Simulation of a Lab Flash Reactor

6.4.1 Basis of the Simulation Runs

The computational model was used to evaluate various designs of a hydrogen-oxygen nonpremixed burner to be installed in a lab flash reactor (LFR). The design was

aimed to quickly react the H_2-O_2 mixtures inside the reactor, which rapidly generates the hot reducing gas, thus better utilizing the reactor volume during the flash reduction of iron oxide concentrate particles.

The operating conditions for the lab flash reactor are determined by the following chemical reactions:

$$2H_2 + O_2 \rightarrow 2H_2O \tag{6-7}$$

Reaction (6-7) represents the combustion of hydrogen with oxygen. It is an irreversible and exothermic reaction that provides the energy required by the reduction process. The reduction of magnetite to metallic iron takes place in the following two successive steps:

$$Fe_3O_4 + H_2 = 3FeO + H_2O \tag{6-8}$$

$$FeO + H_2 = Fe + H_2O \tag{6-9}$$

In the temperature range of interest (1473–1873 K), Reactions (6-8) and (6-9) are reversible. The reduction of magnetite to wüstite [Reaction (6-8)] is considerably less equilibrium limited than the reduction of wüstite to metallic iron [Reaction (6-9)]. The latter is significantly limited by equilibrium and, consequently, a sufficiently large excess of hydrogen over the stoichiometric amount is required to substantially reduce wüstite to metallic iron [i.e., to achieve a high conversion for Reaction (6-9)]. This can be expressed in terms of an excess driving force defined by

$$\text{Excess Driving Force} = \frac{\dfrac{p_{H_2,off}}{p_{H_2O,off}} - \dfrac{p_{H_2,eq}}{p_{H_2O,eq}}}{\dfrac{p_{H_2,eq}}{p_{H_2O,eq}}} \tag{6-10}$$

where $p_{i,eq}$ and $p_{i,off}$ are the partial pressures of the ith species at equilibrium and in the off-gas, respectively. The off-gas partial pressures of H_2 and H_2O used in Equation (6-10)

are affected not only by the reduction process but also by the partial combustion of hydrogen.

The LFR operating conditions for the burner design simulation runs were selected based on a target nominal residence time between 2–7 seconds (Choi and Sohn, 2010). Concentrate particles consisting of magnetite (Fe_3O_4) and other gangue materials (mostly SiO_2) are fed to the reaction shaft at a maximum rate of 0.6 kg h^{-1}. Thermal energy generated by the partial combustion of hydrogen with oxygen compensates for the reactor heat loss and maintains an off-gas temperature of 1373 K. Excess hydrogen is supplied to maintain an excess driving force in the off-gas of 2.8 (250 % excess hydrogen). Material balances yield the required flow rates of hydrogen and oxygen to effect Reactions (6-8) and (6-9) to completion while maintaining the target excess driving force.

In this work, hydrogen is only consumed by combustion; that is, the gas-solid reduction reactions are not included in the model. In addition, the stoichiometry of Reaction (6-7) indicates that for every two moles of hydrogen that are consumed, two moles of water vapor are produced. As a result, the total volumetric flow rate of the gas mixture after combustion is equal to the input hydrogen volumetric flow rate. Hence, the total volumetric flow rates are used when referring to the lower (820 NL h^{-1}) and upper (8200 NL h^{-1}) operating conditions. In this section, the flow rates are given at normal condition; that is, 1 atm and 273 K.

Table 6.3 presents the lower (820 NL h^{-1}) and higher (8200 NL h^{-1}) operating conditions for the lab flash reactor. Table 6.4 shows the resulting nominal residence times for the gas mixture and particles. It is noted that the particle nominal residence time

Table 6.3 Operating Conditions for the Lab Flash Reactor.

Parameter	Values	
	Lower	Higher
Solid concentrate		
Feed rate, kg h^{-1}	0.06	0.6
Average particle size, μm	32	32
Process Gases		
Hydrogen (H_2)		
Flow rate, NL h^{-1}	820	8200
Input temperature, K	1273	1273
Oxygen (O_2)		
Flow rate, NL h^{-1}	56	560
Input temperature, K	298	298
Furnace wall temperature, K	1373	1373
Off-gas H_2/H_2O molar ratio	5.14	5.14
Excess driving force	2.8	2.8

Table 6.4: Nominal Residence Times in the Lab Flash Reactor.

Parameter	Values	
	Lower	Higher
Average gas velocity[a], m s^{-1}	0.05	0.5
Particle terminal velocity, m s^{-1}	0.10	0.10
Nominal residence times, s		
Gas mixture	21.6	2.2
Particles	6.7	1.8

[a]Calculated at 1373 K.

ranges from 1.8 (820 NL h^{-1}) to 6.7 (8200 NL h^{-1}) seconds. In this work, the nominal residence time of the iron oxide concentrate particles was calculated using the methodology developed by Choi (2010) and considering a reaction zone length of 1 m.

6.4.2 Simulation Strategy

Two-dimensional axisymmetric simulations were first carried out to obtain basic information about the proposed nozzle design such as the ratio of linear inlet velocities of hydrogen and oxygen, the stability of H_2-O_2 flame, and the flame length. A three-dimensional simulation approach was then undertaken for more detailed and practical analysis considering the fact that the proposed nozzle design was three-dimensional in nature.

Figure 6.7 shows the three-dimensional geometry of the lab flash reactor with the designed burner. The latter consists of four H_2 special pattern slotted ports surrounding four O_2 inlet ports. This configuration was chosen so that the H_2 distribution provides a shielding effect on the O_2 mass transfer. Tables 6-5 and 6-6 present the parameters used in the simulation runs of the lower and higher operating conditions. Due to symmetry, only one-fourth of the reactor was simulated. The resulting computational mesh consisted of 292 566 cells.

6.4.3 Distributions of Velocity, Temperature and Species Concentrations

Figures 6.8 and 6.9 show gas streamlines for the low (820 NL h^{-1}) and high (8200 NL h^{-1}) hydrogen flow rate conditions, respectively. A streamline represents the path of a

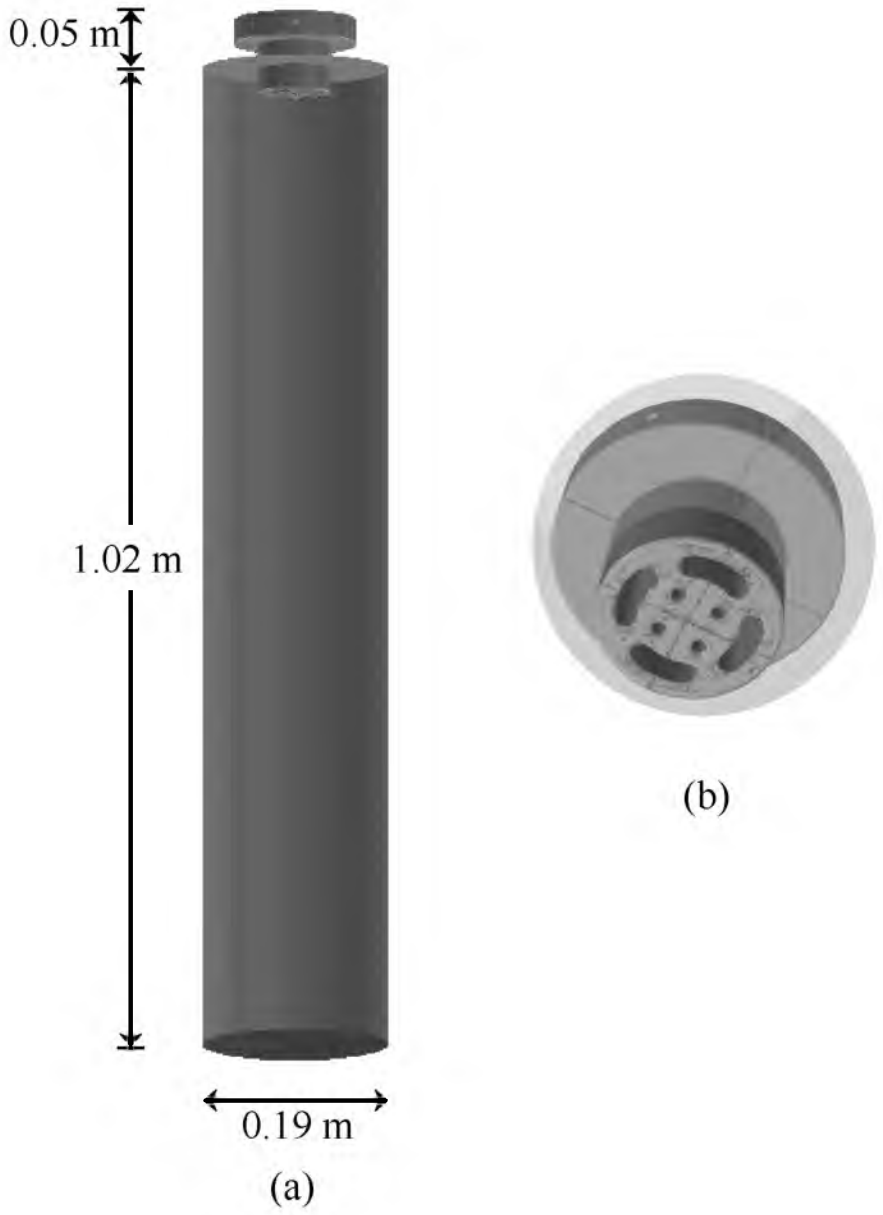

Figure 6.7: Schematic representation of the three-dimensional geometry used in the simulation of the lab flash reactor.
(a) Reactor and (b) designed burner.

Table 6.5: General Parameters for the Simulation Runs of the Lab Flash Reactor.

Parameter	Value
Reactor geometry	
Diameter, m	0.19
Length, m	1.016
Wall temperature	
Top reactor wall	1373
Side reactor wall	1373
Convective heat transfer coefficient, W m^{-2} K^{-1}	
External burner walls	10.9
Surface emissivities (inlets, outlet and walls)	0.3
Particle streams	
Temperature, K	298
Particle velocity, m s^{-1}	0.10
Particle density, kg m^{-3}	5170
Number of injection points for the cloud model	3
Cloud diameters, m	
Minimum	6.3×10^{-3}
Maximum	0.19

Table 6.6: Inlet Boundary Conditions for the Simulation of the Lab Flash Reactor.

Parameter	Values	
	Lower	Higher
Hydrogen stream		
Temperature, K	1273	1273
Mass flow rate, kg s^{-1}	5.2×10^{-6}	5.2×10^{-6}
Turbulent intensity, %	5	5
Hydraulic diameter, m	0.0064	0.0064
Oxygen stream		
Temperature, K	298	298
Mass flow rate, kg s^{-1}	5.6×10^{-6}	5.6×10^{-6}
Turbulent intensity, %	5	5
Hydraulic diameter, m	0.0064	0.0064

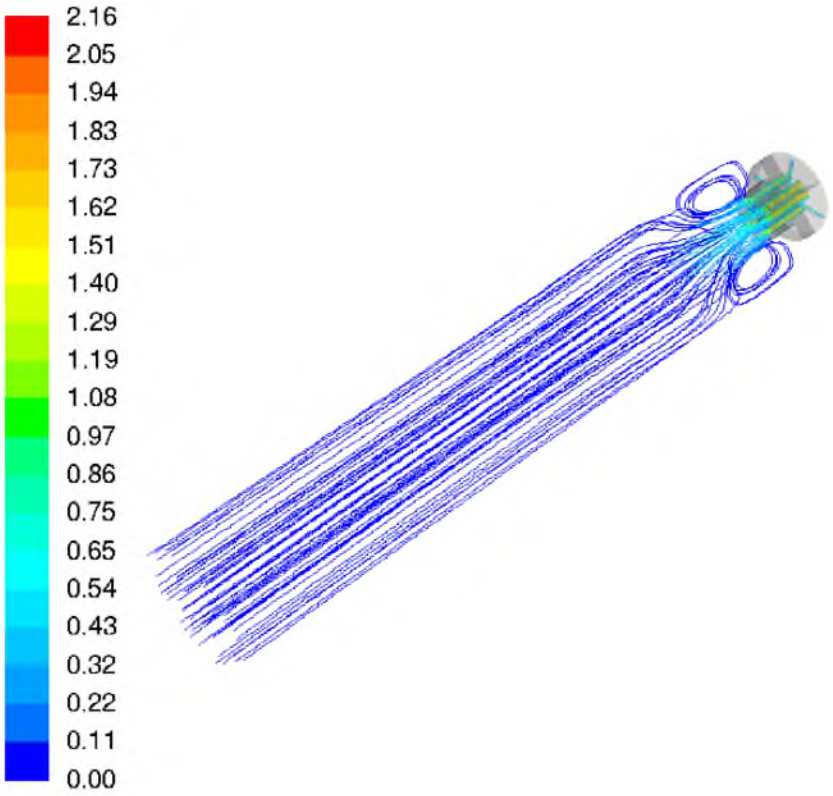

Figure 6.8: Gas streamlines inside the lab flash reactor. Lower flow rate (820 NL h^{-1}) condition. Color scale represents velocity magnitude. Values in m s^{-1}.

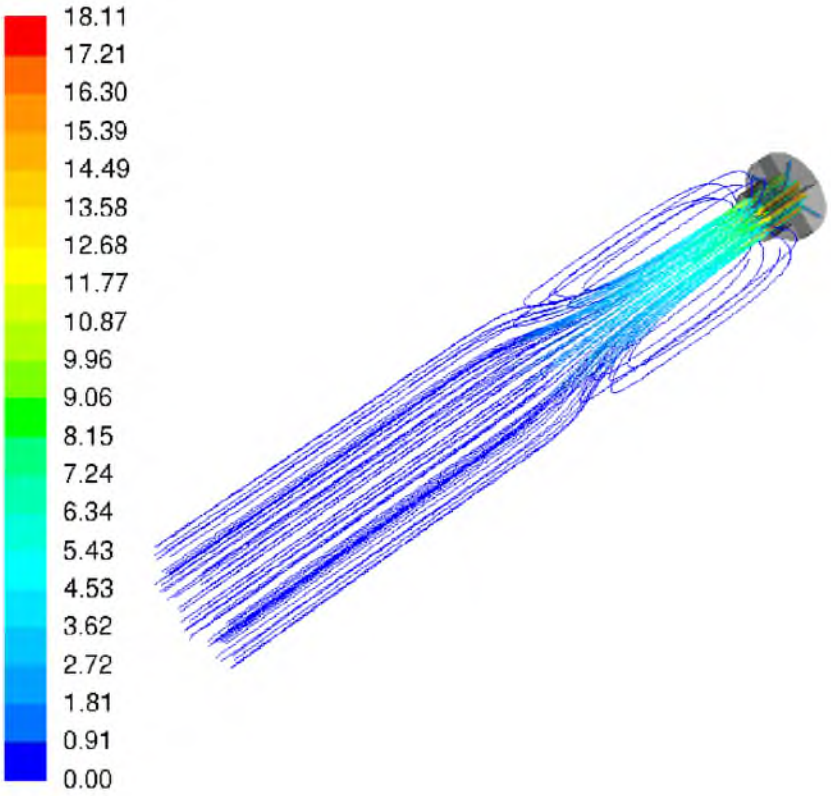

Figure 6.9: Gas streamlines inside the lab flash reactor. Higher flow rate (8200 NL h^{-1}) condition. Color scale represents velocity magnitude. Values in m s^{-1}.

fluid element. It is noted that the radial expansion of the gas flow is simulated correctly. In both cases, recirculation zones are formed due to the lack of a surrounding secondary flow that can sustain the entrainment rate of the jet flame (Beer and Chigier, 1972). The length of the recirculation zone at a low hydrogen flow rate is significantly shorter than that at a high hydrogen flow rate. The latter is a result of the faster entrainment rate of the high flow rate flame. The flame length is proportional to the length of the recirculation zone in confined diffusion flames.

Figure 6.10 shows a comparison of the temperature distributions inside the reactor. The maximum flame temperatures for the lower (820 NL h^{-1}) and higher operating (820 NL h^{-1}) conditions were 2726 and 3155 K, respectively. The latter value is close to the adiabatic flame temperature (3079 K) of a stoichiometric H_2-O_2 mixture (Turns, 2012). It was found that the largest portion of the combustion reactions in the lower condition flame takes place in the vicinity of the O_2 port. It is noted that the higher condition flame provides a higher temperature and a longer flame compared to that of the lower condition.

In this work, the temperature distribution was found to be affected not only by the combustion reaction but also by the heat loss from the reactor. For a small scale reactor like the lab flash reactor, higher heat release rates from the burner are necessary to achieve and/or maintain high temperatures inside the reactor. Unfortunately, a higher heat release from the burner would translate into an increase in the flow rates of hydrogen and oxygen which, in turn, would shorten the residence time of the particles.

The consumption of O_2 is a major concern in the design of the nozzle. Thus, the

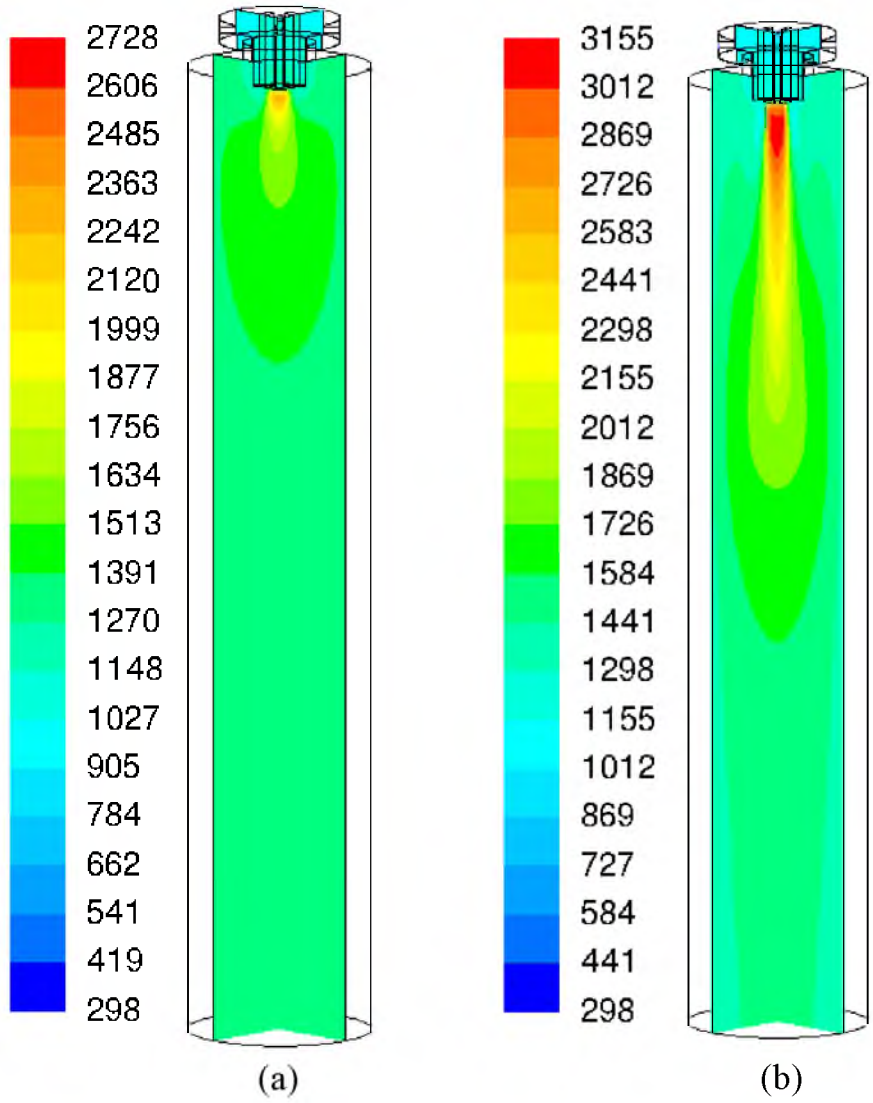

Figure 6.10: Contours of temperature in the lab flash reactor. Values in kelvins. Total flow rates: (a) 820 and (b) 8200 NL h^{-1}.

design of the nozzle is aimed at providing the best O_2 shielding; that is, O_2 should not be transferred out of the flame core. Figure 6.11 shows the O_2 mole fraction distributions. In both cases, O_2 does not escape beyond the shield provided by H_2. It is also noted that its complete consumption takes place within 15 cm from the nozzle tip in the axial direction in both cases. The above results indicate that the designed nozzle is promising.

Figure 6.12 shows a comparison of the H_2/H_2O molar ratio distributions for the lower (820 NL h^{-1}) and higher (8200 NL h^{-1}) operating conditions. This ratio represents the excess driving force for the reduction reactions. In both cases, the expected off-gas H_2/H_2O molar ratio is 5.14, that is, $\log_{10}(H_2/H_2O) = 0.71$. The upper values in the color scale (e.g., red color, $H_2/H_2O = 32$) represent zones rich in hydrogen, that is, highly reducing. These are narrow zones located in the mixing region next to the flame. In contrast, the lower values (e.g., dark blue, $H_2/H_2O = 0.032$) correspond to lean hydrogen zones, that is, highly oxidizing. These zones are concentrated within the flame core which is where most of the water vapor is generated. In both cases, homogenous distributions of H_2/H_2O are developed once the flame zone is passed.

By comparing Figures 6-10 and 6-12, it is noted that the flame length determines the length of the homogenous H_2/H_2O molar ration zones. Larger flames result in shorter homogeneous H_2/H_2O zones. From the point of view of reactor design, it is therefore desirable to generate shorter flames because they will provide larger homogenous temperature and H_2/H_2O (excess driving force) distributions and thus, improved reactor volume utilization. In this work, the length of the simulated flames was only a function of the volumetric flow rates of oxygen. Hence, the shorter flame was generated at the

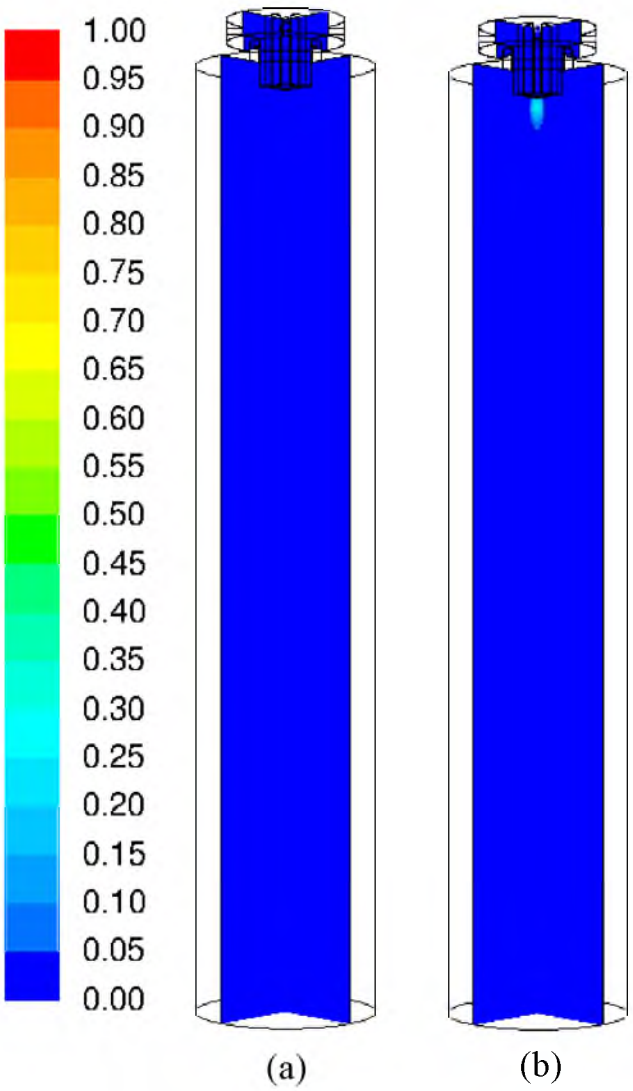

Figure 6.11: Contours of O_2 mass fraction inside the lab flash reactor.
Total flow rates: (a) 820 and (b) 8200 NL h^{-1}.

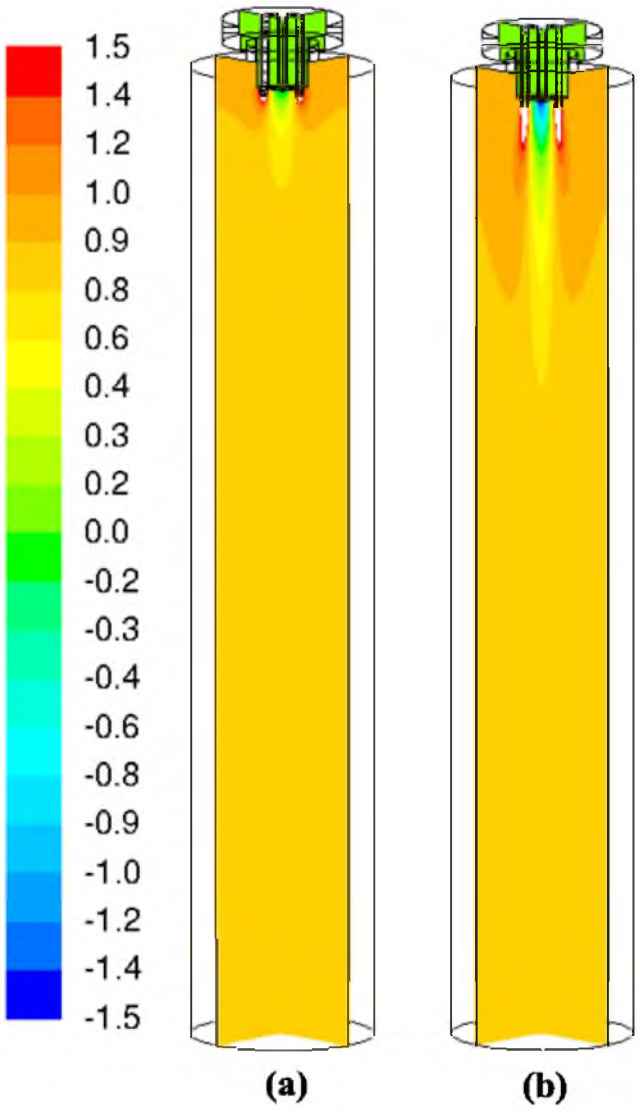

Figure 6.12: Contours of H_2/H_2O molar ratio inside the lab flash reactor. Total flow rates: (a) 820 and (b) 8200 NL h^{-1}. Scale values indicate logarithm (base 10) of the H_2/H_2O molar ratio.

expense of a lower heating rate from the burner. This restriction can be eliminated by using swirl burners. By controlling the amount of angular momentum imparted to the fuel and oxidant streams, the length and shape of the flame can be controlled.

6.4.4 Motion and Heating of Iron Oxide Concentrate Particles

The interaction of iron oxide concentrate particles with the gas phase was incorporated into the simulation from a Lagrangian viewpoint. Uniform size inert particles capable of interchanging momentum and energy with the surroundings were injected from three points evenly located on the burner surface center within a diameter of 6.35 mm. Tables 6.5 and 6.6 show the parameters used in the simulations. The predicted mass-average particle residence times were compared with nominal ones for the lower (820 NL h^{-1}) and higher (8200 NL h^{-1}) operating conditions.

Due to the heating of the particles, the maximum gas temperature (Figure 6.13) decreased by about 200 K [see Figure 6.10(b)] for the higher condition (8200 NL h^{-1}). Figure 6.14 shows a comparison of the mass-average particle temperature profiles along the reactor axis. For the lower (820 NL h^{-1}) condition, the particles reached a maximum temperature lower than 2000 K. In contrast, particles reached a maximum temperature close to 2500 K in the higher flow (8200 NL h^{-1}). In both cases, these high maximum temperatures will lead to the melting of the concentrate particles.

Figure 6.15 shows particle trajectories for the higher (8200 NL h^{-1}) condition. Under this condition, the maximum particle residence time at 1 m from the injection point is approximately 0.5. Figure 6.16 shows a comparison of the mass-average particle

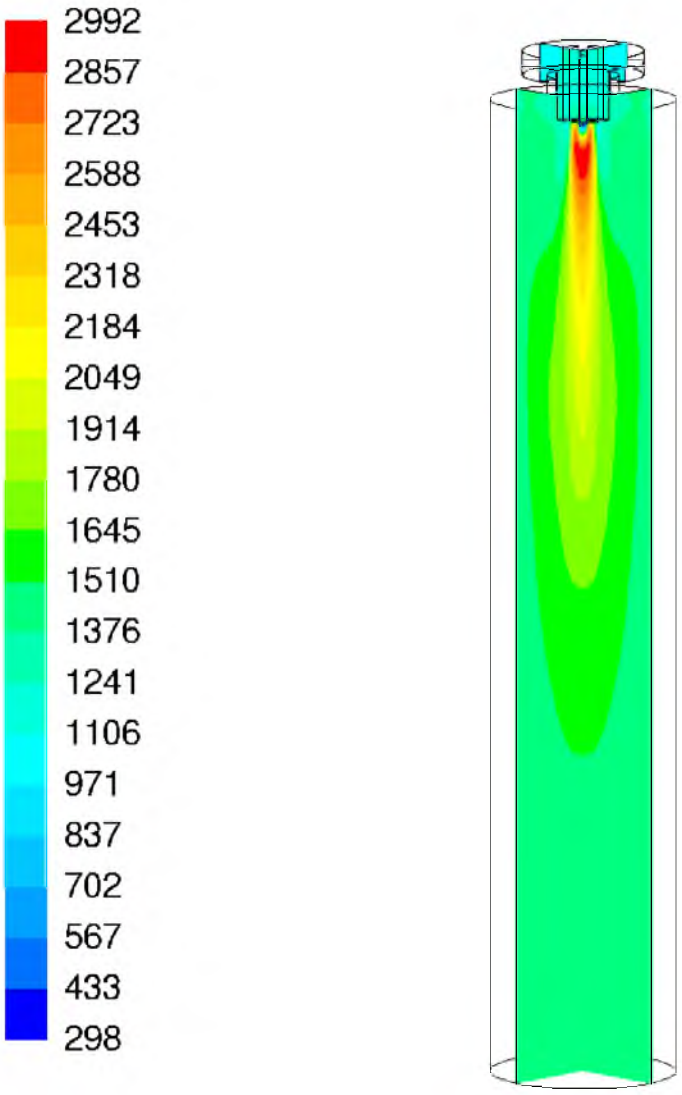

Figure 6.13: Contours of temperature inside the lab flash reactor for the higher (8200 NL h^{-1}) condition. Particle heating by the gas phase is accounted for in the calculations. Values in kelvins.

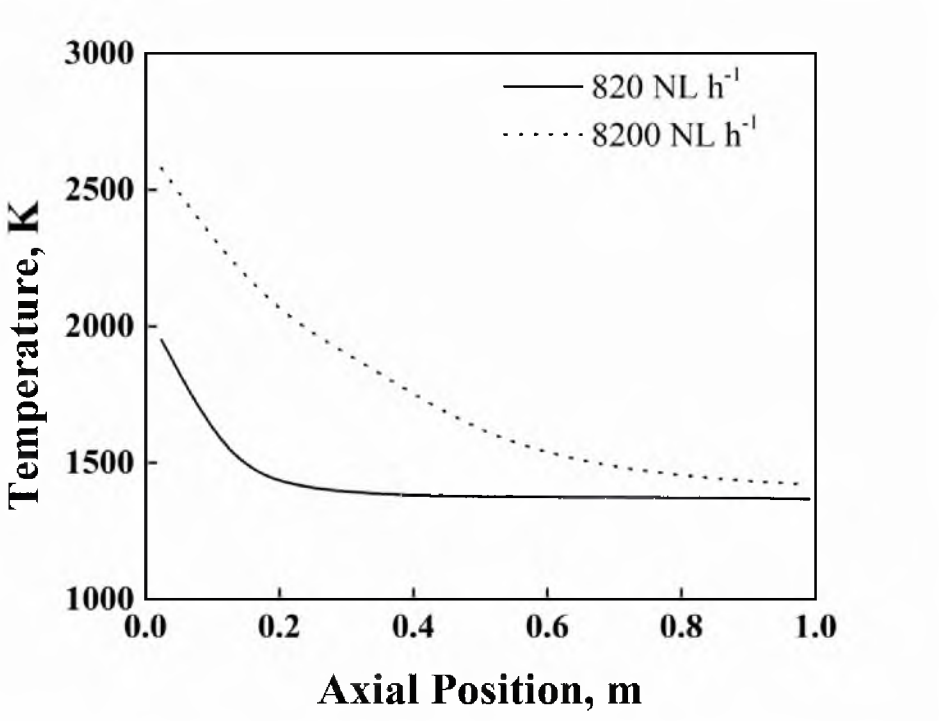

Figure 6.14: Comparison of computed mass-average particle temperatures.

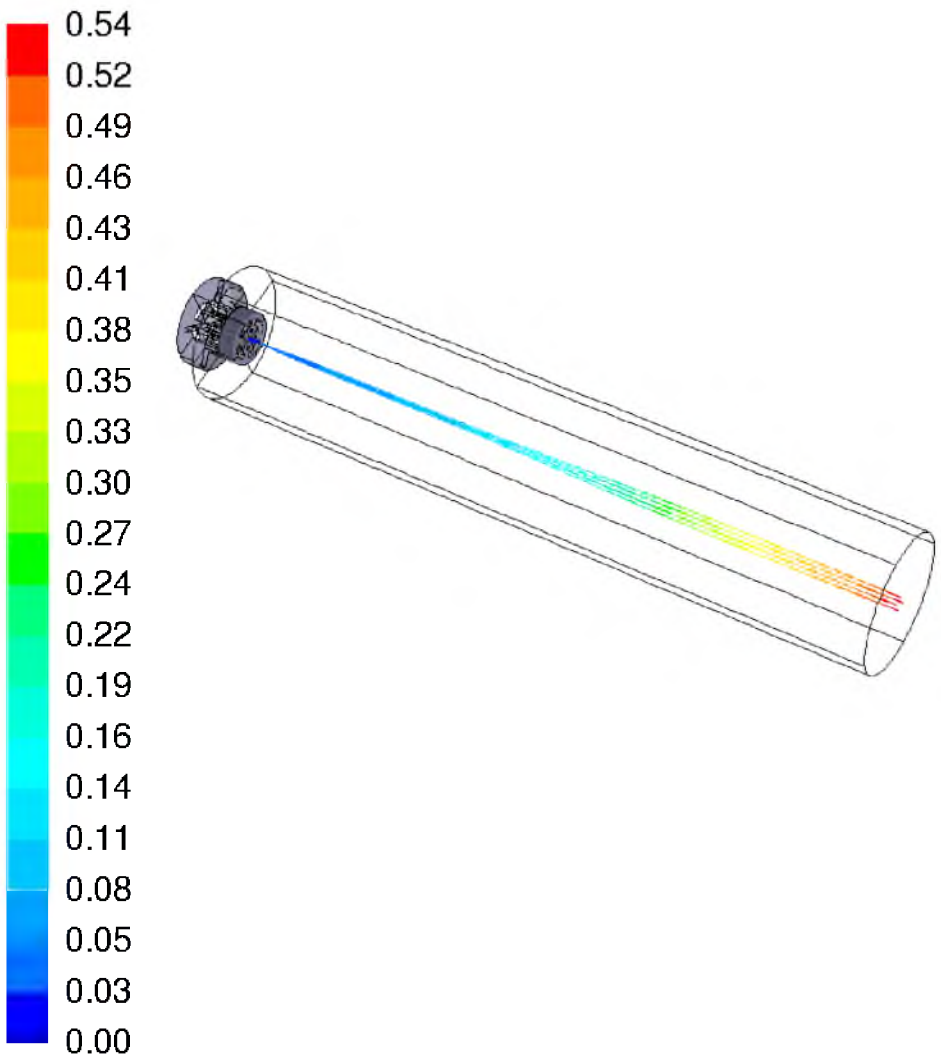

Figure 6.15: Particle trajectories colored by residence time inside the lab flash reactor at the higher (8200 NL h^{-1}) condition. Values in s.

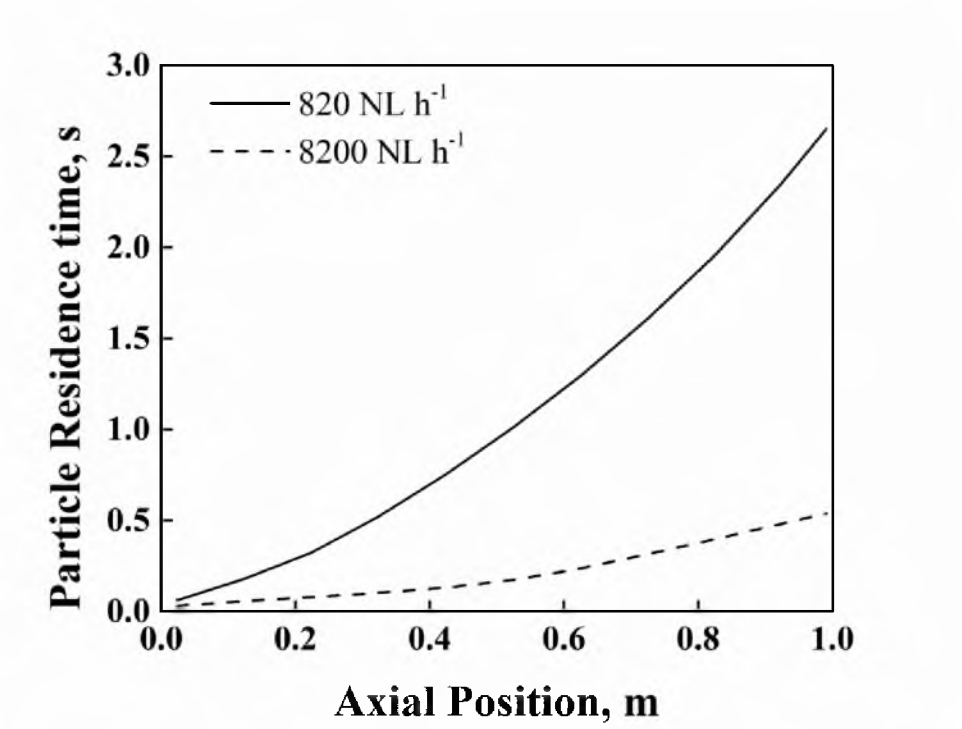

Figure 6.16: Comparison of computed mass-average particle residence time.

residence time profiles along the reactor axis. At 8200 NL h^{-1}, the predicted average particle residence time is 0.5 s at the reactor outlet. This value is significantly shorter than the nominal time of 1.8 s (see Table 6.4). At 8200 NL h^{-1}, the predicted average residence time is 2.5 s at the reactor outlet. Again, this time is shorter than the nominal time of 6.7 s.

The importance of coupling fluid dynamics calculations with the particle force balance [Equation (6-5)] to obtain realistic particle residence times was demonstrated. Shorter residence times result from the exchange of momentum between particles and gas and from nonideal flow patterns. Therefore, CFD-based particle residence times should be calculated when analyzing experimental reduction degrees and/or designing reaction

vessels (i.e., selection of length and diameter). Furthermore, the ability to calculate particle trajectories will be useful for devising the best method for injecting the concentrate particles in the flash reactor.

In summary, the model was capable of simulating the simultaneous interaction of the hydrogen-oxygen combustion with the presence of iron oxide concentrate particles in a complex three-dimensional geometry. This model will be instrumental for the design of components (burner, reactor, particle injectors) as well as the scale up of this novel flash ironmaking technology.

6.5 Concluding Remarks

A three-dimensional computational fluid dynamics model was developed for a novel flash ironmaking process. The model incorporates the turbulent governing equations of overall continuity, momentum, energy, and species transport including gas-phase reaction kinetics. The comparison of the model predictions with benchmark experimental data of a nonpremixed hydrogen jet flame showed good agreement in terms of gas temperature and species concentrations. The model was used to evaluate the design of a hydrogen-oxygen burner for a lab flash reactor. The distributions of velocity, temperature, and species concentrations, and the concentrate particle trajectories in a lab flash reactor were computed and analyzed.

The model was capable of simulating the simultaneous interaction of the hydrogen-oxygen combustion with the presence of iron oxide concentrate particles in a complex three-dimensional geometry. The importance of CFD modeling for predicting more realistically the residence time of concentrate particles was demonstrated. The

present model shows potential as a useful tool for further design and scale up of this novel flash ironmaking technology.

7. CONCLUSIONS AND RECOMMENDATIONS

7.1 Conclusions

Computational fluid dynamic modeling was conducted for three chemically-reacting gas-particle flows: chemical vapor synthesis of tungsten carbide and aluminum nanopowders, flame synthesis of silica nanopowder, and a novel flash ironmaking process based on the direct gaseous reduction of iron oxide concentrate particles. The conclusions from this work can be summarized as follows.

The chemical vapor synthesis of tungsten carbide nanopowder from tungsten hexachloride in a tubular reactor was simulated by a two-dimensional multiphase computational fluid dynamic (CFD) model. A parametric study was conducted to determine the nucleation and growth rate constants. Experimental results obtained for the synthesis of WC nanopowder from WCl_6 with H_2 and CH_4 in a tubular reactor system were used to validate the model. The combination of nucleation rate and growth rate constants that yielded the best agreement with experimental data was determined. It is noted that this work is the first application of CFD in the chemical vapor synthesis of WC nanopowder.

The synthesis of silica nanopowder from tetraethylorthosilicate in a bench-scale flame spray pyrolysis reactor was simulated. The transport and evaporation of liquid droplets were treated from a Lagrangian viewpoint. The population balance model was solved for particles undergoing homogeneous nucleation and Brownian coagulation. The

nucleation rate was computed based on the rates of thermal decomposition and oxidation of the precursor with no adjustable parameters. The computed results show that the model is capable of reproducing the magnitude as well as the variations of the average particle diameter with different experimental conditions using a single value of the collision efficiency factor.

Three-dimensional simulations of a chemical vapor synthesis reactor of aluminum nanopowder were performed. The nucleation rate was computed using an expression from the classical nucleation theory. The growth rate was obtained by the combined effect of vapor condensation and coagulation. The comparison of the model predictions with the available experimental data showed good agreement under different operating conditions without the need of adjustable parameters. Computed results indicated that particle aggregation determined the final particle size in the simulated chemical vapor synthesis reactor.

In the simulation of the flash ironmaking reactor, the comparison of the model predictions with benchmark experimental data of a nonpremixed hydrogen jet flame showed good agreement in terms of gas temperature and species concentrations. The model was used to evaluate the design of a hydrogen-oxygen burner for a lab flash reactor. The distributions of velocity, temperature, and species concentrations, and the concentrate particle trajectories in a lab flash reactor were computed and analyzed.

The model was capable of simulating the simultaneous interaction of the hydrogen-oxygen combustion with the presence of iron oxide concentrate particles in a complex three-dimensional geometry. Analysis of the predicted particle residence times inside the lab flash reactor demonstrated the importance of CFD calculations for

residence time calculations. The present model shows potential as a useful tool for further design and scale up of this novel flash ironmaking technology.

In summary, chemically reacting gas-particle flows involve complex interactions between physical and chemical processes, and as a result, they are difficult to study by traditional experimental methods alone. Consequently, methodologies based on computational modeling represent the best alternative to design and operate such processes. For example, successful commercialization of the novel ironmaking process depends largely on our ability to scale up the laboratory experimental setups. Furthermore, the operational optimization of existing processes such as the flame synthesis of silica nanopowder can also benefit from the application of mathematical models, such as the one developed in this work.

7.2 Recommendations

The development of theory-based expressions for the nucleation and growth of tungsten carbide nanoparticles and an expression for the rate of sintering of silica nanoparticles based on experimental data are recommended. These improvements would make the model presented in this work more realistic and would reduce the need of adjustable parameters.

Further experimental work characterizing the evolution of tungsten carbide and silica nanoparticles as a function of the reactor axial position would also be beneficial. This would provide more experimental data in the development of more realistic models for the nucleation and growth processes. It would also provide more experimental data for model validation.

For the simulation of the flash ironmaking reactor, it is recommended that a gas-solid reaction rate expression be incorporated into the model for predicting the reduction rate of iron oxide concentrate particles in hydrogen-containing gaseous streams.

REFERENCES

ANSYS, Inc. *ANSYS FLUENT Theory Guide*; Canonsburg, PA, 2011.

Ban, Z.-G.; Shaw, L. L. Synthesis and Processing of Nanostructured WC-Co Materials. *J. Mater. Sci.* **2002**, *37* (16), 3397-3403.

Barlow, R. S. Sandia H_2/He Flame Data – Release 2.0. http://www.ca.sandia.gov/TNF. Sandia National Laboratories, 2003.

Barlow, R. S.; Carter, C. D. Raman/Rayleigh/LIF Measurements of Nitric Oxide Formation in Turbulent Hydrogen Jet Flames. *Combust. Flame* **1994**, *97* (3-4), 261-280.

Barlow, R. S.; Carter, C. D. Relationships Among Nitric Oxide, Temperature, and Mixture Fraction in Hydrogen Jet Flames. *Combust. Flame* **1996**, *104* (3), 288-299.

Beér, J. M.; Chigier, N. A. *Combustion Aerodynamics;* Wiley.: New York, 1972; pp 43-45.

Bird, R. B.; Stewart, W. E.; Lightfoot, E. N. *Transport Phenomena*, Revised 2nd ed.; Wiley: New York, 2007; pp 77, 80, 315, 337, 583.

Bolsaitis, P. P.; McCarthy, J. F.; Mohiuddin, G.; Elliott, J. F. Formation of Metal Oxide Aerosols for Conditions of High Supersaturation. *Aerosol Sci. Technol.* **1987**, *6* (3), 225-246.

Chang, H. K.; Park, J. H.; Jang, H. D. Flame Synthesis of Silica Nanoparticles by Adopting Two-Fluid Nozzle Spray. *Colloids Surf., A* **2008**, *313-314*, 140-144.

Chang, W.; Skandan, G.; Hahn, H.; Danforth, S. C.; Kear, B. H. Chemical Vapor Condensation of Nanostructured Ceramic Powders. *Nanostruct. Mater.* **1994**, *4* (3), 345-351.

Choi, M. E. Suspension Hydrogen Reduction of Iron Ore Concentrate. Ph.D. Dissertation, The University of Utah, Salt Lake City, UT, 2010.

Choi, M. E.; Sohn, H. Y. Development of Green Suspension Ironmaking Technology Based on Hydrogen Reduction of Iron Oxide Concentrate: Rate Measurements. *Ironmaking Steelmaking* **2010**, *37* (2), 81-88.

Choi, J. W.; Sohn, H. Y.; Choi Y. J.; Fang, Z. Z. Chemical Vapor Synthesis and Characterization of Aluminum Nanopowder. *J. Power Sources* **2010**, *195* (5), 1463-1471.

Chu, J. C. S.; Breslin, J.; Wang, N. S.; Lin, M. C. Relative Stabilities of Tetramethyl Orthosilicate and Tetraethyl Orthosilicate in the Gas Phase. *Mater. Lett.* **1991**, *12* (3), 179-184.

Ehrman, S. H. Effect of Particle Size on Rate of Coalescence of Silica Nanoparticles. *J. Colloid Interface Sci.* **1999**, *213* (1), 258-261.

Ehrman, S. H.; Friedlander, S. K.; Zachariah, M. R. Characteristics of SiO_2/TiO_2 Nanocomposite Particles Formed in a Premixed Flat Flame. *J. Aerosol Sci.* **1998**, *29* (5-6), 687-706.

Eklund, D. R.; Drummond, J. P.; Hassan, H. A. Calculation of Supersonic Turbulent Reacting Coaxial Jets. *AIAA J.* **1990**, *28* (9), 1633-1641.

Fang, Z.; Maheshwari, P.; Wang, X.; Sohn H. Y.; Griffo, A.; Riley, R. An Experimental Study of the Sintering of Nanocrystalline WC-Co Powders. *Int. J. Refract. Met. Hard Mater.* **2005**, *23* (4-6), 249-257.

Fitzsimmons, M; Sarin, V. K. Comparison of WCl_6-CH_4-H_2 and WF_6-CH_4-H_2 Systems for Growth of WC Coatings. *Surf Coat. Technol.* **1995**, *76-77*, 250-255.

Friedlander, S. K. *Smoke, Dust, and Haze: Fundamentals of Aerosol Dynamics;* Oxford: New York, 2000; pp 14-16, 276, 306-312.

Fu, L.; Cao, L. H.; Fan, Y. S. Two-Step Synthesis of Nanostructured Tungsten Carbide-Cobalt Powders. *Scr. Mater.* **2001**, *44* (7), 1061-1068.

Gao, L.; Kear, B. H. Low Temperature Carburization of High Surface Area Tungsten Powders. *Nanostruct. Mater.* **1995**, *5* (5), 555-569.

Gavi, E.; Rivautella, L.; Marchisio, D. L.; Vanni, M.; Barresi, A. A; Baldi, G. CFD Modelling of Nano-Particle Precipitation in Confined Impinging Jet Reactors. *Chem. Eng. Res. Des.* **2007**, *85* (5), 735-744.

Geankoplis, C. J. *Transport Processes and Unit Operations*, 3rd ed.; Prentice-Hall: Upper Saddle River, NJ, 1993; p 256.

Gleiter, H. Nanocrystalline Materials. *Prog. Mater. Sci.* **1989**, *33* (4), 223-315.

Hasanpour, A.; Mozaffari, M.; Amighian, J. Preparation of Bi-Fe_3O_4 Nanocomposite through Reduction of Bi_2O_3 with Fe Via High-Energy Ball Milling. *Phys. B (Amsterdam, Nerth.)* **2007**, *387* (1-2), 298-301.

Hojo, J.; Oku, T.; Kato, A. Tungsten Carbide Powders Produced by the Vapor Phase Reaction of the WCl_6-CH_4-H_2 System. *J. Less-Common Met.* **1978**, *59* (1), 85-95.

Hottel, H. C.; Noble, J. J.; Sarofim, A. F.; Silcox, G. D.; Wankat, P. C.; Knaebel, K. S. Heat and Mass Transfer. In *Perry's Chemical Engineer's Handbook,* 8th ed.; Green, D. W., Perry, R. H., Eds.; McGraw-Hill: Blacklick, OH, 2008; pp 5-30 – 5-35.

Jang, H. D. Experimental Study of Synthesis of Silica Nanoparticles by a Bench-Scale Diffusion Flame Reactor. *Powder Technol.* **2001**, *119* (2-3), 102-108.

Jang, H. D.; Chang, H. K.; Suh, Y.; Okuyama, K. Synthesis of SiO_2 Nanoparticles from Sprayed Droplets of Tetraethylortosilicate by the Flame Spray Pyrolysis. *Current Applied Physics* **2006**, *6* (Suppl. 1), e110-e113.

Johannessen, T.; Pratsinis, S. E.; Livbjerg, H. Computational Fluid-Particle Dynamics for the Flame Synthesis of Alumina Particles. *Chem. Eng. Sci.* **2000**, *55* (1), 177-191.

Kim, J. C.; Kim, B. K. Synthesis of Nanosized Tungsten Carbide Powder by the Chemical Vapor Condensation Process. *Scr. Mater.* **2004**, *50* (7), 969-972.

Kodas, T. T.; Hampden-Smith, M. J. *Aerosol Processing of Materials;* Wiley: New York, 1999; pp 97-100.

Launder, B. E.; Spalding, D. B. *Mathematical Models of Turbulence;* Academic: London, 1972.

Lee, G.-H.; Kang, S. Sintering of Nano-sized WC-Co Powders Produced by a Gas Reduction-Carburization Process. *J. Alloys Compd.* **2006**, *419* (1-2), 281-289.

Lehtinen, K. E. J.; Windeler, R. S.; Friedlander, S. K. A Note on the Growth of Primary Particles in Agglomerate Structures by Coalescence. *J. Colloid Interface Sci.* **1996**, *182* (2), 606-608.

Liu, S.; Huang, Z.-L.; Liu, G.; Yang, G. B. Preparing Nano-Crystalline Rare Earth Doped WC/Co Powder by High Energy Ball Milling. *Int. J. Refract. Met. Hard Mater.* **2006**, *24* (6), 461-464.

Magnussen, B. F. On the Structure of Turbulence and a Generalized Eddy Dissipation Concept for Chemical Reaction in Turbulent Flow. Presented at 19th AIAA Meeting, St. Louis, MI, January 12-15, 1981.

Magnussen, B. F.; Hjertager, B. H. On Mathematical Modeling of Turbulent Combustion with Special Emphasis on Soot Formation and Combustion. *Symp. (Int.) Combust.* **1977**, *16* (1) 719-729.

McCandlish, L. E.; Kear, B. H.; Kim, B. K. Processing and Properties of Nanostructured WC-Co. *Nanostruct. Mater.* **1992**, *1* (2), 119-124.

McGraw, R. Description of Aerosol Dynamics by the Quadrature Method of Moments. *Aerosol Sci. Technol.* **1997**, 27 (2), 255-265.

Mi, S.; Courtney, T. H. Synthesis of WC and WC-Co Cermets by Mechanical Alloying and Subsequent Hot Isostatic Pressing. *Scr. Mater.* **1997**, *38* (1), 171-176.

Nersisyan, H. H.; Won, H. I.; Won, C. W.; Lee, J. H. Study of the Combustion Synthesis Process of Nanostructured WC and WC-Co. *Mater. Chem. Phys.* **2005**, *94* (1), 153-158.

Olivas-Martinez, M.; Sohn, H. Y.; Jang, H. D. Silica Nanopowder from Waste Silicon Sludge and CFD Modeling of the Flame Spray Pyrolysis Process. In *REWAS 2008--Global Symposium on Recycling, Waste Treatment and Clean Technology, Proceedings,* Cancun, Mexico, Oct 12-15, 2008; Mishra, B., Ludwig, C., Das, S., Eds.; Minerals, Metals & Materials Society: Warrendale, PA, 2008; pp 631-638.

Panda, S.; Pratsinis, S. E. Modeling the Synthesis of Aluminum Particles by Evaporation-Condensation in an Aerosol Flow Reactor. *Nanostruct. Mater.* **1995**, *5* (7-8) 755-767.

Petersson, A.; Ågren, J. Constitutive Behaviour of WC-Co Materials with Different Grain Size Sintered Under Load. *Acta Mater.* **2004**, *52* (7), 1847-1858.

Prakash, A.; Bapat, A. P.; Zachariah, M. R. A Simple Numerical Algorithm and Software for Solution of Nucleation, Surface Growth, and Coagulation Problems. *Aerosol Sci. Technol.* **2003**, *37* (11), 892-898.

Pratsinis, S. E. Flame Aerosol Synthesis of Ceramic Powders. *Prog. Energy Combust. Sci.* **1998**, *24* (3), 197-219.

Randolph, A. D.; Larson, M. A. *Theory of Particulate Processes;* Academic: New York, 1988; pp 36-37.

Rao, N. P.; McMurry, P. H. Nucleation and Growth of Aerosol in Chemically Reacting Systems: A Theoretical Study of the Near-Collision-Controlled Regime. *Aerosol Sci. Technol.* **1989**, *11* (2), 120-132.

Ryu, T.; Sohn, H. Y.; Han, G.; Kim, Y.-U.; Hwang, K. S.; Mena, M.; Fang, Z. Z. Nanograined WC-Co Composite Powder by Chemical Vapor Synthesis. *Metall. Mater. Trans. B* **2007**, *39* (1), 1-6.

Schefflan, R.; Kovenklioglu, S.; Kalyon, D.; Mezger, M.; Leng, M. Formation of Aluminum Nanoparticles upon Condensation from Vapor Phase for Energetic Applications. *J. Energ. Mater.* **2006**, *24* (2), 141-156.

Schild, A.; Gutsch, A.; Mühlenweg, H.; Pratsinis, S. E. Simulation of Nanoparticle Production in Premixed Aerosol Flow Reactors by interfacing Fluid Mechanics and Particle Dynamics. *J. Nanopart. Res.* **1999**, *1* (2), 305-315.

Schwade, B.; Roth, P. Simulation of Nano-particle Formation in a Wall-Heated Aerosol Reactor including Coalescence. *J. Aerosol Sci.* **2003**, *34* (3), 339-357.

Seinfeld, J. H.; Pandis, S. N. *Atmospheric Chemistry and Physics. From Air Pollution to Climate Change*, 2nd ed.; Wiley: Hoboken, NJ, 2006; p 1225.

Setyawan, H; Yuwana, M. Modeling and Simulation of Aluminum Nanoparticle Synthesis by the Evaporation-Condensation Process Using the Nodal Method. *Chem. Prod. Process Model.* **2008**, *3* (1), Article 32.

Shi, X. L.; Shao, G. Q.; Duan, X. L.; Xiong, Z.; Yang, H. Characterizations of WC-Co Nanocomposite Powders and Subsequently Sinterhip Sintered Cemented Carbide. *Mater. Charact.* **2006**, *57* (4-5), 358-370.

Siegel, R.; Howell, J. R. *Thermal Radiation Heat Transfer*, 3rd ed.; Taylor & Francis: Washington, DC, 1992; pp 263-266.

Sohn, H. Y.; PalDey, S. Synthesis of Ultrafine Nickel Aluminide Particles by the Hydrogen Reduction of Vapor-Phase Mixtures of $NiCl_2$ and $AlCl_3$. *J. Mater. Res.* **1998a**, *13* (11), 3060-3069.

Sohn, H. Y.; PalDey, S. Synthesis of Ultrafine Particles of Intermetallic Compounds by the Vapor-Phase Magnesium Reduction of Chloride Mixtures: Parts I and II. *Metall. Mater. Trans. B* **1998b**, *29* (2), 457-469.

Sohn, H. Y.; PalDey, S. Synthesis of Ultrafine Particles and Thin Films of Ni_4Mo by the Vapor-Phase Hydrogen Coreduction of the Constituent Metal Chlorides. *Mater. Sci. Eng. A* **1998c**, *247* (1-2), 165-172.

Sohn, H. Y.; Ryu, T.; Choi, J. W.; Hwang, K. S.; Han, G.; Choi, Y. J; Fang, Z. Z. The Chemical Vapor Synthesis of Inorganic Nanopowders. *JOM* **2007**, *59* (12), 44-49.

Szekely, J.; Evans, J. W.; Sohn, H. Y. *Gas-Solid Reactions;* Academic: New York, 1976; pp 47.

Thölén, A. R. Gas Evaporation and Electron Microscopical Observation of Small Particles. *Nanophase Materials* **1994**, *260*, 57-72.

Turns, S. R. *An Introduction to Combustion: Concepts and Applications*, 3rd ed.; McGraw-Hill: New York, 2012; p 21.

Ulrich, G. D.; Milnes, B. A.; Subramanian, N. S. Particle Growth in Flames. II: Experimental Results for Silica Particles. *Combust. Sci. Technol.* **1976**, *14* (4-6), 243-249.

Upadhyaya, G. S. *Cemented Tungsten Carbide: Production, Properties and Testing*; Noyes Publications: New York, 1998.

Wahlberg, S.; Grenthe, I.; Muhammed, M. Nanostructured Hard Material Composites by Molecular Engineering 1. Synthesis from Soluble Tungstate Salts. *Nanostruct. Mater.* **1997**, *9* (1-8), 105-108.

Won, C.-W.; Chun, B.-S.; Sohn, H. Y. Preparation of Ultrafine Tungsten Carbide Powder by CVD Method from WCl_6-C_2H_2-H_2 Mixtures. *J. Mater. Res.* **1993**, *8* (10), 2702-2708.

Wu, X. Y.; Zhang, W.; Wang, W.; Yang, F.; Min, J. Y.; Wang, B. Q.; and Guo, J. D. Ultrafine WC-10Co Cemented Carbides Fabricated by Electric-Discharge Compaction. *J. Mater. Res.* **2004**, *19* (8), 2240-2244.

Zawrah, M. F. Synthesis and Characterization of WC-Co Nanocomposites by Novel Chemical Method. *Ceram. Int.* 2007, *33* (2), 155-161.

Zhu, Y. T.; Manthiram, A. Influence of Processing Parameters on the Formation of WC-Co Nanocomposite Powder Using a Polymer as Carbon Source. *Composites, Part B* **1996**, *27* (5), 407-413.